IMT School for Advanced Studies, Lucca
Lucca, Italy

In joint supervision with

Universidad de Sevilla
Seville, Spain

A variational approach to brittle fracture and cohesive delamination: modelling and technological applications

PhD in Institutions, Markets and Technologies
Curriculum in
Computational Mechanics
XXX Cycle

Valerio Carollo

2018

The dissertation of Valerio Carollo is approved.

Program Coordinator of Computational Mechanics Curriculum Cycle XXX: Prof. Marco Paggi, IMT School for Advanced Studies, Lucca

Supervisor: Prof. Marco Paggi, IMT School for Advanced Studies, Lucca

Supervisor: Dr. José Reinoso, University of Seville

Tutor: Prof. Marco Paggi, IMT School for Advanced Studies, Lucca

The dissertation of Valerio Carollo has been reviewed by:

Prof. Pedro Camanho, University of Porto

Prof. Davide Bigoni, University of Trento

Prof. Luis Tavara, University of Sevilla

IMT School for Advanced Studies, Lucca

2018

To my family

Contents

List of Figures

List of Tables

Acknowledgements

First and foremost, I would like to express my deep gratitude to Prof. Marco Paggi and Dr. José Reinoso for their fruitful supervision and support during my doctoral period. Their ideas and research directions are the key that has led to the contents of this thesis.

The majority of the thesis is based on articles published, or currently under publication, co-authored by Prof. Paggi and Dr. Reinoso. These articles are listed in the Publications Section of this thesis. In particular, from article 1 are based the Sections 3.1.3, 3.2.2 and 5.2. From article 2 are based the Sections 3.1.1, 3.1.2, 3.2.1 and all Section 5.1 except Section 5.1.3. From article 3 are based the Sections 3.1.1, 3.1.2, 3.2.1 and the introduction of Chapter 5. From article 4 is based Section 2.1. On these article are also based parts of Chapters 1 and 6.

I would like to thank Dr. Claudia Borri for her great availability and support for the experimental part of my doctoral research. The collaboration with Dr. Borri has led to the research described in Section 2.1.

I would also like to thank Dr. Dario Piga from the Dalle Molle Institute for Artificial Intelligence Research (Switzerland). His expertise in the field of identification and optimization algorithm has led to the research described in Section 4.1.

I would like to acknowledge the members of the Micro and Nano Mechanics group at IMDEA Materials institute (Spain) for the collaboration during my visiting period in 2016. That collaboration has led to the research described in Sections 2.2 and 5.1.3.

I would like to acknowledge the European Research Council for the support to the ERC Starting Grant Multifield and multi-scale Computational Approach to Design and Durability of PhotoVoltaic Modules - CA2PVM, under the European Unions Seventh Framework Programme (FP/2007-2013)/ERC Grant Agreement n. 306622, which has partially supported the present research.

I would like thank my friend and colleagues from IMT Lucca for the pleasant environment create and enjoyable moments spent during my Ph.D. years.

I am particularly grateful to my family to the support and care provided me during my studies.

Publications

1. V. Carollo, J. Reinoso and M. Paggi. "A 3D finite strain model for intralayer and interlayer crack simulation coupling the phase field approach and cohesive zone model". *Composite structures* 182 (2017): 636-651.
2. V. Carollo, J. Reinoso and M. Paggi. "Modeling complex crack paths in ceramic laminates: a novel variational framework combining the phase field method of fracture and the cohesive zone model approach". *Journal of the European Ceramic Society*. Under review.
3. V. Carollo, J. Reinoso and M. Paggi. "Recent advancements on the phase field approach to brittle fracture for heterogeneous materials and structures". *Advanced Modeling and Simulation in Engineering Sciences*. Under review.
4. V. Carollo, M. Paggi and C. Borri. "A two-scale constitutive parameters identification procedure for elastoplastic fracture". *COMPLAS XIII: proceedings of the XIII International Conference on Computational Plasticity: fundamentals and applications*. CIMNE, 2015.
5. V. Carollo, M. Paggi and A. Rossani. "A two parameter elasto-plastic formulation for hardening pressure-dependent materials". *Mechanics Research Communications* 77 (2016): 1-4.

Abstract

A new computational model is used for the study of fracture phenomena in homogeneous and composite materials. The computational model is based on the coupling between the phase field model and the cohesive zone model within the framework of the finite element method. This model is adopted from literature and consistently extended. The enhancements enclose the combination of the model with plasticity and its extension to the 3D finite elasticity framework. This extension is formulated in a consistent way by means of the variational approach. The model is validated through numerical examples mostly based on experimental results. The experiments are designed and performed by means of experimental facilities suitable for micro testing. The numerical simulations comprehend problems at different scales of homogeneous and composite materials in the bi-dimensional and three-dimensional space. The model results particularly appropriate for many technological applications. Among the different applications, the following cases are analysed: the competition between crack propagation and plasticity; the adhesive wear phenomenon considering the fracture of the micro asperities of two surfaces in contact; the mechanical behaviour of a nanolaminate and a microlaminate; the interaction between crack propagation and delamination. In the latter application is where the model shows its strength. The competition between crack propagation and delamination in composite materials is simulated without the necessity of remeshing or crack tracking algorithms. The model is particularly suitable for the exploitation in many engineering industrial fields.

Chapter 1

Introduction

The onset and development of fracture events in solids has attracted an increasing interest in many engineer fields. The prediction of the environmental conditions which lead to the damage or failure of an engineer system play a key role in the design of durable and safe structures. The discipline which deals with this problem is Fracture Mechanics. Fracture mechanics provides the rules to design a mechanical structure that can operate in safety. The loading conditions are identified and defined in order to avoid strong fracture phenomena like macroscopic cracks or failure of the structure.

In order to study the problem, we should take under consideration that in every engineer structure imperfections like micro cracks or flaws are always present. The evolution of such imperfections promote the appearance of microscopic failure events, whose coalescence cause macroscopic fracture phenomena. In order to investigate these phenomena, fracture mechanics deals with different length scales [1]. At the atomic scale fracture is considered as the separation between atoms and atomic slip systems. At the micro scale fracture phenomena interest the grains of polycrystalline materials. Herewith, it is defined the competition between interlayer and intralayer fracture. At bigger scales, fracture phenomena can interest the micro structure of a composite materials. At the macro scale the materials take into accounts the lower scale considering

the stress and strains of the continuum material.

1.1 Review on fracture mechanics

The first pioneering investigation on Fracture Mechanics was conducted by Inglis [2]. He studied the case of an infinite plane with an elliptic hole under constant external stress (Fig. 1). After this seminal contribution, in 1921, Griffith [3] built the foundation of the so called Linear Elastic Fracture Mechanics (LEFM) theory stating the energy balance criterion. According to this criterion the crack propagation can be predicted through a relation among 5 energies contributions:

$$U_t = U_i - U_a - U_w + U_\gamma \tag{1.1}$$

where U_t is the total elastic energy of the cracked body, U_i is the initial strain energy of the uncracked body, U_a is the elastic energy release for the introduction of the crack, U_w is the work made by external loadings and U_γ is the increase in surface energy due to the creation of the crack. From this energy balance criterion is possible to compute the critical stress at fracture σ_F imposing that the variation of total energy U_t with respect to the crack length a has to be minimum. This condition can be expressed mathematically as:

$$\frac{dU_t}{da} = 0 \quad \rightarrow \quad \sigma_F = \sqrt{\frac{2E\gamma_s}{\pi a}} \tag{1.2}$$

where E is the Young modulus and γ_s is the surface energy per unit length. Many authors used LEFM to solve the problem with crack of different shapes [4]. The stress distribution near the crack tip can be estimated through the fundamental developments by William [5], which state that for all the crack tips the stress field is governed by the same qualitative distribution. According with such assumptions, the so-called stress intensity factor K [6] was introduced, which correspond to a central magnitude to evaluate a particular fracture criterion.

The LEFM theory allows to describe many cracking phenomena, nevertheless some limitations has to be considered. First of all, a crack can

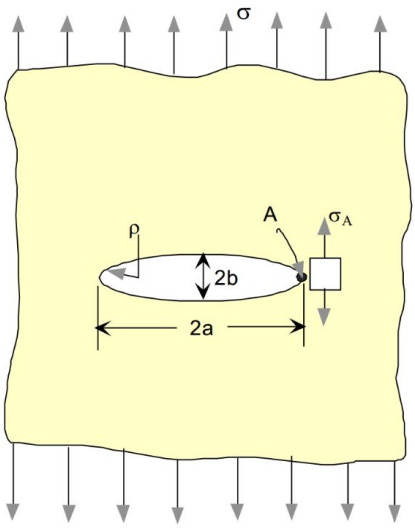

Figure 1: Infinite plane with a central elliptic hole under tension.

only propagates starting from a pre-existing defect rather than nucleates and propagates. Secondly, the theory can be applied only to brittle materials. In fact, due to the stress concentration at the crack tip the yield limit would be violated even at low external load. In order to overcome the latter limitation, the theory was extended to the so called Elasto-Plastic Fracture Mechanics (EPFM), where the elasto-plastic formulation is considered to predict the redistribution of the stress and the blunting of the crack tip due to the yielding of the material. The material develop plasticity near the crack tip creating the so called plastic zone. The dimension and shape of the plastic zone depend on the material properties and loading conditions. In particular, the higher is the stress intensity factor or the lower is the value of the yield stress, the larger is the dimension of the plastic zone. In the case of small plastic zone compared with the crack length and the dimension of the structure, the plastic zone length (d_p) was computed in [7] assuming: von Mises plasticity; perfect plastic behaviour; dependence of the plasticity on the stresses and strains within a circle centred at the crack tip. Later, Irwin [8] correct that value of d_p

assuming also at the crack ligament a force balance criterion between the elastic and the elasto-plastic stress curve, obtaining:

$$d_p = \frac{1}{6\pi}\left(\frac{K_I}{\sigma_F}\right)^2 \tag{1.3}$$

where K_I take the name of stress intensity factor. Irwin also computed the values of the effective crack length and the stress intensity factor. Dugdale [9] set up another model which provide a similar result. He started from three main assumptions: the entire plastic deformation is concentrated in a strip of length d_p; the strip has perfect plastic behaviour; the effects of an external constant tension are superimposed with the effects of a constant tension acting on the strip. This formulation leads to:

$$d_p = \frac{\pi}{8}\left(\frac{K_I}{\sigma_F}\right)^2 \tag{1.4}$$

The solution of this problem provides a relation that differs from the Irwin model only for a multiplicative constant.

Nowadays, these models are well-establish theory for the description of fracture phenomena. In order to extend their applicability to complex structural structure many computational models have been developed. In the following section a review of the most used computational models in the field of fracture mechanics are provided.

1.2 Fracture mechanics computational models

The development of new materials make fracture events a matter of the interaction of many different phenomena. For instance, the advent of new composite materials raised new investigation lines. Complex crack patterns such as branching, multiple coalescence and crack merging are developed in many engineering structures. These phenomena are caused for the presence of anisotropy and/or heterogeneities, interfaces as well as multi-axial external loadings, among others factors.

As a consequence of its practical importance, in the last decades, many computational models have been developed to predict the strength

and the crack path in brittle materials. Most of the computational models for the description of fracture phenomena are developed within the finite element method (FEM) [10] or boundary element method (BEM) [11; 12]. Techniques like the extended finite element method (XFEM) [13; 14], finite fracture mechanics (FFM) [15] and the embedded finite element method (EFEM) [16; 17; 18] belong to this class of approaches. In parallel, methods to simulate quasi-brittle and interface fracture adopting the cohesive zone model (CZM) [19; 20] have been proposed to simulate cohesive fracture typical of elasto-plastic materials or interfaces. These computational models generally suffer from some drawbacks due to the complexity in tracing the evolution of the crack path. On the one side in XFEM and EFEM, a splitting algorithm has to be defined for the element crossed by the crack or containing the crack tip. This leads to crack topology problems when the quadratic or higher order displacement interpolation schemes are employed. This is not the case of FFM which is a powerful and well-founded predictive tool, but can only by applied to relatively simple structures for feasibility reasons. On the other side, CZM-based methods, implemented using interface finite elements, are viable strategies for pre-existing interfaces [21], while several algorithmic complexities arise for modelling evolving cracks in the continuum [22].

Alternatively, continuum damage models (CDM) use a smeared crack representation over a material band and constitute an easy-solution to be implemented into standard finite element codes [23]. Pathological mesh-dependency of CDMs can be alleviated by means of non-local damage methods such as integral-based formulations [24], gradient enhanced models [25; 26; 27; 28; 29], and thick level set methods [30; 31], to quote a few of the existing modeling options.

Rooted on the Griffith theory of fracture, recent phase field methods can be conceptually categorized as a gradient extended dissipative formulations. These methods are derived within the context of the so-called variational approach of fracture and are especially suitable for brittle materials [32]. In particular, phase field formulations endow a regularization of the Griffith theory using a characteristic length scale l in the spirit

of the Γ-convergence [33; 34; 35]. Due to their strong potential to model complex crack patterns, phase field methods have been intensively developed following the landmark thermodynamically consistent formulation proposed by Miehe et al. [36; 37]. Subsequent extensions to dynamic [38; 39] and ductile [40] fracture, higher order approximations [41], multi-field problems [42; 43; 44] and shell structures [45; 46; 47; 48; 49] have been successfully put forward in the last few years.

Recently, further developments of the phase field approach of fracture for heterogeneous media have followed two basic methodologies: (i) the use of a new energy model which combines the brittle energy dissipation due to fracture in the bulk and the interfacial damage, based on the level set method [50; 51], and (ii) the pioneering modelling framework developed in [52], which accounts for the interaction between the phase field model in the bulk and the interface cohesive model. This latter variational concept has shown a great level of accuracy to retrieve linear elastic fracture mechanics (LEFM) results for heterogeneous media, and seminally provided a comprehensive discussion regarding the interaction between both fracture approaches based on the ratio between their characteristic length scales, i.e. l/l_{CZM} where l_{CZM} is the characteristic length scale of the cohesive model.

1.3 Objectives and organization of the thesis

In this thesis, a variational approach based on the phase field model for brittle fracture and the cohesive zone model is proposed. The model consider the combination of these two computational methods together with other constitutive models such as plasticity. Phase field and cohesive zone model are also coupled at the constitutive level making use of the approach developed in [52]. This approach is adopted and enhanced considering its three-dimensional formulation in the finite elasticity framework. Without loss of generality, the variational formulation for the bulk is particularized to solid shells based on the novel enhanced assumed strain formulation presented in [49] to prevent locking pathologies. Therefore, the proposed formulation enables the interaction

of phase field and cohesive zone models for fracture with locking free solid shell elements.

The dissertation is organized as follows. In Chapter 2 an experimental investigation on fracture phenomena is presented. In Section 2.1 the interaction between crack propagation and plasticity is studied by means on tensile tests on metallic strips. In Section 2.2 the fracture properties at the micro scale are studied by means of experiments on a nanolaminate materials. In this case the experiments are performed with facilities suitable for micro testing.

In Chapter 3 the variational formulation and the finite element implementation of the computational model is outlined. The phase field model is presented in Section 3.1 and the cohesive zone model is presented in Sections 3.2. In the latter section the coupled formulation of the two model is presented.

In Chapter 4 the computational model herein proposed is applied to two technological applications. In Section 4.1.1 the experimental results described in Section 2.1 are reproduced in order to identify the material and fracture parameters of the material. In Section 4.2 the adhesive wear phenomenon is investigated by means of simulations based on the phase field model.

In Chapter 5 the coupled phase field and cohesive zone model framework is used to study the interaction between crack propagation and delamination in laminates. This interaction is responsible for the generation of the typical complex crack paths developed in laminates. The problem is approached in Section 5.1 by means of parametric analysis and technology applications. In particular the experiments described in Section 2.2 are reproduced in order to characterize the nanolaminate. In Section 5.2 we show the potentialities of the 3D finite elasticity formulation of the coupled phase field and cohesive zone model framework. Then, numerical simulations on flat and curved 3D geometries are presented.

Finally, Section 6 addresses the main conclusions of the current research. Moreover, it is outlined the perspective future developments and applicability of the research developed.

Chapter 2

Experimental investigation of the interaction between crack propagation, plasticity and delamination

In this chapter is presented the behaviour of the crack propagation in different materials and structures with high relevance in high technological engineering applications. In particular, several experimental tests that aim to shade light on the phenomena involving crack propagation together with plasticity or delamination are henceforth analysed in detail. In Section 2.1 the interaction between the crack propagation and the plasticity is investigated with a metallic strip tested under uniform tensile loading. In Section 2.2 the interaction between the crack propagation and the delamination of the interfaces of a nanolaminate is investigated. The experimental facilities as well as the experimental procedure are thoroughly described together with the corresponding results. Then, the fracture performance of each of the engineering components under consideration are characterized.

2.1 Crack propagation and plasticity

In this section the interaction between crack propagation and plasticity is investigated by means of an application from the field of photovoltaic (PV) technologies. The PV power generation via Silicon-based wafers is one of the most growing technology in the framework of renewable energies. Among all the factors which influence the efficiency of PV panels the mechanical integrity plays a key roll. In fact, a statistic comprise in the period 2008-2011 from the Institute for Solar Energy Research Hamelin and TÜV Rheinland reveals that the 6% of the of the PV modules present cracking phenomena already before the installation [53]. These cracks are likely to evolve in more severe damage phenomena due to ageing environmental effects like snow, wind gusts, hail or rapid temperature variations.

In order to study the consequences of these environmental effects on PV modules, various authors reproduce the environmental conditions via mechanical testing. In [54] the fatigue behaviour of PV modules affected by a preexisting crack have been studied. The preexisting cracks have been generated by the impact of a PMMA balls of 4 cm of diameter at a velocity of 6 m/s. After this, the crack propagation has been monitored during a 650 cycle of a fatigue 3-point bending test. The crack propagation together with the power loss during the fatigue test were monitored via an electroluminescence camera (Fig. 2). In [55], indeed, it has been studied the power loss and the crack propagation in a flexible PV module. The PV module has been tested under 4-point bending. The same electroluminescence technique was used to capture the results of the test.

These investigations provide a thorough understanding with regard to the durability of the silicon wafer of the PV cells. In this section we focus our attention on the durability of the electrical connections employed between the PV cells. This electrical connections are metallic strips called busbars (Fig. 3 (a)). The main problem of the busbars is that the gap which separate two PV cells can suffer strong deformations. In [56] the effect of the temperature variation on the gap deformation is studied.

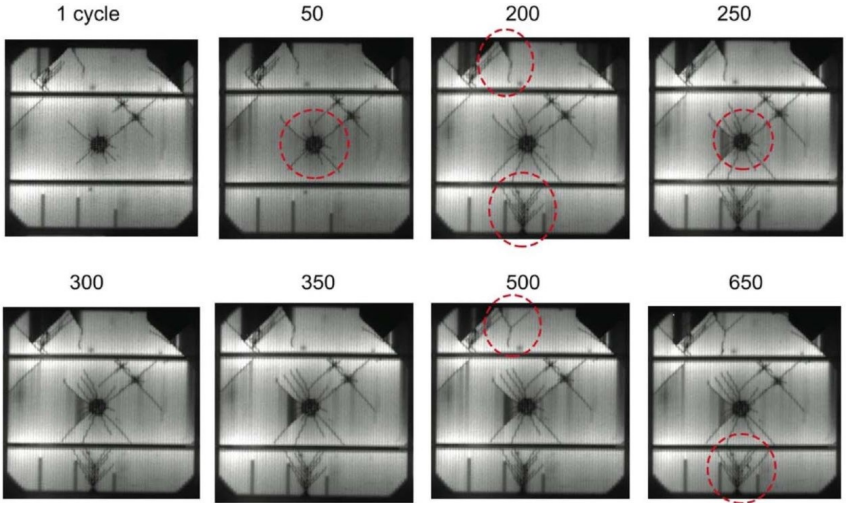

Figure 2: Electroluminescence images showing the crack propagation during the 3-point bending fatigue tests. With permission from [54]

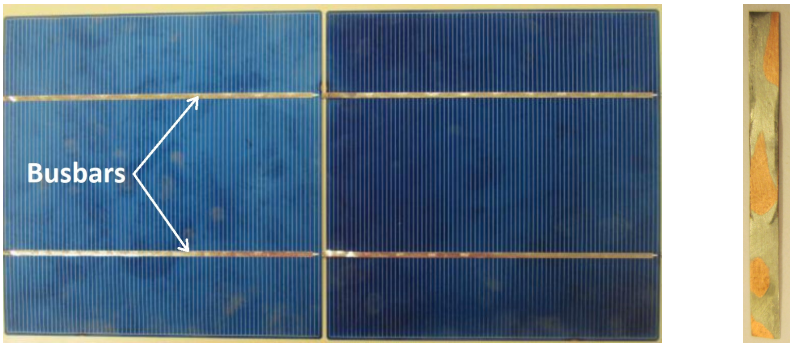

(a) (b)

Figure 3: (a) busbars which connect two photovoltaic cells; (b) partially etched specimen of a busbar. It can be recognize the silver coating and the inner copper part (red).

They found that between the temperature range of $-40°$ and $-80°$ the gap suffer a strain from -1.25% to $+2\%$. Considering that metals un-

dergo plastic deformations from around a strain of 0.2%, we expect that plasticity can be developed in busbars.

In the following section we investigate the interaction between crack propagation and plasticity by means of experimental tests on busbars. The tested busbars are composed of copper coated by a thin layer of silver (Fig. 3 (b)). The experimental campaign is then conducted to characterize the mechanical and fracture properties of the busbars. Moreover, in Section 4.1 the characterization is supported by a computational model and an optimization algorithm.

2.1.1 Experimental tests on busbars' specimens

The experimental campaign described in this section is conducted in the MUSAM-Lab of the IMT School for Advanced Studied Lucca in collaboration with Dr. Claudia Borri. The experiments are performed using a Deben Gatan MTEST5000S tensile stage (Fig. 4) equipped with a 5 kN loading cell. The tensile stage is placed inside a scanning electron microscope (SEM) Zeiss EVO MA15, capable of working with variable pressure to avoid metallization or graphitization of the samples surface. This experimental setup allows performing monotonic and cyclic tensile tests and record images of the surface during the test at different magnifications, observing the evolution of crack propagation at the micro scale.

The experiments are performed on notched and unnotched specimens of busbar. The geometry of the specimens is characterized by a free span of 17 mm, a width of 2.6 mm, a thickness of 0.2 mm and a notch with length a_0 which vary among the values: 0 mm (unnotched), 0.45 mm and 0.8 mm (Fig. 5). The total specimen length is longer than the free span length. This external part is roll with a Teflon stripe and clamped in the tensile stage. The Teflon stripe layer distribute the pressure of the clamp avoiding stress localizations and preventing boundary failure. The tests have been performed under quasi-static load applying a monotonically increasing tensile displacement Δ upon failure with a constant velocity of 0.033 mm/min.

Fig. 6 shows the results of the experiments in terms of force-displacement

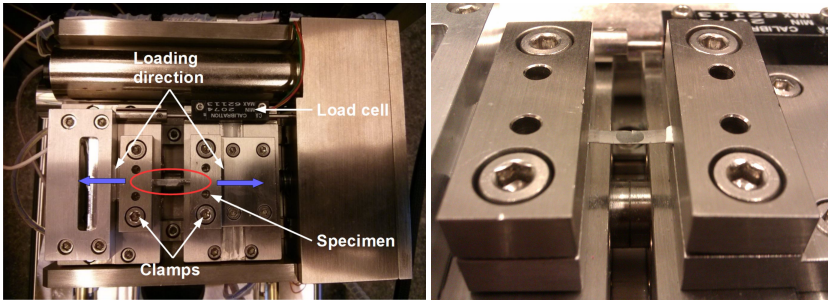

(a) (b)

Figure 4: Tensile stage: (a) description of the experimental set up; (b) detail of the specimen and the clamps.

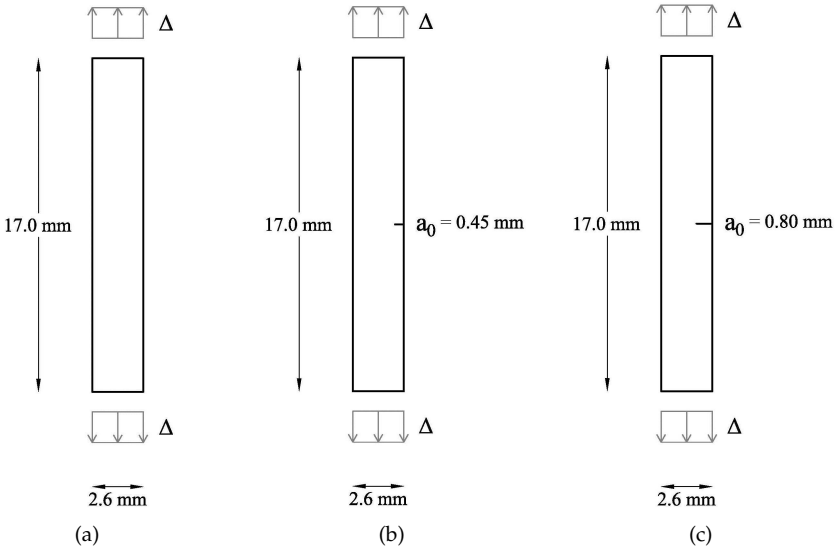

Figure 5: Specimen geometry and loading condition.

curves. In this curves the regular drops in the force evolution are caused by the temporary stops of the tensile stage for the recording of high resolution images of the specimen. The curve corresponding to the un-

notched specimen shows the typical behaviour of an elasto-plastic material. It is characterized by a first linear behaviour followed by a linear hardening until the failure of the specimen. The curves corresponding to the notched specimens show a coupled effect of plasticity and fracture. The first part of the curve is characterized by a linear elastic behaviour. After that a plastic behaviour is shown. At this stage the material around the notch tip experienced the development of strong plastic deformation while maintaining the notch length equal to the initial one. This behaviour can be observed comparing the SEM images Fig. 7(a) and 7(b). After a further increasing of the tensile displacement the curves show a softening behaviour which is maintained until the failure of the specimen. The softening branch of the curve can be addressed to the fracture onset and the consequent crack propagation from the notch tip (Fig. 7(c,d,e,f)).

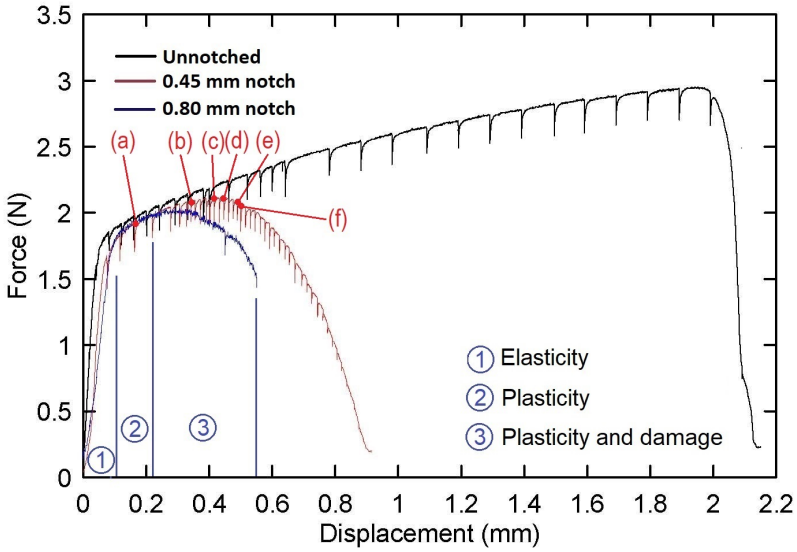

Figure 6: Force-displacement curves for three different notch lengths: unnotched specimen, 0.45 mm notch, 0.80 mm notch. The red letters refers to the sequence of images in Fig. 7.

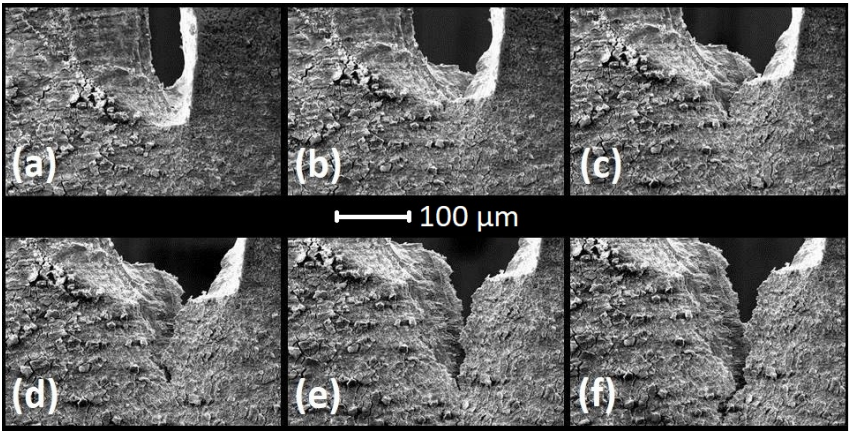

Figure 7: Evolution of the notch tip during the tensile test of the 0.45 mm notched specimen.For each image the imposed displacement is: (a) 0.163 mm; (b) 0.340 mm; (c) 0.415 mm; (d) 0.445 mm; (e) 0.490 mm; (f) 0.500 mm.

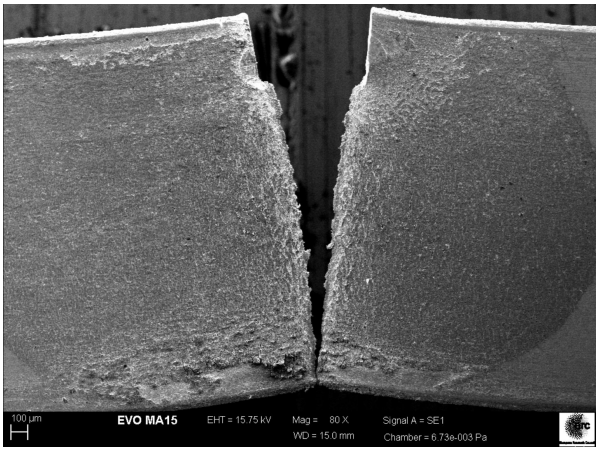

Figure 8: Crack path of the failed specimen with 0.45 mm notch.

The final crack direction follow a straight line (Fig. 8) as was expected from the symmetry of the specimen and of the imposed boundary conditions.

These experimental results are used in Section 4.1 for the mechanical and fracture characterization of the busbar. The characterization is supported by the numerical model described in Section 3.2, and by the optimization algorithms described in Section 4.1.

2.2 Fracture in Al/SiC nanolaminate

Nanolaminates composite have an increasing interest within the scientific community due to their outstanding material properties and the potential future applications in various engineering fields [57; 58; 59]. Nanolaminates are made of alternate layer of two different materials. Usually the two constituent materials have layer thickness which range from 10 nm to 100 nm. Various type of constituents combinations have been already studied: the metallic systems like Cu/Nb [60], Cu/W [61] or Al/Nb [62] among others; the metal ceramic systems like Al/SiC [63] or Al/TiN [64] among others. The former systems are characterized by ductile deformations. These systems show a strengthening due to the interaction between dislocations, interfaces, grain boundaries and due to the small layer thickness. In fact, the interfaces between the layers or the grain boundaries act as a barrier for the dislocation causing the so called dislocation pile-up. This phenomenon is the so called Hall-Petch behaviour, and it is responsible of the material strengthening at small scales. In metal ceramic nanolaminates deformations are limited due to the higher stiffness introduced by the ceramic materials. Moreover, plastic deformation are constraint within the metallic layer due to the brittle nature of ceramics.

In this section it is investigated the mechanical and fracture properties of the metal ceramic nanolaminate composed by aluminium and silicon-carbide (Al/SiC). The material structure of the Al/SiC nanolaminate can be seen in (Fig. 9). This nanolaminate is being studied as a suitable material for high wear resistant coatings applications. In fact, SiC layers gives to the nanolaminate good wear resistance properties, while the Al provides to the nanolaminate a ductile character to its mechanical performance. Al/SiC nanolaminates are commonly fabricated by magnetron

sputtering [65]. With this technology the material is slowly deposited on a substrate. In details, the material to be deposited (target material) is negatively charged and bombarded by energetic positive ions. The ions are generated from a glow discharged plasma. The impact of the ions on the target material provoke the ejection of atoms which will deposit on the substrate material. The Al/SiC surfaces used for the experiments herein described were fabricated with magnetron sputtering. A target of pure aluminium was used for the Al layers and a SiC target for the SiC layers. The sputtering gas used was Argon. The substrate where the sputtered material deposited was made of silicon (Si).

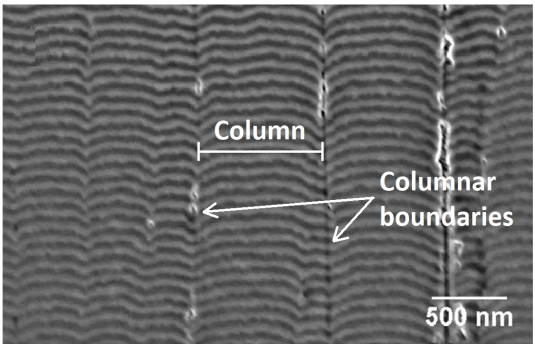

Figure 9: Al/SiC nanolaminate layer structure. The darker uniform layers correspond to the SiC layers. The clearer layers correspond to the Al layers. With permission from [66].

In order to investigate the small scale mechanical properties of such nano-structured materials, experimental facilities able to perform micro testing are required. The most used technology for micro testing is the nanoindentation [67]. Nanoindenters are instruments which apply a pressure on the material by means of a tip of the dimensions of few microns. The indenter is equipped in a load cell able to measure with high precision the force and the displacement imposed on the specimens. Indenter's tips are made of material with high stiffness like diamond. This materials avoid the development of not negligible deformations of the tip during the experimental tests. The tip of the indenter can assume vari-

ous geometries. The most commons are flat, cube corner and Berkovich geometry [67].

The most simple test that can be performed with a nanoindenter is the indentation test. In the indentation test the surface of a material is punched with the indenter until a prefixed pressure is detected by the load cell. The loading-unloading curve provided by the test allow to calculate the hardness and the Young modulus of the material [67].

More advanced techniques make use of indenters in order to impose a concentrate load to a specimen with a particular geometry. The geometry of the specimens are realized by means of Focus Ion Beam (FIB). This equipment realize 3D geometries eroding the material that surround the desire geometry. In particular, the FIB bombard the surface with gallium ions (ions with high mass). The material is then removed due to the impact between the ions and the material surface.

Making use of the FIB and the indenter, micropillars can be realized and tested under compression (Fig. 10). The aim of this test is to retrieve the fracture toughness of the material making it fail under compression. Flat punch or cube corner tip are used to impose a pressure to a micropillar [63; 68]. In particular the test that makes use of the cube corner tip has taken the name of pillar splitting test. This test provoke the failure of the micro pillar splitting it in three parts (Fig. 11). The way through which the existing fracture events propagate in the micropillar provides valuable informations regarding the material's fracture properties. In particular, the behaviour of the interfaces and the effect of the defect of the materials can be studied. For instance, Al/SiC nanolaminates are characterized by the so called columnar defect. This defect gives to the layers of the nanolaminate a wave shape (Fig. 9). The boundaries of this columnar defects are very brittle. A study currently under publication of researchers from IMDEA Materials institute shows that micropillars tends to fracture following the columnar boundaries.

The behaviour of the different fracture Modes of the Al/SiC nanolaminate has been also investigated. In [69] a shear test has been designed and performed (Figs. 12(a), 12(b)). This study provide informations regarding the fracture Mode II of the nanolaminate with layers parallel to

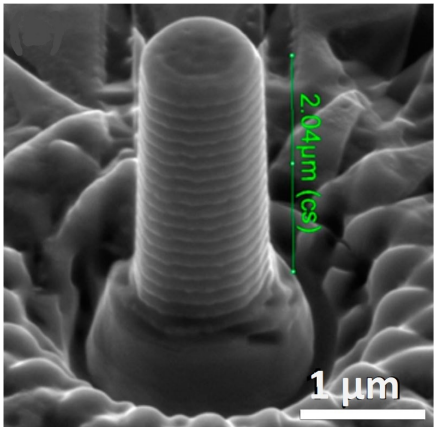

(a)

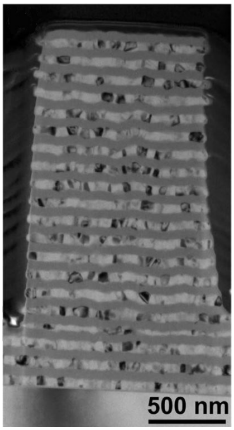

(b)

Figure 10: Micropillar geometry: (a) 3D geometry from SEM image; (b) internal structure of the layers from TEM image. With permission from [68]

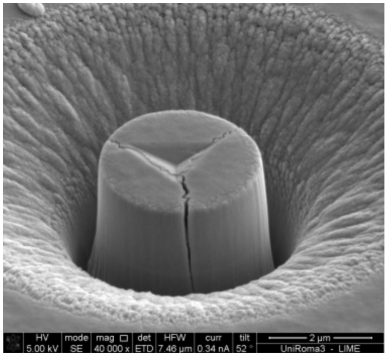

(a)

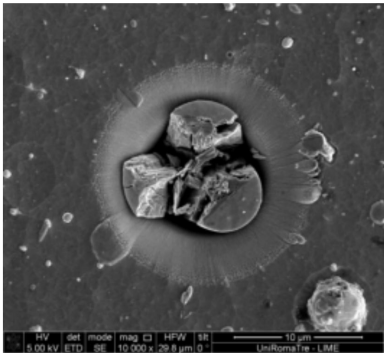

(b)

Figure 11: Pillar splitting test: (a) micropillar with the footprint of the cube corner tip indenter; (b) fractured micropillar due to the pillar splitting test. The non uniformity of the Al layers are given by the metallic grains. With permission from [63].

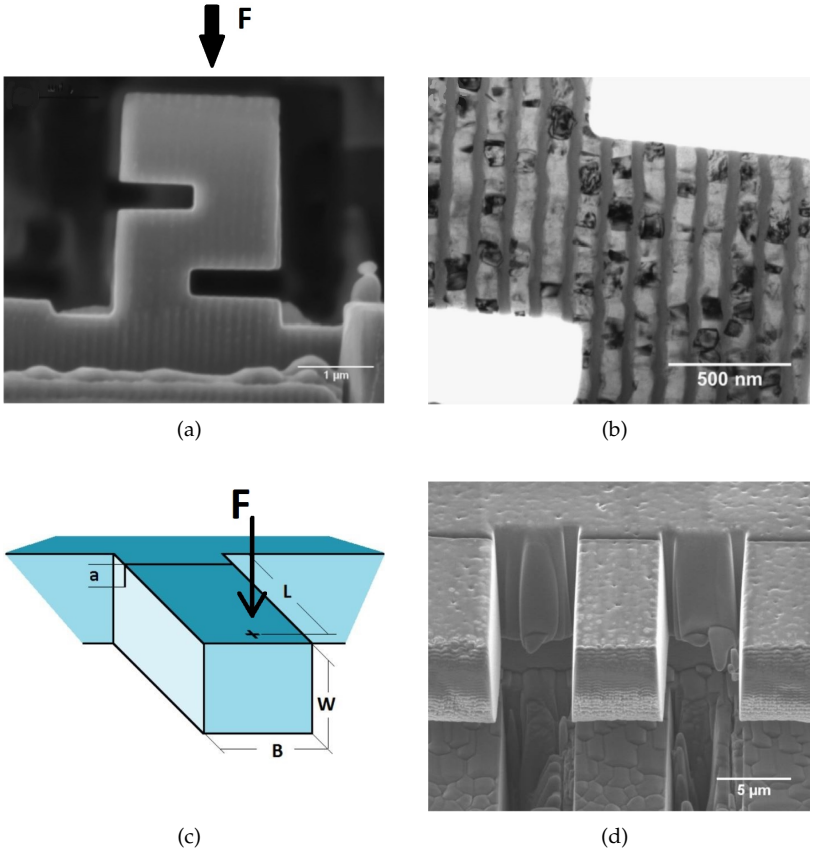

Figure 12: Micromechanical test: (a) SEM image of the shear test specimen; (b) TEM image of the layer structure of the shear test specimen; (c) micro cantilever beam test geometry; (d) SEM image of the cantilever specimens. With permission from [69] and [70]

the loading direction. Finally, in [70] cantilever beam tests has been designed and performed (Figs. 12(c), 12(d)). The cantilever beams have been notched near the constraint end of the beam. A pressure has been imposed from the top surface near the free end by means of an indenter. Cantilever beams with various layer thickness and layer orientations has

been tested.

In the following section the results of a tensile test technique are shown. The tensile test provides informations on the Mode I fracture properties of the weaker material. The difficulty of the micro tensile test is that is very laborious to be performed.

2.2.1 Micro tensile tests: design and results

The facilities used for the experimental campaign have been provided by the "Nanomechanics and Micromechanics of Advanced Materials" group of the IMDEA Materials institute. All the experimental results regarding the tensile tests of the Al/SiC nanolaminate have been retrieved in collaboration with Dr. Jon Molina-Aldareguia, Yang Lingwey and Alberto Palomares. They are all members of the research group above mentioned.

The experimental facilities used for the microstructural characterization of the Al/SiC nanolaminate are described in the sequel. First, a FIB-FEGSEM dual-beam microscope Helios NanoLab 600i, FEI (Fig. 13 (a)) is used. This facility is utilized for the micro machining and patterning of the specimens through ion-beam milling. Moreover, it is used for TEM sample preparation of lamellae. Additionally, a FEG S/TEM microscope Talos F200X, FEI (Fig. 13 (b)) is used to acquire high resolution images of the specimens. The TEM can reach good quality of images at lower scale with respect to the SEM. Then, it is used for the investigation of the fracture surface topography after the tensile test is performed. The tensile stage utilized for the tensile test inside the SEM is an in-situ nanoindenter Hysitron, PI87 (Fig. 13 (c)). This system can be assembled inside the SEM to carry out tests like nanoindentation, micro-compression, micro-bending, micro-tension. During the tests the load and the displacement are recorded and the deformation mechanisms of the materials can be investigated.

The procedure to perform a tensile test at the micro scale is not straightforward. First of all, a tensile grip of the dimension of few microns is needed. This grip has been previously machined from a diamond tip

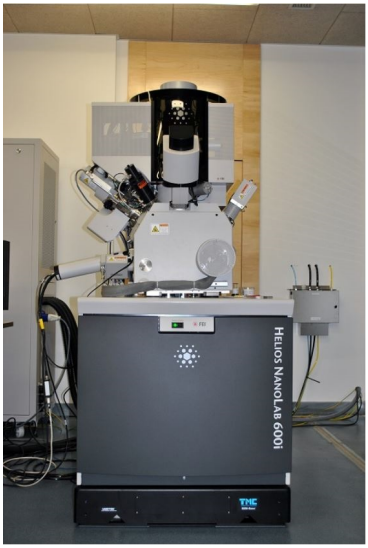

(a)

(b)

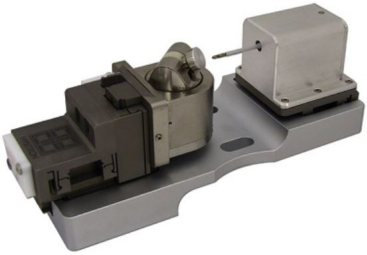

(c)

Figure 13: Experimental facilities used for the micro tensile test at IMDEA Materials institute: (a) FIB-FEGSEM dual-beam microscope; (b) FEG S/TEM microscope; (c) nanoindenter Hysitron, PI87.

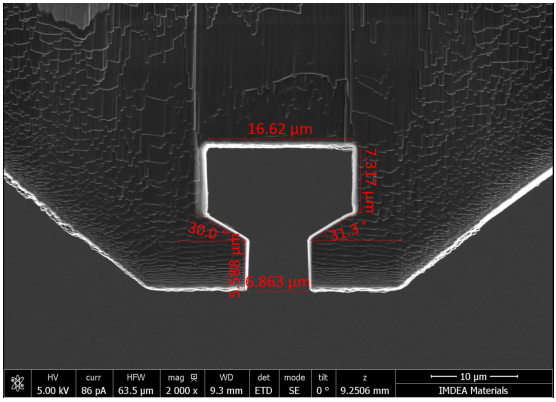

Figure 14: Micro tensile grip geometry.

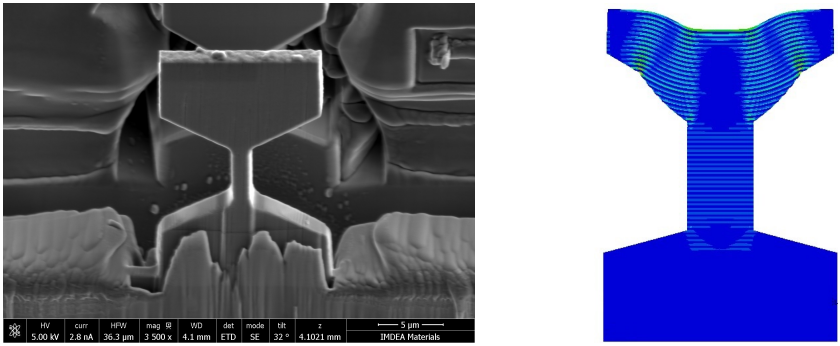

(a) (b)

Figure 15: (a) geometry of the micro dog bone specimen; (b) simulation of bending distortion of the specimen's head due to a small head height and a big specimen width.

through a FIB milling process (Fig. 14). After that, the nanolaminate specimen has to be machined through FIB to realize the required shape. In order to achieve a test with pure tensile load a micro dog bone specimen is produced (Fig. 15 (a)). The shape need to be precisely designed in order to make the head of the specimen fit within the tensile grip. The design of the specimens is also supported by preliminary numerical simulations. Hence, it is predicted the shapes which avoid problems such as stress concentrations at the specimen corners or undesired deformations of the specimen head.

The critical point of this design are basically three. Firstly, the specimen need a base large enough to ensure a low distributed tensile load at the interface between the laminate and the substrate. In fact, such interface is extremely weak. With an incorrect design the specimen could detach from the substrate during the tensile test. The second critical point is to avoid large stress intensifications in the transition between the specimens head/base and the specimen pillar. Finally, another critical point is to design the specimen head enough tall in order to avoid a bending deformation of the head (Fig. 15 (b)).

The nanolaminate available for the test is composed of Al/SiC sur-

faces with layer thickness dimensions of: 100 nm, 50 nm and 10 nm. The available nanolaminate has a total thickness which ranges between 10 μm and 17 μm. This is a limitation for the design of the specimen geometry. In fact, for the case of layers perpendicular to the tensile direction the total length of the specimen has to be contained in the total nanolaminate thickness.

After the achievement of a dog bone geometry which fulfil all the constraints, the tensile test is simulated in the finite element program Abaqus [71]. This simulations aim to verify: that the stress intensification in the specimen corners are not too big; that the stress at the interface between laminate and substrate are not too big; that the head of the specimen will not bend due to the displacement imposed by the tensile grip (Fig. 15 (b)). The variables which control that phenomena are the specimen head height and the specimen width in the middle part. The simulations are performed considering a linear elastic material for the SiC and an elasto - perfectly plastic material for the Al.

Once the specimen geometry design is completed the specimens are machined with the FIB system. Later, the tensile test of the specimens are performed in the SEM equipped with the tensile stage. The introduction of the specimen head inside the tensile grip is realized has follows: first the specimen head and the tensile grip are placed close but at different heights (Fig. 16 (a)); then, the specimen head and the tensile grip are aligned one on top of the other (Fig. 16 (b)); finally, the grip is moved vertically toward the specimen until the specimen's head is totally inside the grip. In order to verify that the specimen head is totally inside the tensile grip, a very small displacement which distance the grip from the specimen's head is imposed. When the load cell detect an increment in load then the specimen head is considered inside the grip

The experimental campaign is composed of 5 tests. For the case of layers perpendicular to the loading direction, specimens with layer thickness of 100 nm and 50 nm are tested. For the case of layers parallel to the loading direction specimens with layer thickness of 100 nm, 50 nm and 10 nm are tested. The tests are performed under displacement control. Regular stops are done to acquire high resolution images.

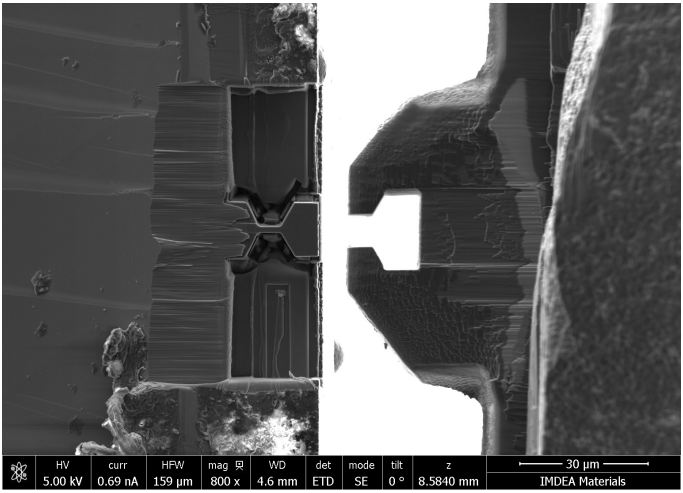

(a)

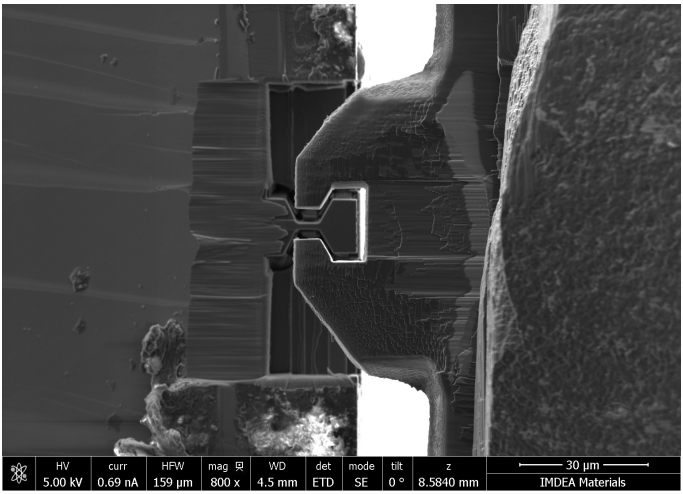

(b)

Figure 16: Procedure of alignment of the tensile grip and the specimen's head.

Fig. 17 (a) shows the force displacement curve of the tests with the layers perpendicular to the loading directions. The curve corresponding to the 100 nm thickness layers shows a quasi brittle behaviour. This is caused by the fact that the failure of the specimen can be addressed to the failure of an interface (Fig. 17 (b)). Indeed, the curve corresponding to the 50 nm thickness layer shows a small ductility but the overall behaviour can be also considered quasi brittle. This small ductility could be addressed to the fact that the failure of the specimen is an interaction between the delamination of an interface and the crack propagation in an Al layer. Moreover, the development of plasticity could have occurred and generate the nonlinearity in the force - displacement curve. In Fig. 17 (b) it can be seen the crack jump from an interface to another one crossing an Al layer.

The test on the specimens with layers parallel to the loading direction was not very successful. In fact, the specimens fail always following a columnar boundary defect of the material (Fig. 18 (b)). This made the specimen fail prematurely, as it can be see from stress value at failure in Fig. 18 (a). Consequently the data collected in these tests are not usable for the characterization of the material.

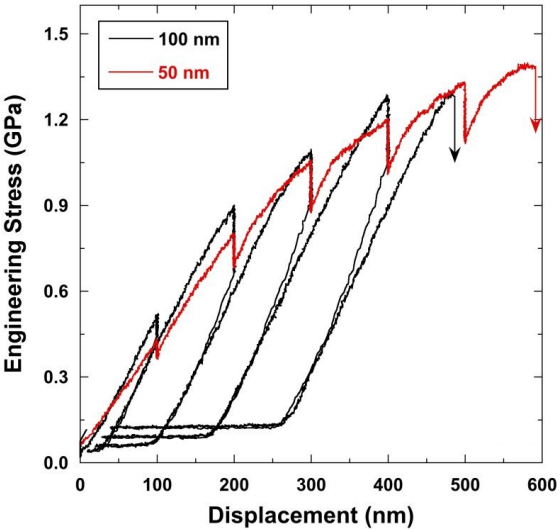

(a)

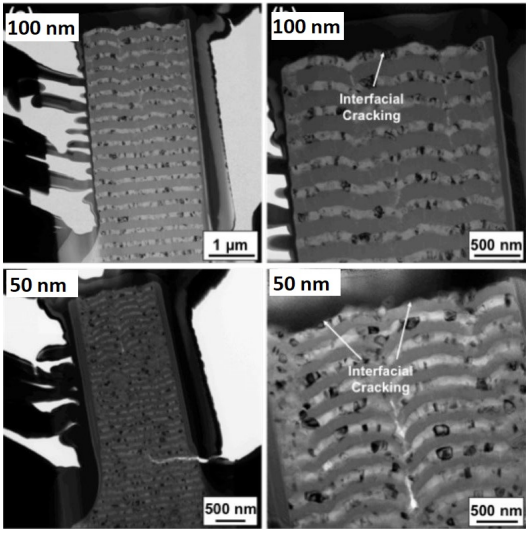

(b)

Figure 17: Tensile test with layers perpendicular to the loading direction: (a) stress-displacement curves; (b) TEM images of a lamella of the failed specimens.

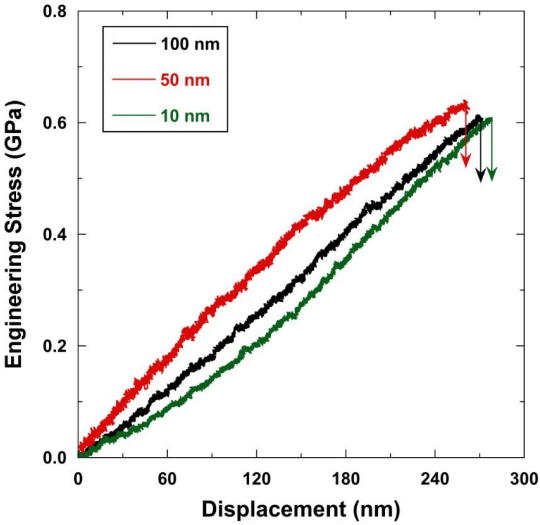

(a)

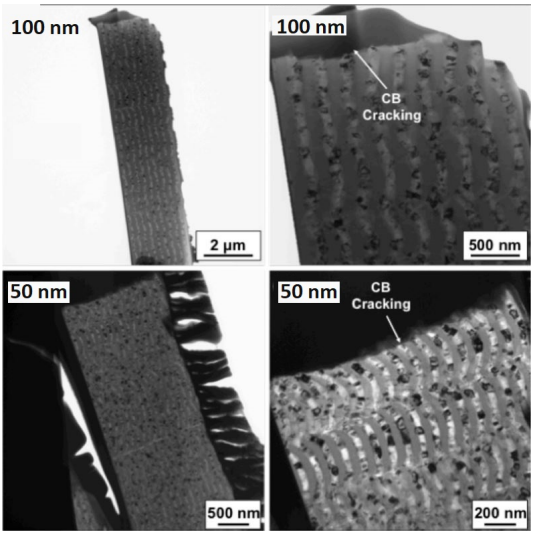

(b)

Figure 18: Tensile test with layers parallel to the loading direction: (a) stress-displacement curves; (b) TEM images of a lamella of the failed specimens.

Chapter 3

Computational approaches for fracture and delamination

3.1 Brittle fracture

In this section a smeared crack model for brittle fracture is used. Our approach is based on the recent phase field formulations. It allows the regularization of sharp crack representation using a pure continuous formulation. In particular, phase field models can be interpreted as a regularized version of the Griffith theory of brittle fracture in the spirit of the Γ-convergence [72]. One of the principal attributes of this approach concerns with the introduction of a characteristic length scale parameter into the particular form of the crack density functional.

3.1.1 Phase field (PF) model for brittle fracture

In this section we describe the thermodynamically consistent formulation of the Phase field (PF) method for brittle fracture. The formulation herein used is based on the approach proposed in [73; 74]. This formulation lays in the classical fracture theory of Griffith and Irwin, but it

considers the crack as a diffuse damage instead of a sharp discontinuity.

Our approach is developed in the general multi-dimensional framework (Fig. 19 (a)). We consider an arbitrary body $\Omega \in \mathbb{R}^n$ in the Euclidean space. An arbitrary point in the body Ω is denoted by the vector of its Cartesian coordinates $\mathbf{x}$, while the body forces are denoted by $f_{\mathrm{v}} : \Omega \longrightarrow \mathbb{R}^n$. The boundaries of Ω are denoted by $\partial\Omega \in \mathbb{R}^{n-1}$, which are split into the prescribed kinematic boundary $\partial\Omega_{\mathrm{u}}$ and the prescribed traction boundary $\partial\Omega_{\mathrm{t}}$. Where kinematic and traction boundaries fulfil the two conditions: $\partial\Omega_t \cup \partial\Omega_u = \partial\Omega$ and $\partial\Omega_t \cap \partial\Omega_u = \emptyset$. For a generic point of Ω, we denote the displacement vector by $\mathbf{u}$ and the Cauchy stress tensor by $\boldsymbol{\sigma}$. Then, the prescribed displacements, $\bar{\mathbf{u}}$, and tractions, $\bar{\mathbf{t}}$, at the respective boundaries are denoted by:

$$\mathbf{u} = \bar{\mathbf{u}} \quad \text{on } \partial\Omega_u \quad \text{and} \quad \bar{\mathbf{t}} = \boldsymbol{\sigma} \cdot \mathbf{n} \quad \text{on } \partial\Omega_t,$$

where $\mathbf{n}$ denotes the outward normal unit vector to the body.

In the PF model for brittle fracture the crack, which is usually represented by a discrete discontinuity, is regularized through a diffuse PF damage variable $\mathfrak{d}$, with $\mathfrak{d} : \Omega \,\mathrm{x}\, [0, t] \longrightarrow [0, 1]$ [75]. For $\mathfrak{d} = 0$ we have the undamaged state, while for $\mathfrak{d} = 1$ we identify a fully damage state. In the 1D case, between 0 and 1 the PF damage variable can vary following the law given in Fig. 19 (b). Here, the parameter l is the so called PF internal length, which control the amplitude of the diffusion area of the damage [73; 74].

Following this framework, the potential energy of the system takes the form:

$$\Pi(\mathbf{u}, \mathfrak{d}) = \int_\Omega \psi(\boldsymbol{\varepsilon}, \mathfrak{d}) \, \mathrm{d}\Omega + \int_\Omega \mathcal{G}_c \gamma(\mathfrak{d}, \nabla_{\mathbf{x}} \mathfrak{d}) \, \mathrm{d}\Omega, \tag{3.1}$$

where $\psi(\boldsymbol{\varepsilon}, \mathfrak{d})$ is the elastic energy density which depend on the damage $\mathfrak{d}$ and the strain $\boldsymbol{\varepsilon}$. $\mathcal{G}_c$ is the Griffith fracture energy and $\gamma(\mathfrak{d}, \nabla_{\mathbf{x}} \mathfrak{d})$ is the so-called crack density functional which depends on $\mathfrak{d}$ and its spacial gradient $\nabla_{\mathbf{x}} \mathfrak{d}$. The crack density functional is defined in [73] with the following equation:

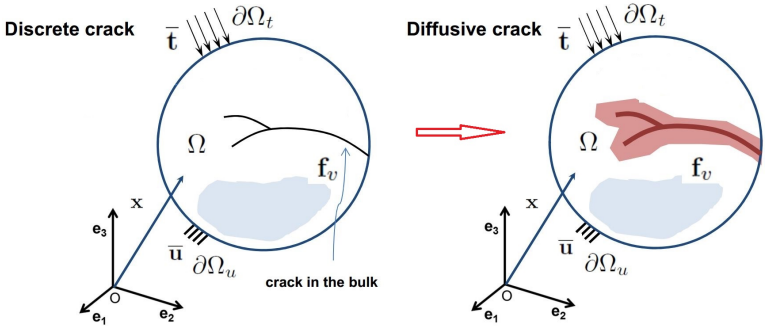

(a)

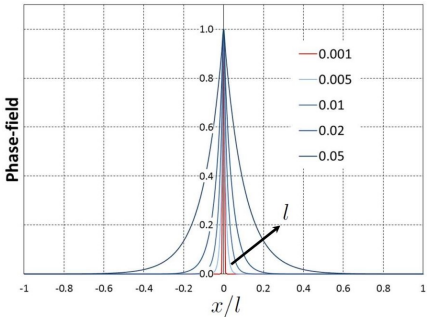

(b)

Figure 19: (a) comparison between the discrete discontinuity of the LEFM theory (left) with the smeared discontinuity of the PF model (right); (b) 1D approximation function which smear out the discontinuity, the damage $\mathfrak{d}$ follows the exponential based function $\mathfrak{d} = \mathrm{e}^{-|x|/l}$.

$$\gamma(\mathfrak{d}, \nabla_{\mathbf{x}}\mathfrak{d}) = \frac{1}{2l}\mathfrak{d}^2 + \frac{l}{2}|\nabla_{\mathbf{x}}\mathfrak{d}|^2. \tag{3.2}$$

Then, the Euler equations associated with the phase field formulation are:

$$\mathfrak{d} - l^2\nabla^2_{\mathbf{x}}\mathfrak{d} = 0 \quad \text{in } \Omega \quad \text{and} \quad \nabla_{\mathbf{x}}\mathfrak{d}\cdot\mathbf{n} = 0 \quad \text{in } \partial\Omega, \tag{3.3}$$

where $\nabla^2_{\mathbf{x}}\mathfrak{d}$ is the Laplacian of the PF variable.

Regarding the elastic energy stored in the body $\psi(\boldsymbol{\varepsilon}, \mathfrak{d})$, we consider the formulation based on the positive-negative split [76]. The positive counterpart of the elastic energy depends on the tensile stresses, while the negative counterpart depends on the compressive stresses. Following the approach in [36], the positive-negative split takes the form:

$$\psi(\boldsymbol{\varepsilon}, \mathfrak{d}) = \mathfrak{g}(\mathfrak{d})\psi_+^e(\boldsymbol{\varepsilon}) + \psi_-^e(\boldsymbol{\varepsilon}), \tag{3.4a}$$

$$\psi_+^e(\boldsymbol{\varepsilon}) = \frac{\lambda}{2}\left(\langle \mathrm{tr}[\boldsymbol{\varepsilon}]\rangle_+\right)^2 + \mu \mathrm{tr}[\boldsymbol{\varepsilon}_+^2], \tag{3.4b}$$

$$\psi_-^e(\boldsymbol{\varepsilon}) = \frac{\lambda}{2}\left(\langle \mathrm{tr}[\boldsymbol{\varepsilon}]\rangle_-\right)^2 + \mu \mathrm{tr}[\boldsymbol{\varepsilon}_-^2], \tag{3.4c}$$

where λ and μ are the Lamé constants, ε_+ and ε_- are, respectively, the positive and negative counterparts of the strain tensor. The symbol $\mathrm{tr}[\bullet]$ denotes the trace operator, the symbol $\langle \bullet \rangle_\pm$ denotes the so-called Macaulay brackets which describe the function $\langle \bullet \rangle_\pm = (\bullet \pm |\bullet|)/2$. The function $\mathfrak{g}(\mathfrak{d})$ is a degradation function that in our formulation takes the form:

$$\mathfrak{g}(\mathfrak{d}) = (1 - \mathfrak{d})^2 + \mathcal{K}, \tag{3.5}$$

where $\mathcal{K}$ is a residual stiffness which is introduced to avoid numerical instabilities and ill-conditioned stiffness matrix when $\mathfrak{d} = 1$. In Eq. (3.4a) the degradation function (Eq. (3.5)) multiplies only the positive counterpart of the elastic energy. In this way the damage is addressed only to the tensile stresses, avoiding damage development in compression.

The split of the strain tensor into its positive and negative counterparts ($\boldsymbol{\varepsilon} = \boldsymbol{\varepsilon}_+ + \boldsymbol{\varepsilon}_-$) is computed making use of the spectral decomposition of the strain tensor:

$$\boldsymbol{\varepsilon}_\pm = \sum_{i=1}^{n_{dim}} \langle \varepsilon^i \rangle_\pm \mathbf{n}_\varepsilon^i \otimes \mathbf{n}_\varepsilon^i, \tag{3.6}$$

where ε^i and $\mathbf{n}_\varepsilon^i$ are, respectively, the eigenvalues and the eigenvectors of the strain tensor.

Finally, the Cauchy stress tensor of the PF formulation takes the form:

$$\boldsymbol{\sigma} := \frac{\partial \hat{\psi}}{\partial \boldsymbol{\varepsilon}} = \mathfrak{g}(\mathfrak{d})\boldsymbol{\sigma}_+ + \boldsymbol{\sigma}_-; \qquad \text{with } \boldsymbol{\sigma}_\pm = \lambda \left(\langle \text{tr}[\boldsymbol{\varepsilon}] \rangle_\pm \right) \mathbf{1} + 2\mu \boldsymbol{\varepsilon}_\pm, \tag{3.7}$$

where $\mathbf{1}$ denotes the second-order identity tensor, and $\sigma_\pm$ denotes the positive-negative counterpart of the stress tensor.

3.1.2 2D finite element formulation and implementation of the PF model for brittle fracture

In this section the PF formulation for brittle fracture is formulated within the framework of the finite element method. The PF is included as constitutive law for a 4-node isoparametric element.

First of all, the weak form of the PF model is derived following the Galerkin procedure. According to the functional defined in Eq. (3.1) we can derive its virtual variation as follows:

$$\begin{aligned} &\delta\Pi_b(\mathbf{u}, \delta\mathbf{u}, \mathfrak{d}, \delta\mathfrak{d}) = \int_\Omega \boldsymbol{\sigma} : \delta\boldsymbol{\varepsilon} \, \mathrm{d}\Omega - \int_\Omega 2(1-\mathfrak{d})\delta\mathfrak{d}\psi_+^e(\boldsymbol{\varepsilon}) \, \mathrm{d}\Omega + \\ &\int_\Omega \mathcal{G}_c^b l \left[\frac{1}{l^2}\mathfrak{d}\delta\mathfrak{d} + \nabla_{\mathbf{x}}\mathfrak{d} \cdot \nabla_{\mathbf{x}}(\delta\mathfrak{d}) \right] \mathrm{d}\Omega + \delta\Pi_{b,\text{ext}}(\mathbf{u}, \delta\mathbf{u}), \\ &\forall \delta\mathbf{u} \in \mathfrak{V}^u, \delta\mathfrak{d} \in \mathfrak{V}^\mathfrak{d} \end{aligned} \tag{3.8}$$

with:

$\mathfrak{V}^u = \left\{ \delta\mathbf{u} \,|\, \mathbf{u} = \overline{\mathbf{u}} \text{ on } \partial\Omega_u, \mathbf{u} \in \mathcal{H}^1 \right\}$

$\mathfrak{V}^\mathfrak{d} = \left\{ \delta\mathfrak{d} \,|\, \delta\mathfrak{d} = 0 \text{ on } \Gamma_b, \mathfrak{d} \in \mathcal{H}^0 \right\}$

where $\delta\mathbf{u}$ is the virtual variation of the displacement vector, and $\delta\mathfrak{d}$ is the virtual variation of the PF variable. The variation of the external contribution to the functional is defined as follows:

$$\delta\Pi_{b,\text{ext}}(\mathbf{u}, \delta\mathbf{u}) = \int_{\partial\Omega} \overline{\mathbf{t}} \cdot \delta\mathbf{u} \, \mathrm{d}\partial\Omega + \int_\Omega \mathbf{f}_v \cdot \delta\mathbf{u} \, \mathrm{d}\Omega. \tag{3.9}$$

The isoparametric element is defined in the bi-unit square domain in the vector space $\boldsymbol{\xi} = \{\xi^1, \xi^2\}$. In this space, the Lagrangian shape functions $N^I(\boldsymbol{\xi})$ are employed in order to interpolate the geometry ($\mathbf{x}$), the displacement field ($\mathbf{u}$), its variation ($\delta\mathbf{u}$) and its linearization ($\Delta\mathbf{u}$):

$$\mathbf{x} \cong \sum_{I=1}^{n} N^I \widetilde{\mathbf{x}}_I = \mathbf{N}\widetilde{\mathbf{x}}; \quad \mathbf{u} \cong \sum_{I=1}^{n} N^I \mathbf{d}_I = \mathbf{N}\mathbf{d}; \tag{3.10}$$

$$\delta\mathbf{u} \cong \sum_{I=1}^{n} N^I \delta\mathbf{d}_I = \mathbf{N}\delta\mathbf{d}; \quad \Delta\mathbf{u} \cong \sum_{I=1}^{n} N^I \Delta\mathbf{d}_I = \mathbf{N}\delta\mathbf{d}, \tag{3.11}$$

where n is the number of nodes per element, $\mathbf{x}_I$ and $\mathbf{d}_I$ are the discrete nodal coordinates and displacements values, respectively, which are collected in the corresponding vectors $\widetilde{\mathbf{x}}$ and $\mathbf{d}$. The operator $\mathbf{N}$ collect the interpolation function at the element level. The displacement-strain operator $\mathbf{B_d}$ is also used in order to define and interpolate the strain field (ε), its variation ($\delta\varepsilon$) and its linearization ($\Delta\varepsilon$):

$$\varepsilon \cong \mathbf{B_d}\mathbf{d}; \quad \delta\varepsilon \cong \mathbf{B_d}\delta\mathbf{d}; \quad \Delta\varepsilon \cong \mathbf{B_d}\Delta\mathbf{d} \tag{3.12}$$

The operator $\mathbf{N}$ is also used to interpolate the PF variable $\mathfrak{d}$, its variation $\delta\mathfrak{d}$ and linearization $\Delta\mathfrak{d}$:

$$\mathfrak{d} \cong \sum_{I=1}^{n} N^I \overline{\mathfrak{d}}_I = \mathbf{N}\overline{\mathfrak{d}}; \quad \delta\mathfrak{d} \cong \sum_{I=1}^{n} N^I \delta\overline{\mathfrak{d}}_I = \mathbf{N}\delta\overline{\mathfrak{d}}; \quad \Delta\mathfrak{d} \cong \sum_{I=1}^{n} N^I \Delta\overline{\mathfrak{d}}_I = \mathbf{N}\delta\overline{\mathfrak{d}}, \tag{3.13}$$

where $\overline{\mathfrak{d}}_I$ is the value of the PF variable at the node level, $\overline{\mathfrak{d}}$ is the vector which collect the nodal PF variable value at the element level.

Finally the operator $\mathbf{B}_\mathfrak{d}$ is defined in order to interpolate the gradient of the PF variable ($\nabla_\mathbf{x}\mathfrak{d}$), its variation ($\nabla_\mathbf{x}\delta\mathfrak{d}$) and linearization ($\nabla_\mathbf{x}\Delta\mathfrak{d}$):

$$\nabla_\mathbf{x}\mathfrak{d} \cong \mathbf{B}_\mathfrak{d}\overline{\mathfrak{d}}; \quad \nabla_\mathbf{x}(\delta\mathfrak{d}) \cong \mathbf{B}_\mathfrak{d}\delta\overline{\mathfrak{d}}; \quad \nabla_\mathbf{x}(\Delta\mathfrak{d}) \cong \mathbf{B}_\mathfrak{d}\Delta\overline{\mathfrak{d}}. \tag{3.14}$$

Considering the interpolation framework herein defined we can write the discretized form of the Eq. (3.8) at the element level (denoted by the superscript el):

$$
\begin{aligned}
&\delta\tilde{\Pi}_b^{el}(\mathbf{d},\delta\mathbf{d},\overline{\mathfrak{d}},\delta\overline{\mathfrak{d}}) = \\
&= \delta\mathbf{d}^{\mathrm{T}}\{\int_{\Omega^{el}}\left[\left((1-\mathfrak{d})^2+\mathcal{K}\right)\mathbf{B}_{\mathbf{d}}^{\mathrm{T}}\boldsymbol{\sigma}_+ + \mathbf{B}_{\mathbf{d}}^{\mathrm{T}}\boldsymbol{\sigma}_-\right]\mathrm{d}\Omega + \\
&- \int_{\partial\Omega^{el}}\mathbf{N}^{\mathrm{T}}\overline{\mathbf{t}}\,\mathrm{d}\partial\Omega - \int_{\Omega^{el}}\mathbf{N}^{\mathrm{T}}\mathbf{f}_v\,\mathrm{d}\Omega\} + \\
&+ \delta\overline{\mathfrak{d}}^{\mathrm{T}}\left\{\int_{\Omega^{el}} -2(1-\mathfrak{d})\mathbf{N}^{\mathrm{T}}\psi_+^e(\boldsymbol{\varepsilon})\,\mathrm{d}\Omega + \int_{\Omega^{el}}\mathcal{G}_c^b l\left(\mathbf{B}_{\mathfrak{d}}^{\mathrm{T}}\nabla_{\mathbf{x}}\mathfrak{d} + \frac{1}{l^2}\mathbf{N}^{\mathrm{T}}\mathfrak{d}\right)\mathrm{d}\Omega\right\} = \\
&= \delta\mathbf{d}^{\mathrm{T}}\mathbf{f}_{\mathbf{d}}^b + \delta\overline{\mathfrak{d}}^{\mathrm{T}}\mathbf{f}_{\mathfrak{d}}^b
\end{aligned}
\tag{3.15}
$$

then the internal $\mathbf{f}_{\mathbf{d},\text{int}}^b$ and external $\mathbf{f}_{\mathbf{d},\text{ext}}^b$ contribution of the residual vector of the displacement field, and the residual vector associated with the PF variable $\mathbf{f}_{\mathfrak{d}}^b$ are defined as:

$$
\mathbf{f}_{\mathbf{d},\text{int}}^b = \int_{\Omega^{el}}\left[\left((1-\mathfrak{d})^2+\mathcal{K}\right)\mathbf{B}_{\mathbf{d}}^{\mathrm{T}}\boldsymbol{\sigma}_+ + \mathbf{B}_{\mathbf{d}}^{\mathrm{T}}\boldsymbol{\sigma}_-\right]\mathrm{d}\Omega, \tag{3.16}
$$

$$
\mathbf{f}_{\mathbf{d},\text{ext}}^b = \int_{\partial\Omega^{el}}\mathbf{N}^{\mathrm{T}}\overline{\mathbf{t}}\,\mathrm{d}\partial\Omega + \int_{\Omega}\mathbf{N}^{\mathrm{T}}\mathbf{f}_v\,\mathrm{d}\Omega, \tag{3.17}
$$

$$
\mathbf{f}_{\mathfrak{d}}^b = \int_{\Omega^{el}} -2(1-\mathfrak{d})\mathbf{N}^{\mathrm{T}}\psi_+^e(\boldsymbol{\varepsilon})\,\mathrm{d}\Omega + \int_{\Omega^{el}}\mathcal{G}_c^b l\left[\mathbf{B}_{\mathfrak{d}}^{\mathrm{T}}\nabla_{\mathbf{x}}\mathfrak{d}\frac{1}{l^2}\mathbf{N}^{\mathrm{T}}\mathfrak{d}\right]\mathrm{d}\Omega, \tag{3.18}
$$

from which the total residual vector of the displacement field can be found as $\mathbf{f}_{\mathbf{d}}^b = \mathbf{f}_{\mathbf{d},\text{ext}}^b - \mathbf{f}_{\mathbf{d},\text{int}}^b$.

The solution scheme herein used is based on a fully coupled monolithic scheme. With respect to the staggered scheme solution used in [40; 50; 51], the monolithic scheme ensure a stronger stability of the solution. Then, the coupled linearized system of equation can be written as:

$$
\begin{bmatrix}\mathbf{K}_{\mathbf{dd}}^b & \mathbf{K}_{\mathbf{d}\mathfrak{d}}^b \\ \mathbf{K}_{\mathfrak{d}\mathbf{d}}^b & \mathbf{K}_{\mathfrak{d}\mathfrak{d}}^b\end{bmatrix}\begin{bmatrix}\Delta\mathbf{d} \\ \Delta\mathfrak{d}\end{bmatrix} = \begin{bmatrix}\mathbf{f}_{\mathbf{d},\text{ext}}^b \\ 0\end{bmatrix} - \begin{bmatrix}\mathbf{f}_{\mathbf{d},\text{int}}^b \\ \mathbf{f}_{\mathfrak{d}}^b\end{bmatrix}. \tag{3.19}
$$

where $\mathbf{K}_{\mathbf{dd}}^b$, $\mathbf{K}_{\mathbf{d}\mathfrak{d}}^b$, $\mathbf{K}_{\mathfrak{d}d}^b$ and $\mathbf{K}_{\mathfrak{d}\mathfrak{d}}^b$ are the stiffness matrices related to the displacement and PF degree of freedom. Further details on the form and components of these matrices can be found in [77].

3.1.3 3D finite element formulation and implementation of the PF method in finite strain solid shells

In this section the PF method is particularized for the case of 3D solid shell elements (Fig. 20). In the solid shell formulation enhanced assumed strain (EAS) technology is used in order to alleviate locking pathologies. In particular, it is adopted the additive decomposition of the Green-Lagrange strain tensor $\mathbf{E} = \mathbf{E}^u + \tilde{\mathbf{E}}$, where $\mathbf{E}^u$ and $\tilde{\mathbf{E}}$ denote the compatible and the incompatible counterparts [78; 79], respectively.

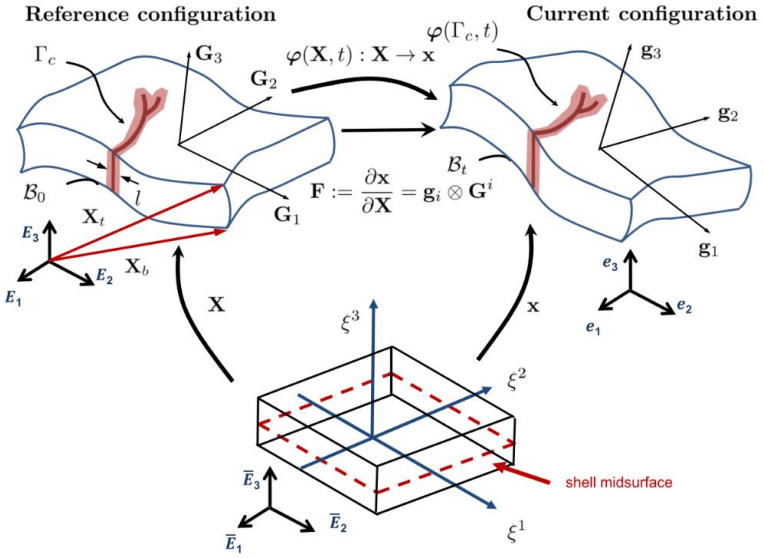

Figure 20: Solid shell element and finite strain kinematic framework.

The formulation is defined trough the Hu-Washizu functional. In this functional the displacements $\mathbf{u}$, the incompatible strains $\tilde{\mathbf{E}}$, the second Piola-Kirchhoff stress tensor $\mathbf{S}$, and the crack phase field variable $\mathfrak{d}$ constitute the independent fields of the formulation. According to the Griffiths theory of brittle fracture, for cracked bodies, this variational formalism in the reference configuration can be expressed as:

$$\Pi(\mathbf{u},\tilde{\mathbf{E}},\mathbf{S},\mathfrak{d}) = \underbrace{\int_{\mathcal{B}_0\setminus\Gamma} \mathfrak{g}(\mathfrak{d})\Psi(\mathbf{E})\,\mathrm{d}\Omega - \int_{\mathcal{B}_0} \mathbf{S}:\tilde{\mathbf{E}}\,\mathrm{d}\Omega}_{\Pi^b_{\text{int}}} + \underbrace{\int_{\Gamma} \mathcal{G}_c\,\mathrm{d}\Gamma}_{\Pi_{\text{fr}}} + \Pi_{\text{ext}}, \tag{3.20}$$

where the internal contribution of the bulk is denoted by Π^b_{int}, whilst Π_{fr} identifies the dissipative contribution due to fracture events. Furthermore, the prescribed external surface and body actions are arranged in the term Π_{ext}. In Eq.(3.20), $\Psi(\mathbf{E})$ is the effective Helmholtz free-energy function in the bulk for undamaged hyperelastic materials and $\mathfrak{g}(\mathfrak{d})$ is the degradation function. $\Psi(\mathbf{E})$ and $\mathfrak{g}(\mathfrak{d})$ satisfies the relations $\mathfrak{g}(0)\Psi(\mathbf{E}) = \Psi(\mathbf{E})$ for undamaged states, and $\mathfrak{g}(1)\Psi(\mathbf{E}) = \mathcal{K}\Psi(\mathbf{E})$ for fully damaged states, being $\mathcal{K} \approx 0$ a residual positive parameter that prevents numerical instabilities [77]. Thus, without loss of generality, we adopt as degradation function $\mathfrak{g}(\mathfrak{d}) = [1-\mathfrak{d}]^2 + \mathcal{K}$. Moreover, it is worth mentioning that the second integral term of Π^b_{int} accounts for the contribution of the second Piola-Kirchhoff stress tensor over the incompatible strains in the view of the EAS method.

Introducing the PF approximation to the dissipated energy counterpart of the functional in Eq. (3.20), it follows:

$$\begin{aligned}\Pi^b(\mathbf{u},\tilde{\mathbf{E}},\mathbf{S},\mathfrak{d}) = &\int_{\mathcal{B}_0\setminus\Gamma} \mathfrak{g}(\mathfrak{d})\Psi(\mathbf{E})\,\mathrm{d}\Omega - \int_{\mathcal{B}_0} \mathbf{S}:\tilde{\mathbf{E}}\,\mathrm{d}\Omega + \\ &+ \int_{\mathcal{B}_0} \mathcal{G}^b_c\gamma(\mathfrak{d},\nabla_{\mathbf{X}}\mathfrak{d})\,\mathrm{d}\Omega + \Pi_{\text{ext}}\end{aligned} \tag{3.21}$$

The corresponding weak form of the functional in Eq. (3.21) is given by the first variation through directional derivative concept with respect to the four independent fields. This leads to the following residual equations:

$$\mathcal{R}^u(\mathbf{u},\delta\mathbf{u},\tilde{\mathbf{E}},\mathbf{S},\mathfrak{d}) = \mathcal{R}^u_{\text{int}} - \mathcal{R}^u_{\text{ext}} = \\ = \int_{\mathcal{B}_0} \mathfrak{g}(\mathfrak{d}) \frac{\partial \Psi}{\partial \mathbf{E}} : \delta\mathbf{E}^u \,\mathrm{d}\Omega + \delta\Pi_{\text{ext}}(\mathbf{u}) = 0, \quad \forall \delta\mathbf{u} \in \mathfrak{V}^u, \tag{3.22}$$

$$\mathcal{R}^{\tilde{E}}(\mathbf{u},\tilde{\mathbf{E}},\delta\tilde{\mathbf{E}},\mathbf{S},\mathfrak{d}) = \int_{\mathcal{B}_0} \mathfrak{g}(\mathfrak{d}) \frac{\partial \Psi}{\partial \mathbf{E}} : \delta\tilde{\mathbf{E}} \,\mathrm{d}\Omega - \int_{\mathcal{B}_0} \mathbf{S} : \delta\tilde{\mathbf{E}} \,\mathrm{d}\Omega = 0, \quad \forall \delta\tilde{\mathbf{E}} \in \mathfrak{V}^{\tilde{E}}, \tag{3.23}$$

$$\mathcal{R}^S(\mathbf{u},\tilde{\mathbf{E}},\mathbf{S},\delta\mathbf{S},\mathfrak{d}) = \int_{\mathcal{B}_0} \delta\mathbf{S} : \tilde{\mathbf{E}} \,\mathrm{d}\Omega = 0, \quad \forall \delta\mathbf{S} \in \mathfrak{V}^S, \tag{3.24}$$

$$\mathcal{R}^{\mathfrak{d}}(\mathbf{u},\tilde{\mathbf{E}},\mathbf{S},\mathfrak{d},\delta\mathfrak{d}) = \\ = \int_{\mathcal{B}_0} -2(1-\mathfrak{d})\delta\mathfrak{d}\Psi(\mathbf{E}) \,\mathrm{d}\Omega + \int_{\mathcal{B}_0} \mathcal{G}_c^b l \left[\frac{1}{l^2}\mathfrak{d}\delta\mathfrak{d} + \nabla_{\mathbf{X}}\mathfrak{d} \cdot \nabla_{\mathbf{X}}(\delta\mathfrak{d}) \right] \mathrm{d}\Omega = 0, \\ \forall \delta\mathfrak{d} \in \mathfrak{V}^{\mathfrak{d}}, \tag{3.25}$$

where $\mathfrak{V}^u = \left\{\delta\mathbf{u} \in [H^1(\mathcal{B}_0)] : \delta\mathbf{u} = \mathbf{0} \text{ on } \partial\mathcal{B}_{0,u}\right\}$ identifies the space of admissible displacement variations; $\mathfrak{V}^{\tilde{E}} = [L_2(\mathcal{B}_0)]$ and $\mathfrak{V}^S = [L_2(\mathcal{B}_0)]$ identify the admissible spaces corresponding to the test functions of the incompatible strain and the stress fields, respectively; and finally $\mathfrak{V}^{\mathfrak{d}} = \{\delta\mathfrak{d} \in \mathcal{H}^1(\mathcal{B}_0) \,|\, \delta\mathfrak{d} = 0 \text{ on } \Gamma_c\}$ is the space of admissible test functions for the crack phase field variable.

Recalling the orthogonality condition for the stress field $\mathbf{S}$ and the enhanced strain field $\tilde{\mathbf{E}}$ [80], the weak form of the boundary value problem associated with the cracked bulk is reduced to the following three field problem

$$\mathcal{R}^u(\mathbf{u},\delta\mathbf{u},\tilde{\mathbf{E}},\mathfrak{d}) = \mathcal{R}^u_{\text{int}} - \mathcal{R}^u_{\text{ext}} = \int_{\mathcal{B}_0} \mathfrak{g}(\mathfrak{d}) \frac{\partial \Psi}{\partial \mathbf{E}} : \delta\mathbf{E}^u \,\mathrm{d}\Omega + \delta\Pi_{\text{ext}}(\mathbf{u}) = 0, \tag{3.26}$$

$$\mathcal{R}^{\tilde{E}}(\mathbf{u},\tilde{\mathbf{E}},\delta\tilde{\mathbf{E}},\mathfrak{d}) = \int_{\mathcal{B}_0} \mathfrak{g}(\mathfrak{d}) \frac{\partial \Psi}{\partial \mathbf{E}} : \delta\tilde{\mathbf{E}} \,\mathrm{d}\Omega = 0, \tag{3.27}$$

$$\mathcal{R}^{\mathfrak{d}}(\mathbf{u},\tilde{\mathbf{E}},\mathfrak{d},\delta\mathfrak{d}) =$$
$$= \int_{\mathcal{B}_0} -2(1-\mathfrak{d})\delta\mathfrak{d}\Psi(\mathbf{E})\,\mathrm{d}\Omega + \int_{\mathcal{B}_0} \mathcal{G}_c^b l\left[\frac{1}{l^2}\mathfrak{d}\delta\mathfrak{d} + \nabla_{\mathbf{X}}\mathfrak{d}\cdot\nabla_{\mathbf{X}}(\delta\mathfrak{d})\right]\,\mathrm{d}\Omega = 0. \tag{3.28}$$

The nonlinear system given in Eqs.(3.26)-(3.28) is solved by means of the standard incremental-iterative Newton-Raphson method. For this purpose, the consistent linearization of these equations can be expressed as

$$\hat{L}[\mathcal{R}^u(\mathbf{u},\delta\mathbf{u},\tilde{\mathbf{E}},\mathfrak{d})]\cdot[\Delta\mathbf{u},\Delta\tilde{\mathbf{E}},\Delta\mathfrak{d}] =$$
$$= \int_{\mathcal{B}_0} \mathfrak{g}(\mathfrak{d})\left[\delta\mathbf{E}^u : \frac{\partial^2\Psi}{\partial\mathbf{E}^2} : \Delta\mathbf{E}^u + \frac{\partial\Psi}{\partial\mathbf{E}} : \Delta\delta\mathbf{E}^u\right]\,\mathrm{d}\Omega +$$
$$+ \int_{\mathcal{B}_0} \mathfrak{g}(\mathfrak{d})\left[\delta\mathbf{E}^u : \frac{\partial^2\Psi}{\partial\mathbf{E}^2} : \Delta\tilde{\mathbf{E}}\right]\,\mathrm{d}\Omega \int_{\mathcal{B}_0} \delta\mathbf{E}^u : \frac{\partial\Psi}{\partial\mathbf{E}}\frac{\partial\mathfrak{g}(\mathfrak{d})}{\partial\mathfrak{d}}\Delta\mathfrak{d}\,\mathrm{d}\Omega, \tag{3.29}$$

$$\hat{L}[\mathcal{R}^{\tilde{E}}(\mathbf{u},\tilde{\mathbf{E}},\delta\tilde{\mathbf{E}},\mathfrak{d})]\cdot[\Delta\mathbf{u},\Delta\tilde{\mathbf{E}},\Delta\mathfrak{d}] =$$
$$= \int_{\mathcal{B}_0} \mathfrak{g}(\mathfrak{d})\left[\delta\tilde{\mathbf{E}} : \frac{\partial^2\Psi}{\partial\mathbf{E}^2} : \Delta\mathbf{E}^u + \delta\tilde{\mathbf{E}} : \frac{\partial^2\Psi}{\partial\mathbf{E}^2} : \Delta\tilde{\mathbf{E}}\right]\,\mathrm{d}\Omega +$$
$$+ \int_{\mathcal{B}_0} \delta\tilde{\mathbf{E}} : \frac{\partial\Psi}{\partial\mathbf{E}}\frac{\partial\mathfrak{g}(\mathfrak{d})}{\partial\mathfrak{d}}\Delta\mathfrak{d}\,\mathrm{d}\Omega, \tag{3.30}$$

$$\hat{L}[\mathcal{R}^{\mathfrak{d}}(\mathbf{u},\tilde{\mathbf{E}},\mathfrak{d},\delta\mathfrak{d})]\cdot[\Delta\mathbf{u},\Delta\tilde{\mathbf{E}},\Delta\mathfrak{d}] =$$
$$= \int_{\mathcal{B}_0} -2(1-\mathfrak{d})\delta\mathfrak{d}\frac{\partial\Psi}{\partial\mathbf{E}} : \Delta\mathbf{E}^u\,\mathrm{d}\Omega +$$
$$+ \int_{\mathcal{B}_0} -2(1-\mathfrak{d})\delta\mathfrak{d}\frac{\partial\Psi}{\partial\mathbf{E}} : \Delta\tilde{\mathbf{E}}\,\mathrm{d}\Omega \int_{\mathcal{B}_0} 2\delta\mathfrak{d}\Psi(\mathbf{E})\Delta\mathfrak{d}\,\mathrm{d}\Omega +$$
$$+ \int_{\mathcal{B}_0} \mathcal{G}_c^b l\left[\frac{1}{l^2}\delta\mathfrak{d}\Delta\mathfrak{d} + \nabla_{\mathbf{X}}\Delta\mathfrak{d}\cdot\nabla_{\mathbf{X}}(\delta\mathfrak{d})\right]\,\mathrm{d}\Omega. \tag{3.31}$$

The first variation of the displacement-derived GreenLagrange strain tensor takes the form

$$\delta \mathbf{E}^u = \frac{1}{2} \left[\delta \mathbf{g}_i \cdot \mathbf{g}_j + \mathbf{g}_i \cdot \delta \mathbf{g}_j \right] \mathbf{G}^i \otimes \mathbf{G}^j, \tag{3.32}$$

whereas its linearized virtual displacement-derived GreenLagrange strain tensor in the convective setting reads

$$\Delta \delta \mathbf{E}^u = \frac{1}{2} \left[\delta \mathbf{g}_i \cdot \Delta \mathbf{g}_j + \Delta \mathbf{g}_i \cdot \delta \mathbf{g}_j \right] \mathbf{G}^i \otimes \mathbf{G}^j. \tag{3.33}$$

The previous derivation leads to a fully coupled system of equations, which is solved according to a monolithic solution scheme [49].

Regarding the material formulation, a hyperelastic neo-Hookean isotropic constitutive response is assumed for the numerical implementation of the current framework, with:

$$\Psi(\mathbf{C}) = \frac{\lambda}{2} \left(\ln J \right)^2 - \mu \ln J + \frac{\mu}{2} \left(\mathrm{tr}[\mathbf{C}] - 3 \right), \tag{3.34a}$$

$$\mathbb{C}(\mathbf{C}) = 4 \partial_{\mathbf{C}\mathbf{C}} \Psi(\mathbf{C}) = \lambda \mathbf{C}^{-1} \otimes \mathbf{C}^{-1} + 2 \left(\lambda \ln J - \mu \right) \frac{\partial \mathbf{C}^{-1}}{\partial \mathbf{C}}, \tag{3.34b}$$

where J identifies the determinant of the deformation gradient $\mathbf{F}$ accounting for the consideration of the incompatible strains [49].

Finally, standard Dirichlet- and Neumann-type boundary conditions are considered for the boundary value problem in the bulk.

For the boundary value problem for the bulk, standard discretization of the domain $\mathcal{B}_0$ is considered to be constructed via n_e non-overlapping elements, such that $\mathcal{B}_0 \approx \bigcup_{e=1}^{n_e} \mathcal{B}_0^{(e)}$. The discretization of the bulk is performed according to the solid shell concept [81; 82], being the parametric space identified as follows: $\mathcal{A} := \{ \boldsymbol{\xi} = (\xi^1, \xi^2, \xi^3) \in \mathbb{R}^3 \mid -1 \leq \xi^i \leq +1; i = 1, 2, 3 \}$, where (ξ^1, ξ^2) denote in-plane directions, whereas ξ^3 identifies the thickness direction and H is the initial shell thickness (Fig. 20).

The reference position vector of any material point is linearly interpolated by the position of the top $\mathbf{X}_t(\xi^1, \xi^2)$ and bottom $\mathbf{X}_b(\xi^1, \xi^2)$ vectors:

$$\mathbf{X}(\boldsymbol{\xi}) = \frac{1}{2} \left(1 + \xi^3 \right) \mathbf{X}_t(\xi^1, \xi^2) + \frac{1}{2} \left(1 - \xi^3 \right) \mathbf{X}_b(\xi^1, \xi^2). \tag{3.35}$$

Similarly, the same interpolation scheme is adopted for the current configuration:

$$\mathbf{x}(\boldsymbol{\xi}) = \frac{1}{2}\left(1+\xi^3\right)\mathbf{x}_t(\xi^1,\xi^2) + \frac{1}{2}\left(1-\xi^3\right)\mathbf{x}_b(\xi^1,\xi^2). \tag{3.36}$$

The previous approximation is also assumed for the PF variable:

$$\mathfrak{d}(\boldsymbol{\xi}) = \frac{1}{2}\left(1+\xi^3\right)\mathfrak{d}_t(\xi^1,\xi^2) + \frac{1}{2}\left(1-\xi^3\right)\mathfrak{d}_b(\xi^1,\xi^2), \tag{3.37}$$

where $\mathfrak{d}_t$ and $\mathfrak{d}_b$ stand for the PF variable values corresponding to the top and bottom surfaces of the body, respectively. This ansazt for the PF variable allows a non-uniform value of this parameter over the shell thickness, as discussed in [49].

Standard trilinear shape functions are used to interpolate the reference and current position vectors:

$$\mathbf{X} = \mathbf{N}(\boldsymbol{\xi})\widetilde{\mathbf{X}} \quad \text{and} \quad \mathbf{x} = \mathbf{N}(\boldsymbol{\xi})\widetilde{\mathbf{x}}, \tag{3.38}$$

where $\mathbf{N}(\boldsymbol{\xi})$ is the matrix operator associated with the shape functions.

Accordingly, the displacement and the phase field variable $(\mathbf{u}, \mathfrak{d})$, their respective variations $(\delta\mathbf{u}, \delta\mathfrak{d})$ and their increments $(\Delta\mathbf{u}, \Delta\mathfrak{d})$ are approximated at the element level as

$$\mathbf{u} \approx \mathbf{N}(\boldsymbol{\xi})\mathbf{d};\ \delta\mathbf{u} \approx \mathbf{N}(\boldsymbol{\xi})\delta\mathbf{d};\ \Delta\mathbf{u} \approx \mathbf{N}(\boldsymbol{\xi})\Delta\mathbf{d}, \tag{3.39}$$

$$\mathfrak{d} = \mathbf{N}(\boldsymbol{\xi})\overline{\mathfrak{d}};\ \delta\mathfrak{d} = \mathbf{N}(\boldsymbol{\xi})\delta\overline{\mathfrak{d}};\ \ \Delta\mathfrak{d} = \mathbf{N}(\boldsymbol{\xi})\Delta\overline{\mathfrak{d}}. \tag{3.40}$$

The interpolation of the incompatible strain field is expressed in terms of the operator $\mathbf{M}(\boldsymbol{\xi})$ that is designed to alleviate membrane and Poisson thickness locking pathologies can be performed by the used of the EAS method. The interpolation of the incompatible strains $\tilde{\mathbf{E}}$, its variation $\delta\tilde{\mathbf{E}}$ and its increment $\Delta\tilde{\mathbf{E}}$ renders

$$\tilde{\mathbf{E}} \approx \mathbf{M}(\boldsymbol{\xi})\boldsymbol{\varsigma},\ \ \delta\tilde{\mathbf{E}} \approx \mathbf{M}(\boldsymbol{\xi})\delta\boldsymbol{\varsigma},\ \ \Delta\tilde{\mathbf{E}} \approx \mathbf{M}(\boldsymbol{\xi})\Delta\boldsymbol{\varsigma}, \tag{3.41}$$

The particular form of the interpolation operator in the local parametric setting ($\tilde{\mathbf{M}}(\boldsymbol{\xi})$) is given by [83]

$$\tilde{\mathbf{M}}(\boldsymbol{\xi}) = \begin{bmatrix} \xi^1 & 0 & 0 & 0 & 0 & 0 & 0 \\ 0 & \xi^2 & 0 & 0 & 0 & 0 & 0 \\ 0 & 0 & \xi^3 & \xi^1\xi^3 & \xi^2\xi^3 & 0 & 0 \\ 0 & 0 & 0 & 0 & 0 & \xi^1 & \xi^2 \\ 0 & 0 & 0 & 0 & 0 & 0 & 0 \\ 0 & 0 & 0 & 0 & 0 & 0 & 0 \end{bmatrix}. \tag{3.42}$$

As discussed in [78; 84], the operator $\tilde{\mathbf{M}}(\boldsymbol{\xi})$ is subsequently transformed into the global Cartesian setting in order to preserve the consistency of the formulation. Furthermore, in the current solid shell model, transverse shear and trapezoidal locking are circumvented through the use of the assumed natural strain method as detailed in [49].

Insertion of the previous discretization schemes into the residual forms given in Eqs.(3.26)–(3.28), and into the corresponding linearized system, Eqs.(3.29)–(3.31), leads to the following coupled system:

$$\begin{bmatrix} \mathbf{k}_{dd} & \mathbf{k}_{d\mathfrak{d}} & \mathbf{k}_{d\varsigma} \\ \mathbf{k}_{\mathfrak{d}d} & \mathbf{k}_{\mathfrak{d}\mathfrak{d}} & \mathbf{k}_{\mathfrak{d}\varsigma} \\ \mathbf{k}_{\varsigma d} & \mathbf{k}_{\varsigma\mathfrak{d}} & \mathbf{k}_{\varsigma\varsigma} \end{bmatrix} \begin{bmatrix} \Delta\mathbf{d} \\ \Delta\bar{\mathfrak{d}} \\ \Delta\boldsymbol{\varsigma} \end{bmatrix} = \begin{bmatrix} \mathbf{R}^d_{\text{ext}} \\ \mathbf{0} \\ \mathbf{0} \end{bmatrix} - \begin{bmatrix} \mathbf{R}^d_{\text{int}} \\ \mathbf{R}^{\mathfrak{d}}_{\text{int}} \\ \mathbf{R}^{\varsigma}_{\text{int}} \end{bmatrix}. \tag{3.43}$$

This system can be reduced due to the static condensation of the incompatible strains at the element level [49], so that the final system reads of equations featuring the coupled scheme between the kinematic and the phase field yields

$$\begin{bmatrix} \mathbf{k}^*_{dd} & \mathbf{k}^*_{d\mathfrak{d}} \\ \mathbf{k}^*_{\mathfrak{d}d} & \mathbf{k}^*_{\mathfrak{d}\mathfrak{d}} \end{bmatrix} \begin{bmatrix} \Delta\mathbf{d} \\ \Delta\bar{\mathfrak{d}} \end{bmatrix} = \begin{bmatrix} \mathbf{R}^d_{\text{ext}} \\ \mathbf{0} \end{bmatrix} - \begin{bmatrix} \mathbf{R}^{d*}_{\text{int}} \\ \mathbf{R}^{\mathfrak{d}*}_{\text{int}} \end{bmatrix} \tag{3.44}$$

where the modified residuals and tangent matrices take the form

$$\mathbf{k}^*_{\text{dd}} = \mathbf{k}_{dd} - \mathbf{k}_{d\varsigma}\mathbf{k}^{-1}_{\varsigma\varsigma}\mathbf{k}_{\varsigma d}, \quad \mathbf{k}^*_{d\mathfrak{d}} = \mathbf{k}_{d\mathfrak{d}} - \mathbf{k}_{d\varsigma}\mathbf{k}^{-1}_{\varsigma\varsigma}\mathbf{k}_{\varsigma\mathfrak{d}}, \tag{3.45}$$

$$\mathbf{k}^{*}_{\mathfrak{d}d} = \mathbf{k}_{\mathfrak{d}d} - \mathbf{k}_{\mathfrak{d}\varsigma}\mathbf{k}^{-1}_{\varsigma\varsigma}\mathbf{k}_{\varsigma d}, \quad \mathbf{k}^{*}_{\mathfrak{d}\mathfrak{d}} = \mathbf{k}_{\mathfrak{d}\mathfrak{d}} - \mathbf{k}_{\mathfrak{d}\varsigma}\mathbf{k}^{-1}_{\varsigma\varsigma}\mathbf{k}_{\varsigma\mathfrak{d}}, \tag{3.46}$$

$$\mathbf{R}^{d*}_{\text{int}} = \mathbf{R}^{d}_{\text{int}} - \mathbf{k}_{d\varsigma}\mathbf{k}^{-1}_{\varsigma\varsigma}\mathbf{R}^{\varsigma}_{\text{int}}, \quad \mathbf{R}^{\mathfrak{d}*}_{\text{int}} = \mathbf{R}^{\mathfrak{d}}_{\text{int}} - \mathbf{k}_{\mathfrak{d}\varsigma}\mathbf{k}^{-1}_{\varsigma\varsigma}\mathbf{R}^{\varsigma}_{\text{int}}. \tag{3.47}$$

The algebraic system in Eq.(3.44) is solved using a monolithic Newton-Raphson procedure, which constitutes a robust scheme for the developed modeling framework.

3.2 The cohesive zone model (CZM)

When a material is not brittle it can show a softening behaviour given by cohesive fracture. The cohesive fracture concept relies on the idea that after the crack tip there is a process zone where the material is damaged but is still able to transfer stress (Fig. 21). Then, at the crack onset the stress is not considered to go immediately to zero. The stress is decreasing slowly as a function of the crack opening. In order to model this phenomenon the so called cohesive zone model (CZM) is used.

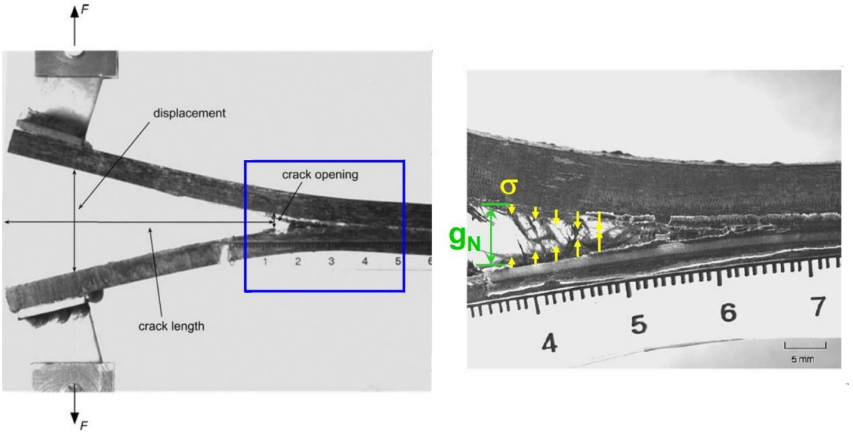

Figure 21: Example of cohesive fracture in double cantilever beam test. With permission from [85]

The first pioneering research regarding the CZM can be attributed to Barenblatt [86]. He formulate a model which overcome the limitation of

small plastic zone and the necessity of a pre-existing defect. This model is able to predict the nonlinear behaviour of the zone ahead of the crack tip caused by plasticity, micro-cracking or other phenomena, with the introduction of a cohesive stress vs. crack separation law in the narrow strip-shaped zone in front of the main crack. The principle parameters that characterized this law are usually the maximum tensile stress $\sigma_{\max}$, the fracture energy G_c and the critical crack opening g_c, the latter determines the starting point of the total decohesion of the material, e.g. the real crack tip. Many of these models have been formulated with different shapes in order to describe crack phenomena in different materials in the three different fracture modes. For instance Needleman used polynomial [87] and exponential formulations [88] to describe the debonding of particles in composite materials with metal matrices:

$$\sigma_I = -\sigma_{\max} \left\{ z\frac{g_{\mathrm{n}}}{\delta} - \beta z^2 \left[1 - cos\left(\frac{2\pi g_{\mathrm{t}}}{g_{\mathrm{c}}} \right) \right] \right\} e^{1-\frac{z g_{\mathrm{n}}}{\delta}} \tag{3.48}$$

where σ_I is the mode I stress, g_{n} the crack opening in mode I, g_{t} the crack opening in mode II and z, β, δ are material parameters. Tvergaard and Hutchinson [89] used a trapezoidal relation to determine crack growth resistance, Geubelle and Baylor [90] used a bilinear equation to determine the crack nucleation and propagation in the matrix of composite materials. Examples of CZM shapes are shown in Fig. 22.

One of the main difficulties in using CZM approaches to describe cohesive fracture is that simple models are preferred to physically meaningful models. This is addressed to the fact that a simple model are more likely to avoid numerical problems in the simulations. Consequently, the identification of the parameters which governs such model is not straightforward. To overcome this problem inverse methods has been proposed. In [91] the result of the numerical simulation are compared with the real measured displacement field. In [92] the shape of the CZM has been retrieved using molecular dynamics simulations. Another attempt to identify the CZM parameters have been made in [93] by considering genetic algorithms and minimizing an objective function involving the global macroscopic response. A method based on the J-integral has

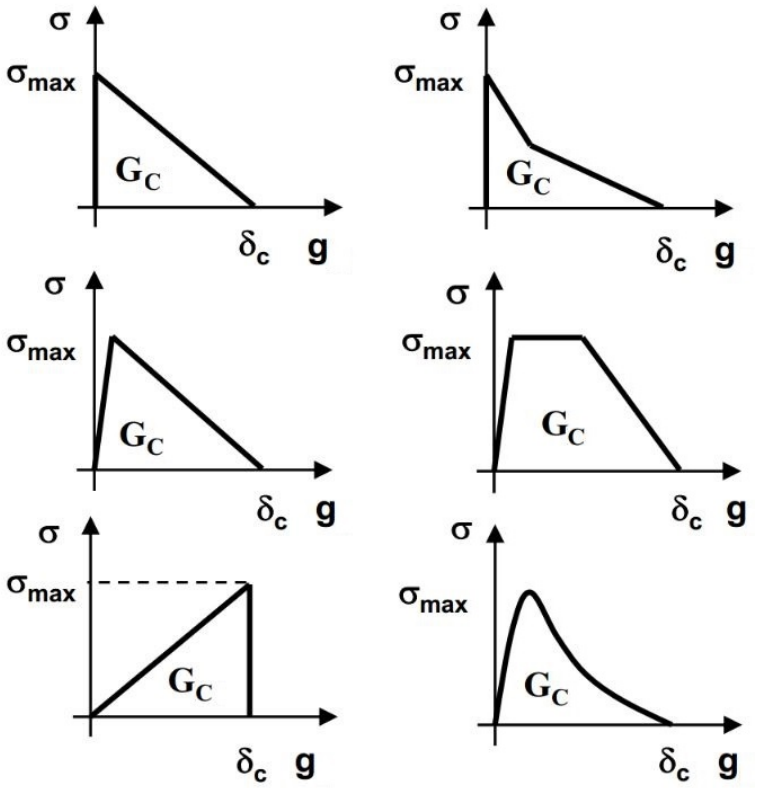

Figure 22: Example of cohesive fracture in double cantilever beam test.

been proposed in [94] to identify the shape of the CZM by monitoring crack propagation in single-edge notched specimens tested inside a SEM chamber.

3.2.1 A CZM compatible with phase field

In this section the formulation of the CZM compatible with the PF model is presented. The two models are coupled at the constitutive level. In this way the effects of the damage in the surrounding bulk is included in the interface. Let's consider a generic body where there are cracks Γ_b and

prescribed interfaces Γ_i (Fig. 23). Both, cracks and interfaces, can evolve and interact.

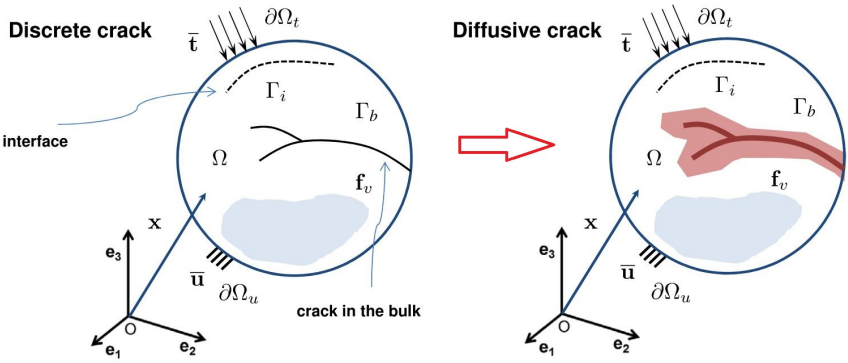

Figure 23: Example of cohesive fracture in double cantilever beam test.

Starting from the vectorial topology defined in Section 3.1.1, we denote a generic point on the interface Γ_i by the vector $\mathbf{x}_c$. Then, we recall the free energy functional which governs the mechanics of the body Ω defined in Eq. (3.1):

$$\Pi(\mathbf{u},\Gamma) = \Pi_\Omega(\mathbf{u},\Gamma) + \Pi_\Gamma(\Gamma) = \int_{\Omega\setminus\Gamma} \psi^e(\boldsymbol{\varepsilon})\,\mathrm{d}\Omega + \int_\Gamma \mathcal{G}_c\,\mathrm{d}\Gamma,$$

The main idea which governs the coupling between the PF approach for brittle fracture and the CZM is to split the fracture energy function $\mathcal{G}_c$ in two parts. One part ($\mathcal{G}_c^b$) which describes fracture in the bulk and that is modelled with the PF approach. The second part ($\mathcal{G}^i$) attains the cohesive opening of the interface and is modelled with the CZM. Then, the free energy functional in Eq. (3.2.1) can be rewritten as follow:

$$\begin{aligned}\Pi(\mathbf{u},\Gamma_b,\Gamma_i) &= \Pi_\Omega + \Pi_{\Gamma_b} + \Pi_{\Gamma_i} = \\ &= \int_{\Omega\setminus\Gamma} \psi^e(\boldsymbol{\varepsilon})\,\mathrm{d}\Omega + \int_{\Gamma_b} \mathcal{G}_c^b(\mathbf{u},\mathfrak{d})\,\mathrm{d}\Gamma + \int_{\Gamma_i} \mathcal{G}^i\left(\mathbf{g},\mathfrak{h},\mathfrak{d}\right)\,\mathrm{d}\Gamma,\end{aligned} \tag{3.49}$$

where $\mathbf{g}$ is the the displacement discontinuities at the interface, $\mathfrak{h}$ is an history parameter as in [95], and $\mathfrak{d}$ is the PF variable.

The classical linear CZM with tension cut-off [96] is particularized in order to take into account the effect of the bulk damage $\mathfrak{d}$. First of all, the cohesive counterpart of the fracture energy in Eq. (3.49) is decomposed into the sum of the Mode I and Mode II fracture energies, $\mathcal{G}_I$ and $\mathcal{G}_{II}$ respectively. In the formulation in [97] the critical opening displacement of the CZM (g_c) depends on the bulk damage $\mathfrak{d}$ according to the linear relation $g_c(\mathfrak{d}) = (1-\mathfrak{d})g_{c,0} + \mathfrak{d}g_{c,1}$, where $g_{c,0} = g_c(\mathfrak{d}=0)$ and $g_{c,1} = g_c(\mathfrak{d}=1)$. Then, the cohesive traction vs separation laws for Mode I and Mode II take the form in Fig. 24, and have equations:

$$\sigma = \begin{cases} k_n \dfrac{g_n}{g_{nc}}, & \text{if } 0 < \dfrac{g_n}{g_{nc}} < 1; \\ 0, & \text{if } \dfrac{g_n}{g_{nc}} \geq 1, \end{cases} \qquad \tau = \begin{cases} k_t \dfrac{g_t}{g_{tc}}, & \text{if } 0 < \dfrac{g_t}{g_{tc}} < 1; \\ 0, & \text{if } \dfrac{g_t}{g_{tc}} \geq 1. \end{cases} \tag{3.50}$$

where σ and τ are the tensions for Mode I and Mode II respectively, g is the opening displacement, and the subscript n and t refers to Mode I and Mode II respectively. The stiffness of the cohesive law k depends on the damage $\mathfrak{d}$ according to the formula:

$$k_n = k_{n,0}\left(\frac{g_{nc,0}}{g_{nc}}\right)^2, \qquad k_t = k_{t,0}\left(\frac{g_{tc,0}}{g_{tc}}\right)^2. \tag{3.51}$$

where k_0 and g_0 are, respectively, the stiffness and critical opening for $\mathfrak{d} = 0$.

In this formulation has been choose to keep constant G_c^i for many reasons. Firstly, the model is formulated starting from the Griffith energy balance criterion, then in Eq. (3) we have a clear and explicit split between the dissipated energy due to bulk fracture and due to interface

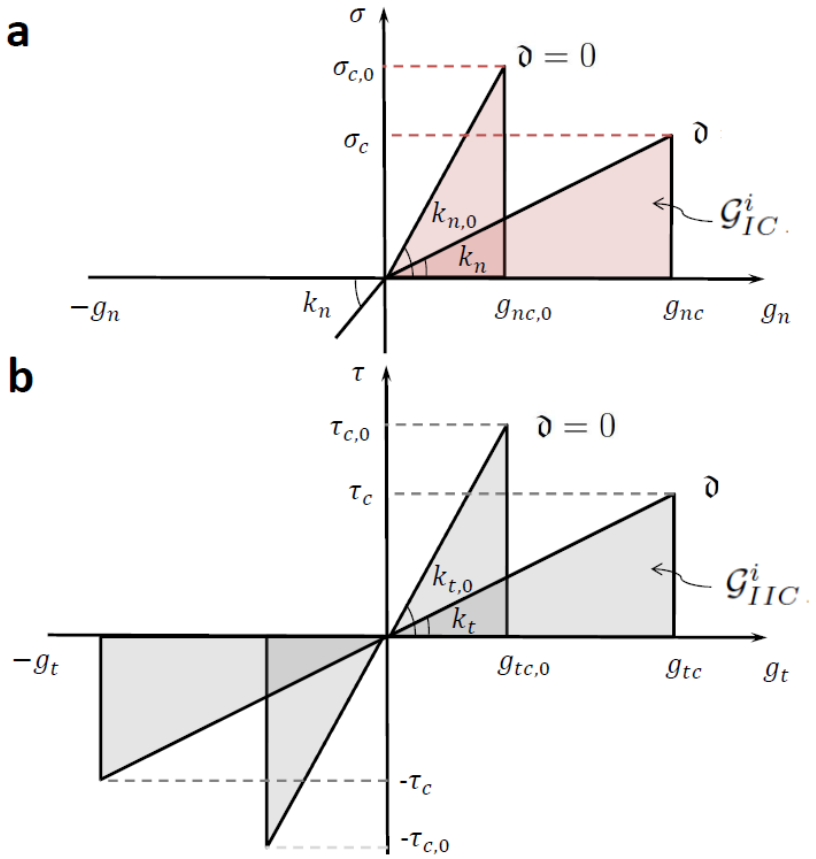

Figure 24: Schematic representation of the traction separation law of the CZM which accounts for the PF variable. (a) Mode I CZM traction σ vs. g_n. (b) Mode II CZM traction τ vs. g_t.

opening. Then, G_c^i becomes the material parameter that governs the interface delamination. This choice make easier the fracture characterization of the interface. In fact, among the four parameter that govern the cohesive law, G_c can be easier to measure from experimental tests [98].

Finally, the mixed mode failure criterion adopted is the one proposed in [99]:

$$\left(\frac{\mathcal{G}_I^i}{\mathcal{G}_{IC}^i}\right)^2 + \left(\frac{\mathcal{G}_{II}^i}{\mathcal{G}_{IIC}^i}\right)^2 = 1, \tag{3.52}$$

where $\mathcal{G}_I^i$ and $\mathcal{G}_{II}^i$ are the dissipated fracture energies which take the form:

$$\begin{aligned}
\mathcal{G}_I^i(\mathfrak{d}) &= \frac{1}{2} n_{t,0} g_n^2 \frac{g_{nc,0}^2}{\left[(1-\mathfrak{d}) g_{nc,0} + \mathfrak{d} g_{nc,1}\right]^2}, \\
\mathcal{G}_{II}^i(\mathfrak{d}) &= \frac{1}{2} k_{t,0} g_t^2 \frac{g_{tc,0}^2}{\left[(1-\mathfrak{d}) g_{tc,0} + \mathfrak{d} g_{tc,1}\right]^2}.
\end{aligned} \tag{3.53}$$

These dissipated fracture energies are compared in Eq. (3.52) with the critical fracture energies $\mathcal{G}_{IC}^i$ and $\mathcal{G}_{IIC}^i$, which have constant value and take the form:

$$\mathcal{G}_{IC}^i = \frac{1}{2} g_{nc,0}^2 k_{n,0}, \qquad \mathcal{G}_{IIC}^i = \frac{1}{2} g_{tc,0}^2 k_{t,0}. \tag{3.54}$$

2D finite element formulation and implementation of the CZM compatible with the PF model

The constitutive formulation presented in the previous Section is now formulated and implemented in a 4-node isoparametric interface finite element (Fig. 25). In analogy with the PF formulation we derive the variation of the functional Π_{Γ_i} defined in Eq.(3.49):

$$\begin{aligned}
&\delta\Pi_{\Gamma_i}(\mathbf{u}, \delta\mathbf{u}, \mathfrak{d}, \delta\mathfrak{d}) = \int_{\Gamma_i} \left(\frac{\partial \mathcal{G}^i(\mathbf{u}, \mathfrak{d})}{\partial \mathbf{u}} \delta\mathbf{u} + \frac{\partial \mathcal{G}^i(\mathbf{u}, \mathfrak{d})}{\partial \mathfrak{d}} \delta\mathfrak{d} \right) \mathrm{d}\Gamma, \\
&\forall \delta\mathbf{u} \in \mathfrak{V}^u, \delta\mathfrak{d} \in \mathfrak{V}^{\mathfrak{d}}
\end{aligned} \tag{3.55}$$

where the variation of the displacement and of the PF variable are the same defined in Eq. (3.8). Taking as base the discretization scheme defined in Section 3.1.2, we introduce other vectors and operators needed for the formulation of the interface element.

First of all, it is defined the vector $\mathbf{g}$ which, for any point in the element Γ_i^{el}, gives the gap between opposing points of the interface flanks. This vector is related to the nodal displacement vector $\mathbf{d}$ through the interface compatibility operator $\hat{\mathbf{B}}_{\mathbf{d}}$ as follows:

$$\mathbf{g} = \mathbf{NLd} = \hat{\mathbf{B}}_{\mathbf{d}}\mathbf{d}, \tag{3.56}$$

where $\mathbf{N}$ is the shape function matrix defined in Eq. (3.10), and $\mathbf{L}$ is a matrix operator.

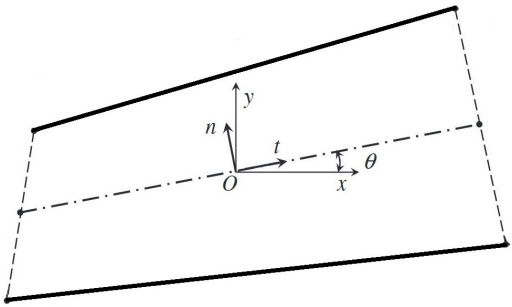

Figure 25: 2D interface element.

In order to apply the traction-separation law of the CZM, the gap vector $\mathbf{g}$ in Eq.(3.56) has to be expressed in terms of the global reference setting, and therefore a transformation from the local interface system is required. The local reference system is defined at the element level by the normal and tangential unit vectors at the interface [21; 100] (Fig. 25). Then, the local gap vector $\mathbf{g}_{\text{loc}}$ is defined as follows:

$$\mathbf{g}_{\text{loc}} \cong \mathbf{Rg} = \mathbf{R}\hat{\mathbf{B}}_{\mathfrak{b}}\mathbf{d}. \tag{3.57}$$

where $\mathbf{R}$ is the rotation matrix.

Regarding the discretization of the PF variable $\mathfrak{d}$ at the element level Γ_i^{el}, the following expression is introduced:

$$\mathfrak{d} \cong \mathbf{N}_{\mathfrak{d}}\mathbf{M}_{\mathfrak{d}}\bar{\mathfrak{d}} = \hat{\mathbf{B}}_{\mathfrak{d}}\bar{\mathfrak{d}}, \tag{3.58}$$

where $\mathbf{M}_\mathfrak{d}$ is the average operator and $\hat{\mathbf{B}}_\mathfrak{d}$ is the compatible operator corresponding to the PF variable. We refer to [100; 101] for the detailed form of the operators herein defined.

Making use of the discretization scheme herein defined for the interface element formulation, Eq. (3.55) can be written in its discretized form. Considering the discretization of the domain at the element level Γ_i^{el} (with $\Gamma_i \sim \bigcup \Gamma_i^{el}$), the discretized functional takes the form:

$$
\begin{aligned}
&\delta\tilde{\Pi}^{el}_{\Gamma_i}(\mathbf{d}, \delta\mathbf{d}, \bar{\mathfrak{d}}, \delta\bar{\mathfrak{d}}) = \\
&= \int_{\Gamma_i^{el}} \left(\frac{\partial \mathcal{G}^i(\mathbf{d}, \bar{\mathfrak{d}})}{\partial \mathbf{d}} \delta\mathbf{d} + \frac{\partial \mathcal{G}^i(\mathbf{d}, \bar{\mathfrak{d}})}{\partial \bar{\mathfrak{d}}} \delta\bar{\mathfrak{d}} \right) \mathrm{d}\Gamma = \\
&= \delta\mathbf{d}^{\mathrm{T}} \int_{\Gamma_i^{el}} \left(\frac{\partial \mathcal{G}^i(\mathbf{d}, \bar{\mathfrak{d}})}{\partial \mathbf{d}} \right)^{\mathrm{T}} \mathrm{d}\Gamma + \delta\bar{\mathfrak{d}}^{\mathrm{T}} \int_{\Gamma_i^{el}} \left(\frac{\partial \mathcal{G}^i(\mathbf{d}, \bar{\mathfrak{d}})}{\partial \bar{\mathfrak{d}}} \right)^{\mathrm{T}} \mathrm{d}\Gamma = \\
&= \delta\mathbf{d}^{\mathrm{T}} \int_{\Gamma_i^{el}} \hat{\mathbf{B}}_{\mathbf{d}}^{\mathrm{T}} \mathbf{R}^{\mathrm{T}} \left(\frac{\partial \mathcal{G}^i(\mathbf{d}, \bar{\mathfrak{d}})}{\partial \mathbf{g}_{\mathrm{loc}}} \right)^{\mathrm{T}} \mathrm{d}\Gamma + \delta\bar{\mathfrak{d}}^{\mathrm{T}} \int_{\Gamma_i^{el}} \hat{\mathbf{B}}_{\mathfrak{d}}^{\mathrm{T}} \left(\frac{\partial \mathcal{G}^i(\mathbf{d}, \bar{\mathfrak{d}})}{\partial \bar{\mathfrak{d}}} \right)^{\mathrm{T}} \mathrm{d}\Gamma
\end{aligned}
\tag{3.59}
$$

From which we can define the residual as follows:

$$
\mathbf{f}^i_{\mathbf{d}} = \int_{\Gamma_i^{el}} \hat{\mathbf{B}}_{\mathbf{d}}^{\mathrm{T}} \mathbf{R}^{\mathrm{T}} \left(\frac{\partial \mathcal{G}^i(\mathbf{d}, \bar{\mathfrak{d}})}{\partial \mathbf{g}_{\mathrm{loc}}} \right)^{\mathrm{T}} \mathrm{d}\Gamma, \tag{3.60a}
$$

$$
\mathbf{f}^i_{\mathfrak{d}} = \int_{\Gamma_i^{el}} \hat{\mathbf{B}}_{\mathfrak{d}}^{\mathrm{T}} \left(\frac{\partial \mathcal{G}^i(\mathbf{d}, \bar{\mathfrak{d}})}{\partial \mathfrak{d}} \right)^{\mathrm{T}} \mathrm{d}\Gamma. \tag{3.60b}
$$

Similarly to the PF formulation, the operators needed for a fully-coupled implicit solution are found. Then, the tangent stiffness matrix

component are derived from the linearization of the residual vectors:

$$\mathbf{K}^i_{\mathbf{dd}} = \frac{\partial \mathbf{f_d}}{\partial \mathbf{d}} = \int_{\Gamma^{el}_i} \hat{\mathbf{B}}^{\mathrm{T}}_{\mathbf{d}} \mathbf{R}^{\mathrm{T}} \mathbb{C}^i_{\mathbf{dd}} \mathbf{R} \hat{\mathbf{B}}_{\mathbf{d}} \, \mathrm{d}\Gamma, \tag{3.61a}$$

$$\mathbf{K}^i_{\mathbf{d}\mathfrak{d}} = \frac{\partial \mathbf{f_d}}{\partial \mathfrak{d}} = \int_{\Gamma^{el}_i} \hat{\mathbf{B}}^{\mathrm{T}}_{\mathbf{d}} \mathbf{R}^{\mathrm{T}} \mathbb{C}^i_{\mathbf{d}\mathfrak{d}} \hat{\mathbf{B}}_{\mathfrak{d}} \, \mathrm{d}\Gamma, \tag{3.61b}$$

$$\mathbf{K}^i_{\mathfrak{d}\mathbf{d}} = \frac{\partial \mathbf{f}_{\mathfrak{d}}}{\partial \mathbf{d}} = \int_{\Gamma^{el}_i} \hat{\mathbf{B}}^{\mathrm{T}}_{\mathfrak{d}} \mathbb{C}^i_{\mathfrak{d}d} \mathbf{R} \hat{\mathbf{B}}_{\mathbf{d}} \, \mathrm{d}\Gamma, \tag{3.61c}$$

$$\mathbf{K}^i_{\mathfrak{d}\mathfrak{d}} = \frac{\partial \mathbf{f}_{\mathfrak{d}}}{\partial \mathfrak{d}} = \int_{\Gamma^{el}_i} \hat{\mathbf{B}}^{\mathrm{T}}_{\mathfrak{d}} \mathbb{C}^i_{\mathfrak{d}\mathfrak{d}} \hat{\mathbf{B}}_{\mathfrak{d}} \, \mathrm{d}\Gamma, \tag{3.61d}$$

where, for the traction-separation law herein proposed, the tangent constitutive operators takes the form:

$$\mathbb{C}^i_{dd} = \begin{bmatrix} \hat{\alpha} k_n & 0 \\ 0 & \hat{\beta} k_t \end{bmatrix}, \tag{3.62a}$$

$$\mathbb{C}^i_{\mathbf{d}\mathfrak{d}} = \left[g_n k_n \frac{\partial \hat{\alpha}}{\partial \mathfrak{d}}, g_t k_t \frac{\partial \hat{\beta}}{\partial \mathfrak{d}} \right], \tag{3.62b}$$

$$\mathbb{C}^i_{\mathfrak{d}\mathbf{d}} = \begin{bmatrix} g_n k_n \dfrac{\partial \hat{\alpha}}{\partial \mathfrak{d}} \\ g_t k_t \dfrac{\partial \hat{\beta}}{\partial \mathfrak{d}} \end{bmatrix}, \tag{3.62c}$$

$$\mathbb{C}^i_{\mathfrak{d}\mathfrak{d}} = \frac{1}{2} g_n^2 k_n \frac{\partial^2 \hat{\alpha}}{\partial \mathfrak{d}^2} + \frac{1}{2} g_t^2 k_t \frac{\partial^2 \hat{\beta}}{\partial \mathfrak{d}^2}. \tag{3.62d}$$

with:

$$\hat{\alpha} = \frac{g^2_{nc,0}}{\left[(1-\mathfrak{d}) g_{nc,0} + \mathfrak{d} g_{nc,1} \right]^2}, \tag{3.63a}$$

$$\hat{\beta} = \frac{g^2_{tc,0}}{\left[(1-\mathfrak{d}) g_{tc,0} + \mathfrak{d} g_{tc,1} \right]^2}. \tag{3.63b}$$

Finally, the linearized system of equation which couple the displacement field with the PF variable takes the form:

$$\begin{bmatrix} \mathbf{K}^i_{\mathbf{dd}} & \mathbf{K}^i_{\mathbf{d}\mathfrak{d}} \\ \mathbf{K}^i_{\mathfrak{d}\mathbf{d}} & \mathbf{K}^i_{\mathfrak{d}\mathfrak{d}} \end{bmatrix} \begin{bmatrix} \Delta\mathbf{d} \\ \Delta\mathfrak{d} \end{bmatrix} = \begin{bmatrix} \mathbf{f}^i_d \\ \mathbf{f}^i_{\mathfrak{d}} \end{bmatrix}. \tag{3.64}$$

3.2.2 3D finite element formulation and implementation of the CZM compatible with the PF model in finite strain interface elements

The postulation of a 3D interface formulation in the framework of the finite strain is a direct extension of the 2D small strain formulation. We consider a generic shell with cracks and prescribed interface as is shown in Fig. 26 (a). We recall the hypothesis introduced in Section 3.2.1 in which the dissipative part of the energy functional is split in a bulk contribution and an interface contribution (Eq. (3.49)). We introduce the same hypothesis in the Hu-Washizu functional defined in Eq. (3.20) and it follows:

$$\begin{aligned} \Pi(\mathbf{u}, \tilde{\mathbf{E}}, \mathbf{S}, \mathfrak{d}) = &\int_{\mathcal{B}_0 \setminus \Gamma} \mathfrak{g}(\mathfrak{d}) \Psi(\mathbf{E}) \, \mathrm{d}\Omega - \int_{\mathcal{B}_0} \mathbf{S} : \tilde{\mathbf{E}} \, \mathrm{d}\Omega + \\ &+ \underbrace{\int_{\mathcal{B}_0} \mathcal{G}^b_c \gamma(\mathfrak{d}, \nabla_{\mathbf{X}} \mathfrak{d}) \, \mathrm{d}\Omega}_{\Pi^b_{\text{fr}}} + \underbrace{\int_{\Gamma_i} \mathcal{G}^i_c(\mathbf{u}, \mathfrak{d}) \, \mathrm{d}\Gamma}_{\Pi^i_{\text{fr}}} + \Pi_{\text{ext}}, \end{aligned} \tag{3.65}$$

where the interface contribution is defined as:

$$\Pi^i(\mathbf{u}, \mathfrak{d}) = \int_{\Gamma_i} \mathcal{G}^i_c(\mathbf{u}, \mathfrak{d}) \, \mathrm{d}\Gamma. \tag{3.66}$$

With respect to the 2D small strain formulation, we have to include the contribution of the fracture in Mode III within the tensorial framework of the finite strain formulation. Then, the constitutive response for fracture Mode I (see Fig. 26 (b) for a generic fracture Mode) reads:

$$S_n = \begin{cases} k_n \dfrac{g_n}{g_{nc}}, & \text{if } 0 < \dfrac{g_n}{g_{nc}} < 1; \\ 0, & \text{if } \dfrac{g_n}{g_{nc}} \geq 1, \end{cases} \tag{3.67}$$

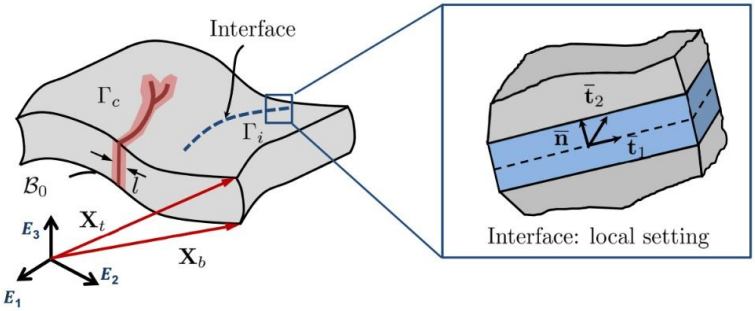

(a)

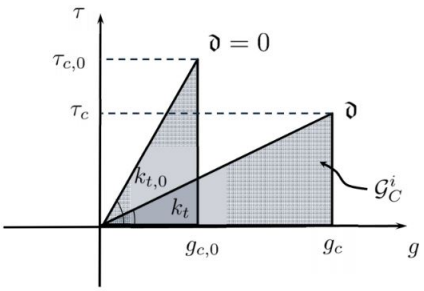

(b)

Figure 26: (a) generic shell body with cracks and prescribed interfaces; (b) generic Mode traction-separation law.

where S_n identifies the normal Piola traction component of the interface, being S_c its corresponding critical value; k_n is the interface stiffness, whereas g_n and g_{nc} are the normal displacement gap and its critical value in the local setting of the interface. Note that the previous cohesive law is further equipped by a penalty formulation in compression with the aim of precluding the inter-penetration of the corresponding flanks.

The interface response given in Eq.(3.67) is further extended for fracture Modes II and III, which obey the following relationships:

$$S_{t1} = \begin{cases} k_{t1}\dfrac{g_{t1}}{g_{t1c}}, & \text{if } 0 < \dfrac{g_{t1}}{g_{t1c}} < 1; \\ 0, & \text{if } \dfrac{g_{t1}}{g_{t1c}} \geq 1, \end{cases} \qquad S_{t2} = \begin{cases} k_{t2}\dfrac{g_{t2}}{g_{t2c}}, & \text{if } 0 < \dfrac{g_{t2}}{g_{t2c}} < 1; \\ 0, & \text{if } \dfrac{g_{t2}}{g_{t2c}} \geq 1, \end{cases} \tag{3.68}$$

In Eq.(3.68), S_{t1} and S_{t2} stand for the tangential Piola traction components associated with the fracture Modes II and III, respectively, whose corresponding critical values are denoted as S_{t1c} and S_{t2c}. The interface stiffness properties for fracture Modes II and III are given by k_{t1} and k_{t2}, respectively. Moreover, g_{t1} and g_{t1c} are the tangential displacement gap and its critical value for fracture Mode II, whilst g_{t2} and g_{t2c} stand for the same quantities for fracture Mode III.

Relying on the previous considerations, the fracture energies for Modes I, II and III render:

$$\begin{aligned} \mathcal{G}^i_{IC} &= \frac{1}{2} S_n g_{nc} = \frac{1}{2} k_n g^2_{nc}; \\ \mathcal{G}^i_{IIC} &= \frac{1}{2} S_{t1} g_{t1c} = \frac{1}{2} k_{t1} g^2_{t1c}; \\ \mathcal{G}^i_{IIIC} &= \frac{1}{2} S_{t2} g_{t2c} = \frac{1}{2} k_{t2} g^2_{t2c}. \end{aligned} \tag{3.69}$$

Similarly to the 2D case, we recall that the critical openings triggering the interface failure are function of $\hat{\mathfrak{d}}_i$ but keeping constant the critical energy release rate for each fracture Mode. We consider that the critical gap at the interfaces increases as the PF variable of the adjoining bulk evolves from 0 to 1. Thus, the following relationship to express the dependency of the critical gaps upon $\hat{\mathfrak{d}}_i$ can be proposed:

$$g_{ic}(\mathfrak{d}_i) = (1 - \mathfrak{d}_i) g_{ic,0} + \mathfrak{d}_i g_{ic,1}, \quad \text{with } i = n, t1, t2. \tag{3.70}$$

In Eq.(3.70), $g_{ic,0}$ and $g_{ic,1}$ denote the critical gaps for the states corresponding to undamaged ($\mathfrak{d}_i = 0$) and fully damaged ($\mathfrak{d}_i = 1$) surrounding bulk. Through the imposition that the fracture energies for each Mode is independent of the crack phase field value, a closed-form expression for the interface stiffnesses can be obtained by equating the

fracture energies for an arbitrary value of $\mathfrak{d}_i$ and for $\mathfrak{d}_i = 0$:

$$k_n = k_{n,0}\left(\frac{g_{nc,0}}{g_{nc}}\right)^2, \quad k_{t1} = k_{t1,0}\left(\frac{g_{t1c,0}}{g_{t1c}}\right)^2, \quad k_{t2} = k_{t2,0}\left(\frac{g_{t2c,0}}{g_{t2c}}\right)^2, \tag{3.71}$$

where $k_{n,0}$, $k_{t1,0}$ and $k_{t2,0}$ are the interface stiffness for intact surrounding bulk ($\hat{\mathfrak{d}}_i = 0$) for the fracture Modes I, II and III, respectively. Their corresponding values for a generic damage state in the bulk $\mathfrak{d}_i$ are denoted by k_n, k_{t1} and k_{t2}.

Therefore, the following closed-form expressions for the Modes I, II and III energy release rates can be derived:

$$\mathcal{G}_I^i(\mathfrak{d}_i) = \frac{1}{2}k_{n,0}g_n^2\frac{g_{nc,0}^2}{\left[(1-\mathfrak{d}_i)g_{nc,0} + \mathfrak{d}_i g_{nc,1}\right]^2}, \tag{3.72}$$

$$\mathcal{G}_{II}^i(\mathfrak{d}_i) = \frac{1}{2}k_{t1,0}g_t^2\frac{g_{t1c,0}^2}{\left[(1-\mathfrak{d}_i)g_{t1c,0} + \mathfrak{d}_i g_{t1c,1}\right]^2}, \tag{3.73}$$

$$\mathcal{G}_{III}^i(\mathfrak{d}_i) = \frac{1}{2}k_{t2,0}g_{t2}^2\frac{g_{t2c,0}^2}{\left[(1-\mathfrak{d}_i)g_{t2c,0} + \mathfrak{d}_i g_{t2c,1}\right]^2}. \tag{3.74}$$

Without loss of generality, a standard quadratic criterion to trigger the interface failure under Mixed Mode fracture conditions is adopted, to couple the modes of fracture:

$$\left(\frac{\mathcal{G}_I^i}{\mathcal{G}_{IC}^i}\right)^2 + \left(\frac{\mathcal{G}_{II}^i}{\mathcal{G}_{IIC}^i}\right)^2 + \left(\frac{\mathcal{G}_{III}^i}{\mathcal{G}_{IIIC}^i}\right)^2 = 1. \tag{3.75}$$

Finally, the following tangent constitutive operators at the interface

are required for the subsequent numerical treatment via nonlinear FEM:

$$\frac{\partial^2 \mathcal{G}_c^i}{\partial \mathbf{g}_{\text{loc}}^2} = \begin{bmatrix} \hat{\alpha} k_n & 0 & 0 \\ 0 & \hat{\beta} k_{t1} & 0 \\ 0 & 0 & \hat{\gamma} k_{t2} \end{bmatrix}, \tag{3.76a}$$

$$\frac{\partial^2 \mathcal{G}_c^i}{\partial \mathbf{g}_{\text{loc}} \partial \hat{\mathfrak{d}}_i} = \begin{bmatrix} g_n k_n \dfrac{\partial \hat{\alpha}}{\partial \hat{\mathfrak{d}}_i} & g_{t1} k_{t1} \dfrac{\partial \hat{\beta}}{\partial \hat{\mathfrak{d}}_i} & g_{t2} k_{t2} \dfrac{\partial \hat{\gamma}}{\partial \hat{\mathfrak{d}}_i} \end{bmatrix}, \tag{3.76b}$$

$$\frac{\partial^2 \mathcal{G}_c^i}{\partial \hat{\mathfrak{d}}_i \partial \mathbf{g}_{\text{loc}}} = \begin{bmatrix} g_n k_n \dfrac{\partial \hat{\alpha}}{\partial \hat{\mathfrak{d}}_i} \\ g_{t1} k_{t1} \dfrac{\partial \hat{\beta}}{\partial \hat{\mathfrak{d}}_i} \\ g_{t2} k_{t2} \dfrac{\partial \hat{\gamma}}{\partial \hat{\mathfrak{d}}_i} \end{bmatrix}, \tag{3.76c}$$

$$\frac{\partial^2 \mathcal{G}_c^i}{\partial \delta \hat{\mathfrak{d}}_i^2} = \frac{1}{2} g_n^2 k_n \frac{\partial^2 \hat{\alpha}}{\partial \hat{\mathfrak{d}}_i^2} + \frac{1}{2} g_{t1}^2 k_{t1} \frac{\partial^2 \hat{\beta}}{\partial \hat{\mathfrak{d}}_i^2} + \frac{1}{2} g_{t2}^2 k_{t2} \frac{\partial^2 \hat{\gamma}}{\partial \hat{\mathfrak{d}}_i^2}. \tag{3.76d}$$

In the previous derivations, the terms $\hat{\alpha}$, $\hat{\beta}$ and $\hat{\gamma}$ are given by

$$\hat{\alpha} = \frac{g_{nc,0}^2}{\left[(1-\mathfrak{d}_i) g_{nc,0} + \mathfrak{d}_i g_{nc,1}\right]^2}, \tag{3.77a}$$

$$\hat{\beta} = \frac{g_{t1c,0}^2}{\left[(1-\mathfrak{d}_i) g_{t1c,0} + \mathfrak{d}_i g_{t1c,1}\right]^2} \tag{3.77b}$$

$$\hat{\gamma} = \frac{g_{t2c,0}^2}{\left[(1-\mathfrak{d}_i) g_{t2c,0} + \mathfrak{d}_i g_{t2c,1}\right]^2} \tag{3.77c}$$

Finally, note that due to the lack of reliable experimental data, the previous formulation can be simplified by assuming the same interface response for fracture Modes II and III.

Finite element formulation and implementation

The point of departure of the weak form of the interface contribution is the term Π^i in Eq.(3.66). In the following, we refer to the derivation of the displacement field $\mathbf{u}_i$ and the crack phase field $\mathfrak{d}_i$, which are associated with the two flanks of the interface. Correspondingly, the local displacement gap vector on the midsurface of the interface $\mathbf{g}_{\text{loc}}$ can be computed

by means of a suitable difference operator $\mathbf{L}$ [52], and a rotation operator $\mathbf{R}(\mathbf{u}_i)$:

$$\mathbf{g}_{\text{loc}} = \mathbf{R}(\mathbf{u}_i)\mathbf{L}\mathbf{u}_i \tag{3.78}$$

The previous transformation is required due to the fact that most of the interface formulations employ a local setting to trigger the relative gaps between the two flanks to distinguish fracture Modes for nonlinear constitutive models [102; 103]. The variation $\delta\mathbf{g}_{\text{loc}}$ and the increment $\Delta\mathbf{g}_{\text{loc}}$ of the local gap vector render

$$\begin{aligned}\delta\mathbf{g}_{\text{loc}} &= \left[\frac{\partial\mathbf{R}(\mathbf{u}_i)}{\partial\mathbf{u}_i}\mathbf{L}\mathbf{u}_i + \mathbf{R}(\mathbf{u}_i)\mathbf{L}\right]\delta\mathbf{u}_i;\\ \Delta\mathbf{g}_{\text{loc}} &= \left[\frac{\partial\mathbf{R}(\mathbf{u}_i)}{\partial\mathbf{u}_i}\mathbf{L}\mathbf{u}_i + \mathbf{R}(\mathbf{u}_i)\mathbf{L}\right]\Delta\mathbf{u}_i\end{aligned} \tag{3.79}$$

Note that an additional geometric term stems from the linearized virtual local gap $\Delta\delta\mathbf{g}_{\text{loc}}$:

$$\Delta\delta\mathbf{g}_{\text{loc}} = \left[\frac{\partial^2\mathbf{R}(\mathbf{u}_i)}{\partial\mathbf{u}_i^2}\mathbf{L}\mathbf{u}_i\delta\mathbf{u}_i + 2\frac{\partial\mathbf{R}(\mathbf{u}_i)}{\partial\mathbf{u}_i}\mathbf{L}\delta\mathbf{u}_i\right]\Delta\mathbf{u}_i \approx \left[2\frac{\partial\mathbf{R}(\mathbf{u}_i)}{\partial\mathbf{u}_i}\mathbf{L}\delta\mathbf{u}_i\right]\Delta\mathbf{u}_i \tag{3.80}$$

As addressed in [101], to simplify the current interface model, the second derivative of the rotation matrix with respect to the displacement field can be neglected due to its minor representativeness. Moreover, the derivative of the Jacobian, which defines the measure of the element length, will also be neglected due to its minor contribution, as rigorously shown in [104].

The PF variable is averaged along the midsurface between the two flanks as follows: $\hat{\mathfrak{d}}_i = \mathbf{L}\mathfrak{d}_i$. Then, the corresponding variation $\delta\hat{\mathfrak{d}}_i$ and increment of the averaged crack phase field variable at the interface reads:

$$\delta\hat{\mathfrak{d}}_i = \mathbf{M}\delta\mathfrak{d}_i; \quad \Delta\hat{\mathfrak{d}}_i = \mathbf{M}\Delta\mathfrak{d}_i \tag{3.81}$$

Based on Eq.(3.66), the first variation of Π^i with respect to the two independent fields yields the following residual equations:

$$\mathcal{R}^{\overline{u}_i}(\mathbf{u}_i, \delta\mathbf{u}_i, \hat{\mathfrak{d}}_i) = \int_{\Gamma_i}\left[\delta\mathbf{g}_{\text{loc}}\right]^{\mathrm{T}}\left[\frac{\partial\mathcal{G}_c^i}{\partial\mathbf{g}_{\text{loc}}}\right]\mathrm{d}\Gamma, \tag{3.82}$$

$$\mathcal{R}^{\hat{\mathfrak{d}}_i}(\mathbf{u}_i, \hat{\mathfrak{d}}_i, \delta\hat{\mathfrak{d}}_i) = \int_{\Gamma_i} \left[\delta\hat{\mathfrak{d}}_i\right]^{\mathrm{T}} \left[\frac{\partial \mathcal{G}_c^i}{\partial \hat{\mathfrak{d}}_i}\right] \mathrm{d}\Gamma. \tag{3.83}$$

The consistent linearization of the residual forms given in Eqs.(3.82)–(3.83) yields:

$$\begin{aligned}
&\hat{L}[\mathcal{R}^{\overline{u}_i}(\mathbf{u}_i, \delta\mathbf{u}_i, \hat{\mathfrak{d}}_i)] \cdot [\Delta\mathbf{u}_i, \Delta\hat{\mathfrak{d}}_i] = \\
&= \int_{\Gamma_i} [\Delta\delta\mathbf{g}_{\mathrm{loc}}]^{\mathrm{T}} \left[\frac{\partial \mathcal{G}_c^i}{\partial \mathbf{g}_{\mathrm{loc}}}\right] \mathrm{d}\Gamma + [\delta\mathbf{g}_{\mathrm{loc}}]^{\mathrm{T}} \left[\frac{\partial^2 \mathcal{G}_c^i}{\partial \mathbf{g}_{\mathrm{loc}}^2}\right] \Delta\mathbf{g}_{\mathrm{loc}} \,\mathrm{d}\Gamma + \\
&+ \int_{\Gamma_i} [\delta\mathbf{g}_{\mathrm{loc}}]^{\mathrm{T}} \left[\frac{\partial^2 \mathcal{G}_c^i}{\partial \mathbf{g}_{\mathrm{loc}} \partial \hat{\mathfrak{d}}_i}\right] \Delta\hat{\mathfrak{d}}_i \,\mathrm{d}\Gamma,
\end{aligned} \tag{3.84}$$

$$\begin{aligned}
&\hat{L}[\mathcal{R}^{\hat{\mathfrak{d}}_i}(\mathbf{u}_i, \hat{\mathfrak{d}}_i, \delta\hat{\mathfrak{d}}_i)] \cdot [\Delta\mathbf{u}_i, \Delta\hat{\mathfrak{d}}_i] = \\
&= \int_{\Gamma_i} \left[\delta\hat{\mathfrak{d}}_i\right]^{\mathrm{T}} \left[\frac{\partial^2 \mathcal{G}_c^i}{\partial \hat{\mathfrak{d}}_i^2}\right] \Delta\hat{\mathfrak{d}}_i \,\mathrm{d}\Gamma + \int_{\Gamma_i} \left[\delta\hat{\mathfrak{d}}_i\right]^{\mathrm{T}} \left[\frac{\partial^2 \mathcal{G}_c^i}{\partial \hat{\mathfrak{d}}_i \partial \mathbf{g}_{\mathrm{loc}}}\right] \Delta\mathbf{u}_i \,\mathrm{d}\Gamma.
\end{aligned} \tag{3.85}$$

The geometrical effects arise from the variation of the rotation operator with respect to the displacement field [100; 101]. The proposed model represents a generalization of the 2D formulation for small displacements in [52] to 3D applications and finite deformations.

In line with the previous derivations, we construct the finite element discretization of the proposed 3D geometrical nonlinear interface model compatible with the phase field approach of fracture in the bulk. As customary, this requires the definition of a reference surface (usually the interface midsurface). The parametric space is defined as $\bar{\boldsymbol{\xi}} = \{\xi^1, \xi^2\} \in$ [-1,1]×[-1,1], where ξ^1, ξ^2 denote the natural coordinates of the interface, and $\mathbf{N}(\bar{\boldsymbol{\xi}})$ identifies the operator arranging the interface shape functions in matrix notation.

Applying standard arguments, the interpolation of the local gap vector can renders:

$$\mathbf{g}_{\mathrm{loc}} = \mathbf{R}(\mathbf{d}_i)\hat{\mathbf{B}}_{\mathbf{b}}\mathbf{d}_i, \tag{3.86}$$

where $\hat{\mathbf{B}}_{\mathbf{b}} = \mathbf{L}\mathbf{N}$ is the interface compatibility operator, and $\mathbf{d}_i$ denotes the vector collecting the nodal displacements of the interface flanks. There-

fore, the discrete variation and increment of the local gap vector are given by:

$$\delta \mathbf{g}_{\text{loc}} = \left[\frac{\partial \mathbf{R}(\mathbf{d}_i)}{\partial \mathbf{d}_i} \hat{\mathbf{B}}_{\mathfrak{b}} \mathbf{d}_i + \mathbf{R}(\mathbf{d}_i) \hat{\mathbf{B}}_{\mathfrak{b}} \right] \delta \mathbf{d}_i;$$
$$\Delta \mathbf{g}_{\text{loc}} = \left[\frac{\partial \mathbf{R}(\mathbf{d}_i)}{\partial \mathbf{d}_i} \hat{\mathbf{B}}_{\mathfrak{b}} \mathbf{d}_i + \mathbf{R}(\mathbf{d}_i) \hat{\mathbf{B}}_{\mathfrak{b}} \right] \Delta \mathbf{d}_i, \tag{3.87}$$

whilst the discrete linearized virtual local gap reads:

$$\Delta \delta \mathbf{g}_{\text{loc}} \approx \left[2 \frac{\partial \mathbf{R}(\mathbf{d}_i)}{\partial \mathbf{d}_i} \hat{\mathbf{B}}_{\mathfrak{b}} \delta \mathbf{d}_i \right] \Delta \mathbf{d}_i \tag{3.88}$$

In an analogous manner, the crack phase field variable, its variation and its increment are interpolated as the interface as follows

$$\mathfrak{d}_i = \hat{\mathbf{B}}_{\mathfrak{d}} \bar{\mathfrak{d}}_i, \quad \delta \mathfrak{d}_i = \hat{\mathbf{B}}_{\mathfrak{d}} \delta \bar{\mathfrak{d}}_i, \quad \Delta \mathfrak{d}_i = \hat{\mathbf{B}}_{\mathfrak{d}} \Delta \bar{\mathfrak{d}}_i \tag{3.89}$$

where $\hat{\mathbf{B}}_{\mathfrak{d}}$ is the compatibility operator corresponding to the crack phase field variable, and $\bar{\mathfrak{d}}_i$ stands for the nodal phase field values at the interface flanks.

Finally, through the insertion the approximations given above into the residual, Eqs.(3.82)-(3.83), and linearized forms, Eqs.(3.84)-(3.85), the following coupled algebraic systems can be obtained:

$$\begin{bmatrix} \mathbf{k}^i_{\mathbf{dd}} & \mathbf{k}^i_{\mathbf{d}\mathfrak{d}} \\ \mathbf{k}^i_{\mathfrak{d}\mathbf{d}} & \mathbf{k}^i_{\mathfrak{d}\mathfrak{d}} \end{bmatrix} \begin{bmatrix} \Delta \mathbf{d}_i \\ \Delta \bar{\mathfrak{d}}_i \end{bmatrix} = \begin{bmatrix} \mathbf{f}^i_d \\ \mathbf{f}^i_{\mathfrak{d}} \end{bmatrix}. \tag{3.90}$$

Note that in line with the bulk formulation, the system given in Eq.(3.90) is solved via a monolithic Newton-Raphson method.

Chapter 4

Fracture simulation in micro-systems

4.1 Elasto-plastic fracture of a busbar

In this section the experiments described in Section 2.1 are simulated. The ductile fracture of the busbar is simulated by means of the numerical coupling between elasto-plastic elements and interface elements. The interface elements are formulated considering the CZM described in Section 3.2. With this approach the competition between plasticity and crack propagation is investigated.

The crack propagation is studied at the micro and macro level. The micro behaviour of the crack is taken into account considering the experimental results described in Section 2.1. The macro behaviour is taken into account by means of the experimental force-displacement curves of the tests. The force-displacement curves give information on the overall behaviour of the specimen.

From a computational point of view, the interface elements are not used to simulate what is commonly called an interface, e.g. the surface which separate two materials. They are introduced to reproduce a cohesive fracture in the bulk. Then, we can control the fracture propagation at the micro level tuning the parameters that govern the traction-separation

law of the interface elements.

4.1.1 Numerical simulations

The first simulation concerns the unnotched tensile test. In this test the behaviour of the specimen is purely elasto-plastic. No interface elements are introduced to simulate that experiment. The mechanical parameters used for the simulation are a Young modulus E = 1314 MPa, a hardening coefficient H = 18.06 MPa and a yield stress σ_y = 3.2 MPa. These values are interpolated with a bilinear fitting of the stress-strain curve of the experimental test. Then, the comparison between the experimental results and simulation predictions is performed in order to validate the computational model. The computational model consists of elasto-plastic 4-node finite elements with a von Mises constitutive law with linear hardening. Fig. 27 shows the good agreement between the experimental results and the simulation predictions.

For the case of notched specimens, the interface elements are introduced along the middle line of the specimen (Fig. 28). The stiffness of the traction-separation law is set very high in order to reduce the artificial compliance introduced with the interface elements. The simulated geometry and the applied boundary conditions are shown in Fig. 28.

Among all the existing CZM laws, two formulations are compared to best fit the experimental results: the two-parameters Tvergaard CZM ([105], Fig. 29(a)), and the three-parameters bilinear CZM with softening ([90], Fig. 29(b)). In the first case, the shape of the CZM is defined by the following equation:

$$\sigma = \begin{cases} \sigma_{\max} \dfrac{g_{\mathrm{n}}}{g_{\mathrm{c}}} \dfrac{27}{4} \left[1 - 2\dfrac{g_{\mathrm{n}}}{g_{\mathrm{c}}} + \left(\dfrac{g_{\mathrm{n}}}{g_{\mathrm{c}}} \right)^2 \right], & \text{if } 0 < \dfrac{g_{\mathrm{n}}}{g_{\mathrm{nc}}} < 1, \\ 0, & \text{if } \dfrac{g_{\mathrm{n}}}{g_{\mathrm{nc}}} \geq 1. \end{cases} \tag{4.1}$$

The shape of the CZM is determined fixing two parameters. The parameters that we select for the control of the shape are the peak stress $\sigma_{\max}$

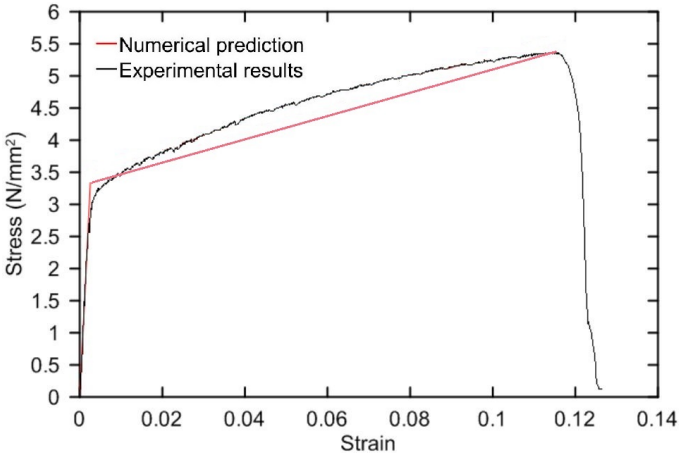

Figure 27: Comparison between the experimental and the numerical stress-strain curve for the case of unnotched specimen.

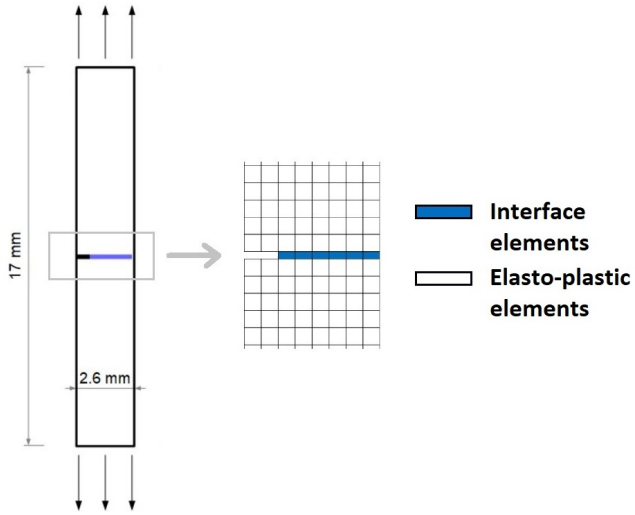

Figure 28: Geometry of the simulated notched specimen. In blue it is highlighted the area where interface elements are introduced.

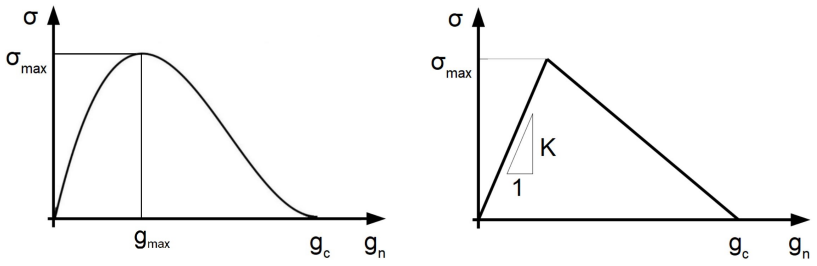

Figure 29: (a) Tvergaard CZM; (b) Bilinear with softening CZM.

and the critical opening at failure g_c. In the second CZM, the shape is defined by the following equation:

$$\sigma = \begin{cases} K g_n, & \text{if } 0 < g_n \leq \dfrac{\sigma_{max}}{K}, \\ \sigma_{max} - \left(g_n - \dfrac{\sigma_{max}}{K}\right) \dfrac{\sigma_{max}}{g_c - \sigma_{max}/K}, & \text{if } \dfrac{\sigma_{max}}{K} < g_n \leq g_c, \\ 0 & \text{if } g_n > g_c. \end{cases} \tag{4.2}$$

In this case, the three parameters that we select for the identification of the shape of the CZM are: the peak stress $\sigma_{\mathbf{max}}$, the initial slope K and the critical opening $g_{\mathbf{c}}$.

The results of the notched simulations in terms of von Mises stress are shown in Fig. 30. These results come from the simulation of the specimen with a notch of 0.45 mm, but the qualitative result is the same for other notch lengths.

The results of the 0.45 mm notch with an imposed displacement of 0.9 mm can be seen in Fig. 30. Here the von Mises stress contour plot is shown for five representative time steps.

4.1.2 Parameter identification procedures

In order to speed up and automatized the identification of the CZM parameters, two optimization procedure are used. These procedures are set

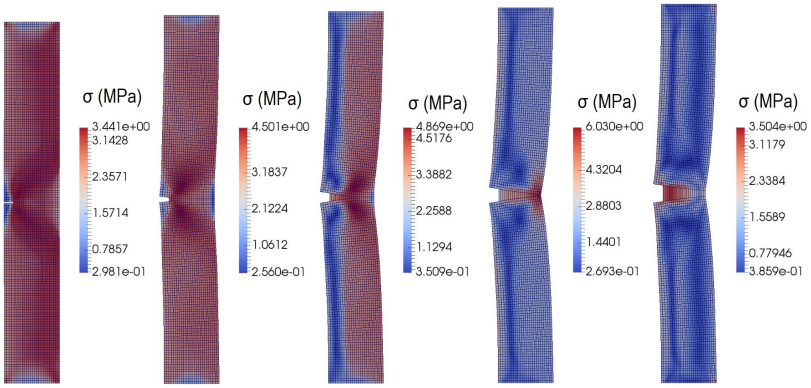

Figure 30: von Mises stress contour plot for the simulation of the 0.45 mm notch experiment. The images refers to following imposed displacements: (a) 0.045 mm; (b) 0.36 mm; (c) 0.54 mm; (d) 0.72 mm; (e) 0.9 mm.

up in collaboration with Dr. Dario Piga from the Dalle Molle Institute for Artificial Intelligence Research (Switzerland).

With these optimization algorithms want to identify the unknown parameters of the CZM. We collect the unknown parameters in the vector $\mathbf{p}$. It reads:

$$\mathbf{p} = [\sigma_{\max}, g_c] \qquad \text{for Tvergard CZM}$$

$$\mathbf{p} = [\sigma_{\max}, g_c, K] \qquad \text{for bilinear CZM}$$

This vector is defined in the vector space $\mathcal{P}$, which contain all the admissible $\mathbf{p}$. We consider that the vector $\mathbf{p}$ is not admissible if the simulation performed with the parameters collected in it generate a result with no physical meaning. Then, $\mathcal{P}$ is constraint according to physical or mathematical restrictions. For each value of $\mathbf{p}$ the so called cost function (or objective function) Φ is computed. Φ is defined as the distance between the experimental and the numerical force-displacement curves. Defining $\Delta\mathbf{F} = \mathbf{F}_{\text{num}} - \mathbf{F}_{\text{exp}}$ as the difference between the numerical and experi-

mental force vectors, the equation of Φ reads:

$$\Phi = \sqrt{\Delta \mathbf{F}^{\mathrm{T}} \mathbf{Q} \Delta \mathbf{F}} \tag{4.3}$$

where $\mathbf{Q}$ is the weight matrix. This matrix is a diagonal matrix which allow to improve the fitting of a specific part of the experimental curve. When $\mathbf{Q}$ is equal to the identity matrix all the points of the force-displacement curve will have the same weight.

The optimization algorithms herein used has been originally developed to solve optimization problems in convex functions. In our case we want to minimize the cost function Φ which is not a convex function. This means that Φ is characterized by many local minimums and the optimization procedure is influenced by the initial tentative value of $\mathbf{p}$. In order to deal with this non convex problem we use and compare the following optimization algorithms: the gradient descent method with backtracking line search [106], and the particle swarm optimization (PSO) algorithm [107].

The gradient descent method is an algorithm which search for the minimum of the cost function following the negative gradient direction. The procedure commences with an initial tentative value of $\mathbf{p}$. At each time step k the numerical gradient of Φ with respect to $\mathbf{p}$ is computed via a central difference approximation. The approximation reads:

$$\nabla \Phi_{\mathrm{i}} = \frac{\partial \Phi}{\partial p_{\mathrm{i}}} \backsimeq \frac{1}{2\Delta p_{\mathrm{i}}} [\Phi(p_{\mathrm{i}} + \Delta p_{\mathrm{i}}) - \Phi(p_{\mathrm{i}} - \Delta p_{\mathrm{i}})] \tag{4.4}$$

where p_{i} is the i-th component of the vector $\mathbf{p}$ and Δp_{i} is a small variation of the i-th component.

The next tentative value $\mathbf{p}_{\mathrm{k+1}}$ is given moving $\mathbf{p}_{\mathrm{k}}$ in the direction of the negative gradient. The length of the displacement $(\mathbf{p}_{\mathrm{k+1}} - \mathbf{p}_{\mathrm{k}})$ is proportional to the variable t. This variable is calculated at each step according to the backtracking line search algorithm. The schematic description of the gradient descent algorithm and the backtracking line search can be found in Algorithms 1 and 2, respectively.

The PSO is an algorithm based on particles which move and explore the cost function values. The particles are located within the domain $\mathcal{P}$.

Algorithm 1: Gradient descent method.

Input: initial value of $\mathbf{p} \in \mathcal{P}$
Output: $\mathbf{p}$ which gives the minimum value of Φ

while error $>$ tolerance **do**

—— **Generic step k** ————————————-
    Numerical gradient: compute $\nabla\Phi_k$ (Eq. (4.4))
    Backtracking line search: found the value of t (Algorithm 2)
    Update: $\mathbf{p}_{k+1} = \mathbf{p}_k - \nabla\Phi_k t_k$
    Error: $\| \nabla\Phi_k \|$

end while

Algorithm 2: Backtracking line search.

Input: $\alpha = 0.5$, $\beta = 0.5$, $t_0 = 1$, $\nabla\Phi_k$
Output: t

$t = t_0$
$\mathbf{p}^{ln} = \mathbf{p}_k$
while $\Phi(\mathbf{p}^{ln}) > \Phi(\mathbf{p}_k) - \alpha \| \nabla\Phi_k \| t$ **do**
    Tentative parameters: $\mathbf{p}^{ln,trial} = \mathbf{p}_k - \nabla\Phi_k t$
    if $\mathbf{p}^{ln,trial} \in \mathcal{P}$ **then**
        Update: $\mathbf{p}^{ln} = \mathbf{p}^{ln,trial}$
        Update: $t = \beta t$
    else
        Update: $t = \beta t$
    end if
end while
$t_k = t$

The coordinates of a particle correspond to the entries of the unknown vector $\mathbf{p}$. The method is initialized defining a number of particles that are randomly located in $\mathcal{P}$. For each particle $\mathbf{p}^{(i)}$ the cost function Φ is computed. Once the value of Φ is known for each particle, the velocity vector

$\mathbf{v}$ and the update position of the particles is computed at the following step (k+1). These computations are based on the following system:

$$\begin{cases} \mathbf{v}_{k+1}^{(i)} = W\mathbf{v}_k^{(i)} + C_1(\mathbf{p}_{opt}^{(i)} - \mathbf{p}_k^{(i)}) + C_2(\mathbf{p}_{\text{global opt}} - \mathbf{p}_k^{(i)}) \\ \mathbf{p}_{k+1}^{(i)} = \mathbf{p}_k^{(i)} + \mathbf{v}_{k+1}^{(i)} \end{cases} \tag{4.5}$$

where W, C_1 and C_2 are known coefficients. $\mathbf{p}_{opt}^{(i)}$ is the local optimum. It gives the best position assumed by a single particle in its history. For best position it is intended the particle position which gives the minimum value of Φ. $\mathbf{p}_{\text{global opt}}$ is the global optimum. It gives the best position assumed in the history of the whole system. Then, the history of all the particles is evaluated. In other words, considering a single particle the velocity terms is the sum of three contributions. The first contribution is an inertial vector proportional to the current velocity of the particle. The second contribution is a vector pointing at the local optimum of the particle. The third contribution is a vector pointing at the global optimum. Then, the particle position is updated by adding to the current position the updated velocity term. A schematic resume of this procedure can be found in Algorithm 3.

In order to validate the optimization procedure herein described we first test the gradient descent method with the simulation of the unnotched specimen. The aim is to validate the algorithm trying to identify the parameters with known optimal values. Then, the Young modulus E, the yield stress σ_y and the hardening coefficient H are perturbed from the optimal values and are given as initial guess of the unknown vector $\mathbf{p}$. This vector and the domain in which is defined reads:

$$\mathbf{p} = [E, \sigma_y, H]$$

$$\mathcal{P} = \{E, \quad \sigma_y, \quad H \mid E > 0, \quad \sigma_y > 0, \quad H > 0\}$$

We consider as optimal values of these parameters the values found with the bilinear interpolation of the experimental stress-strain curve (Section 4.1.1). Table 1 shows the optimal and the perturbed values of $\mathbf{p}$.

Algorithm 3: Particle swarm optimization algorithm.

Input: Number of particles N, limits of the domain $\mathcal{P}$, coefficients W, C_1 and C_2

Output: $\mathbf{p}$ which gives the minimum value of Φ

—— **Initialization** ——————————

Spread the particles randomly along the domain $\mathcal{P}$
for all $i = 1 : N$ **do**
    Compute the cost $\Phi(\mathbf{p}^{(i)})$
    Define the local optimum $\mathbf{p}^{(i)}_{opt} = \mathbf{p}^{(i)}$
end for
Define the global optimum: $\mathbf{p}_{\text{global opt}}$

—— **Generic step k** ——————————-

for all $i = 1 : N$ **do**
    Compute the velocity $\mathbf{v}^{(i)}_{k+1}$
    Update the particle position $\mathbf{p}^{(i)}_{k+1}$
    if $\mathbf{p}^{(i)}_{k+1} \in \mathcal{P}$ **then**
        Compute the cost $\Phi(\mathbf{p}^{(i)}_{k+1})$
    else
        Relocate randomly $\mathbf{p}^{(i)}_{k+1}$ in $\mathcal{P}$
        Compute the cost $\Phi(\mathbf{p}^{(i)}_{k+1})$
    end if
    Check if $\mathbf{p}^{(i)}_{opt}$ and $\mathbf{p}^{(i)}_{\text{global opt}}$ need to be updated
end for

The procedure reaches a minimum close to the optimal value in 110 steps. The overall computational time was around 40 minutes. The cost function is calculated with and without the weight matrix $\mathbf{Q}$. The weight matrix is employed in order to improve the interpolation of the linear part. The results of the gradient descent method, with and without weight matrix, are shown in Fig. 31. These results are confirmed by other sets of perturbed parameters. However, for some sets the algorithm does not found a value close to the optimal one. This demonstrate that the cost

$\mathbf{p}$	Optimal values	Perturbed values	Gradient method results	Initial variation	Final variation
E	1314 MPa	1000 MPa	1367 MPa	-24%	+4%
σ_y	3.55 MPa	2.5 MPa	4.05 MPa	-30%	+14%
H	18.06 MPa	100 MPa	17.70 MPa	+450 %	-2%

Table 1: Parameters used for the validation of the gradient descent method.

function is not convex and the algorithm reach a local minimum far from the global minimum.

After this first validation, the gradient descent algorithm is used for the identification of the two parameters of the Tvergaard CZM (Eq. (4.1)). The 0.45 mm notched specimen is simulated considering the unknown vector and its domain equal to:

$$\mathbf{p} = [\sigma_{\max}, \quad g_c]$$

$$\mathcal{P} = \{\sigma_{\max}, \quad g_c \mid \sigma_{\max} > 0, \quad g_c > g_{\max}\}$$

Unfortunately, the gradient descent method proves to be not very suitable for this identification problem. In fact, due to the not convexity of the cost function, many local minimum are found. This lead to two main drawbacks: the solution found with the algorithm stays in the neighbourhood of the initial guess of $\mathbf{p}$; the algorithm is very slow. The first drawback is caused by the fact that two local minimums are probably separated by a local maximum. Then, considering the path drawn over Φ by the various guess of $\mathbf{p}$, this path cannot cross the region of a local maximum. This aspect is ascribed to the fact that the new guess of $\mathbf{p}$ follows the descent direction. Consequently, in presence of a function with numerous local minimums, the algorithm find a solution close to the initial guess. The second drawback is caused by the fact that the algorithm become very slow when it is approaching a local minimum. In fact, in those regions the gradient have small values, consequently the new guess of $\mathbf{p}$ will be also very small. This can be seen from line 4 of the Algorithm 1, which shows that the distance $(\mathbf{p}_{k+1} - \mathbf{p}_k)$ is proportional to the gradient.

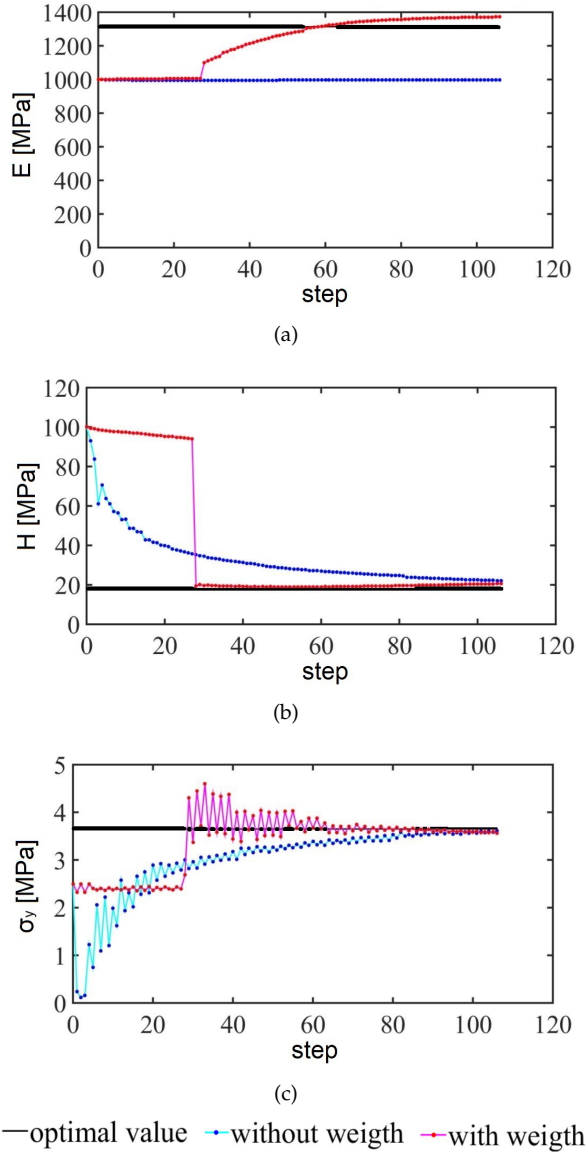

Figure 31: Variation of the guess of the unknown during the gradient method validation: (a) variation of E; (b) variation of H; (b) variation of $\sigma_{\max}$.

Due to the discouraging results obtained with the gradient descent method we use the PSO algorithm. We first perform the optimization procedure for the 0.45 mm notch simulation with Tvergaard CZM. The domain to look for the solution is:

$$\mathcal{P} = \{\sigma_{\max}, \quad g_c \mid 3\ \text{MPa} < \sigma_{\max} < 15\ \text{MPa}\,, 0.01\ \text{mm} < g_c < 0.5\ \text{mm}\}$$

The procedure found the optimal values of $\sigma_{\max} = 8.60$ MPa and $g_c = 0.19$ mm after 30 steps. This values fit with a satisfactory accuracy the force displacement curve of the 0.45 mm notch experimental test (Fig. 32 (a)). The same satisfactory accuracy is not found for the case of the 0.80 mm notch experimental test (Fig. 32 (b)).

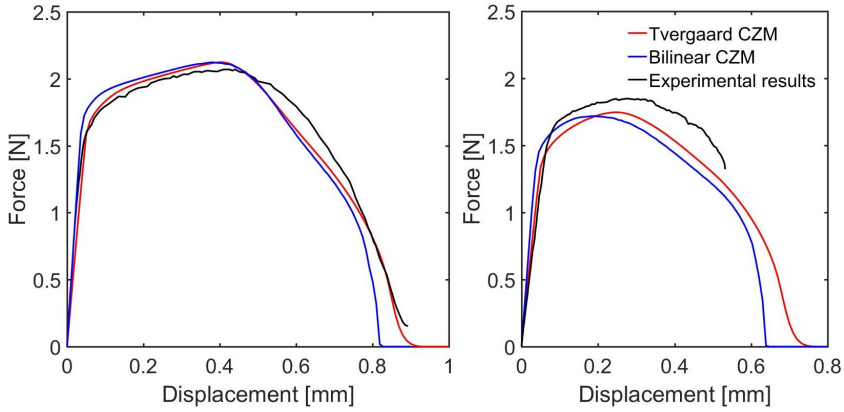

(a) (b)

Figure 32: Comparison of the experimental curves and numerical curves of the simulations with Tvergaard CZM. (a) 0.45 mm notch; (b) 0.80 mm notch.

In order to overcome this limitation we perform the same simulations using the bilinear three-parameters CZM (Eq. (4.2)). With this CZM we can control the softening part of the curve varying the ratio $\sigma_{\max}/K$. Then, the CZM change its behaviour from brittle to ductile changing the

independent parameters. With this bilinear model we perform the optimization procedure for the case of 0.45 mm notch. The identified parameters are then verified with the simulation of the 0.8 mm notch. For this optimization procedure the domain considered is:

$$\begin{aligned}\mathcal{P} =\{&\sigma_{\max}, \quad g_c, \quad K \mid \\ &8 \text{ MPa } < \sigma_{\max} < 20 \text{ MPa }, 0.001 \text{ mm } < g_c < 0.1 \text{ mm }, \\ &10^3 \text{MPa/mm } < K < 10^4 \text{ MPa/mm }, K \geqslant \sigma_{\max}/g_c\}\end{aligned}$$

The condition $K \geqslant \sigma_{\max}/g_c$ is added to avoid the not physically shape of the CZM where the crack opening corresponding to the peak stress is bigger than the critical opening g_c.

We use 30 particles to find the optimal values. The procedure took 17 steps to find the following optimal values: $\sigma_{\max} = 13.3$ MPa, $g_c = 0.07$ mm, $K = 6610$ MPa/mm. In Figs. 33 and 34 the dynamic of the particles during the optimization procedure is shown. The circles represent the particle positions and its radius is proportional to the particle cost value Φ. For each particle the velocity vector is also displayed as a black vector. The red filled circle represent the current global optimum. In this figures three representative steps are shown in order to resume the evolution of the algorithm. In Fig. 35(a) the three steps are represented all together. This figure evidence the attraction of the particle to the global optimum. Moreover, it is shown the strength of the algorithm in exploring the values of the cost function in the surroundings of the current global optimum. Then, as it is shown in Fig. 35(b), the global optimum is constantly improved.

The optimal parameters found with this last procedure give the fitting shown in Fig. 32. Even though the bilinear CZM is governed by three parameters, the fitting that provides is less accurate than the Tvergaard CZM. In fact, the fitting of the softening part of the 0.45 mm notch curve is underestimated. On the contrary, the fitting of the 0.8 mm notch is more accurate than the Tvergaard CZM. The failure displacement of this curve is overestimated of around a 20 %, which is a better result than

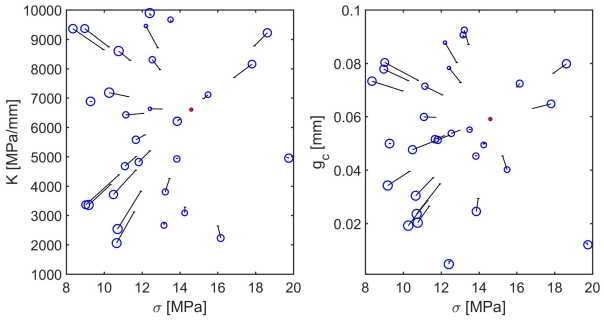

(a)

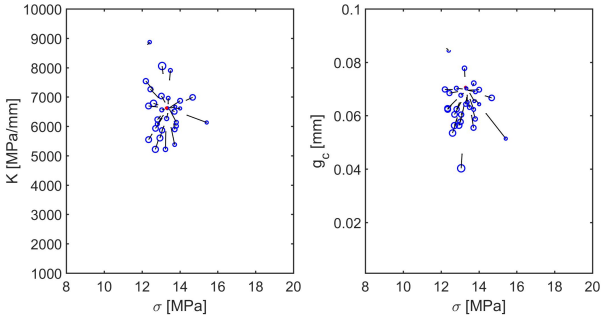

(b)

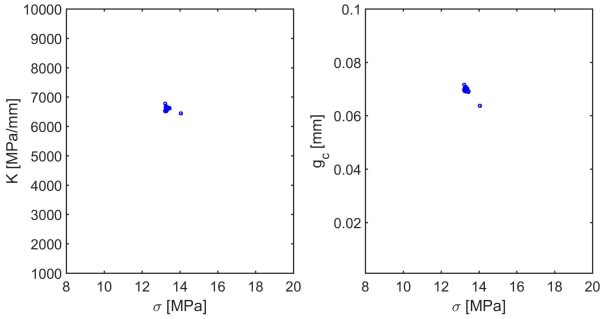

(c)

Figure 33: 2D representation of the PSO evolution. (a) step 0 (initial configuration); (b) step 6; (c) step 17.

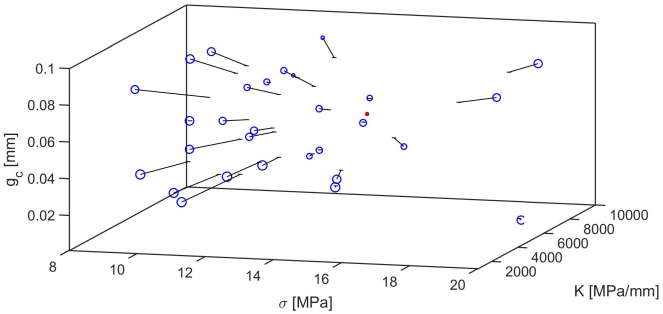

(a)

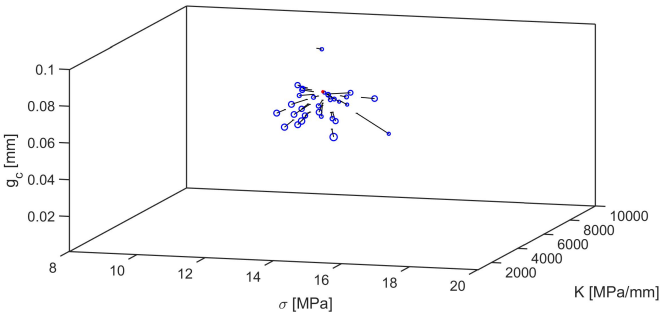

(b)

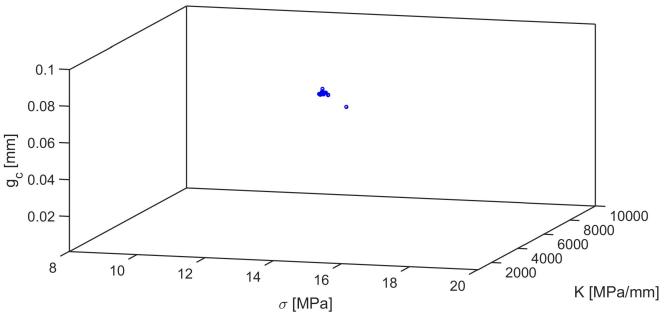

(c)

Figure 34: 2D representation of the PSO evolution. (a) step 0 (initial configuration); (b) step 6; (c) step 17.

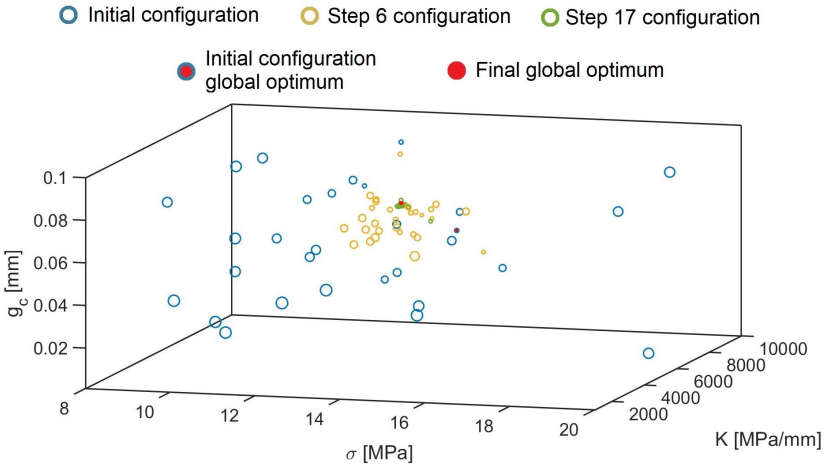

(a)

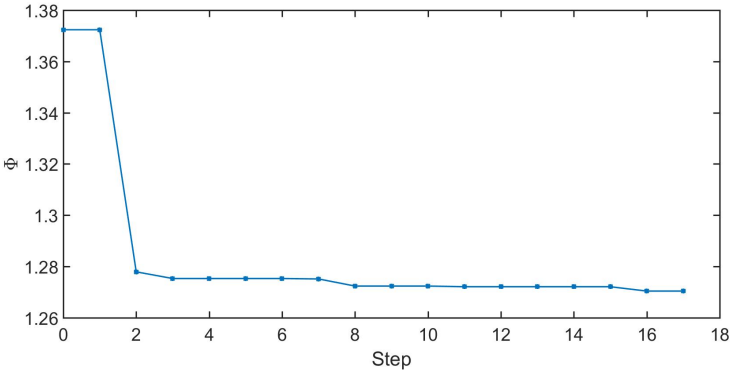

(b)

Figure 35: Summary of the PSO evolution. (a) 3D evolution of three representative steps of the algorithm. (b) evolution of the cost function Φ during the PSO procedure.

the 30 % of the Tvergaard model. Another important point regards the different optimal parameters found with the two models. The value of the critical opening g_c found in the bilinear model is more acceptable from a physical point of view. In fact, recalling the experimental results described in Section 2.1, from the SEM images it is clear that the critical opening should be of the order of few microns. Then the value found for the bilinear model is more acceptable.

4.2 Fracture phenomena at the micro scale: the case of the adhesive wear

Adhesive wear is one of the various forms of wear of materials [108] and its evolution is not yet fully understood. It is mostly induced by severe adhesion between asperities of rough surfaces in contact. It has its roots at the micro-scale and it occurs under special environmental conditions [109]. Its clear observation is possible only in high vacuum, where there is no gas between the two surfaces in contact, and in absence impurities like oxide films. In spite of the need for such particular conditions, adhesive wear can occur frequently in mechanical system components in the case of insufficient lubrication. For instance, this is the case of plane bearings or gear teeth that are particularly affected by strong adhesive wear.

Adhesive wear can occur not only in metals, but also in ceramics and polymers. Materials with comparable hardness are more prone to adhesive wear [110] and metals can develop the most severe form of adhesive wear. It is theorized [111] that when two metallic surfaces are sufficiently close to each other to consider them in contact (i.e. for a distance less than 1 nm), electrons can be exchanged between the two opposing surfaces. This free movement of the electrons provides the explanation for the local bonds causing adhesive wear.

In the literature, the study of adhesive wear is mostly based on two well-known pioneering approaches: the atomistic model by Holm [112] and the continuum fracture model by Archard [113]. Holm's model assumes that adhesive wear can be interpreted as a phenomenon of atoms

removal from the asperities in contact. Consequently, the asperities undergo a process of progressive flattening. This model is supported by experiments conducted with the atomic force microscope [114; 115] and by molecular dynamics simulations [116; 117]. This approach can hardly predict the occurrence of steady state wear observed in many tribological systems [118], due to a progressive flattening of the surfaces which usually continues without reaching an asymptotic geometrical configuration.

On the other hand, Archard's model assumes that adhesive wear is the result of debris originated by asperity interlocking and fracture. This hypothesis is largely confirmed by many experimental tests [119; 120; 121; 122]. When two joint asperities are subjected to sliding motion, the asperities experience a strong deformation which causes severe plastic strain in ductile materials (Fig. 36 (a)). After that stage, cracks nucleate under shear (Fig. 36 (b)) until the fractured material leads to debris formation.

Most of the studies in the literature on adhesive wear are focused on the estimation of the debris volume (wear volume) [120], to estimate the material loss. In the present study, we focus on the simulation and understanding of the fracture stage which leads to debris formation. Using the phase field (PF) approach to fracture, whose features are described in Section 3.1.1, the nucleation of cracks at joined asperities is investigated, along with the crack path from their propagation. Considering a parametric study with different model asperity geometries, the conditions for the occurrence of a steady state wear are carefully analysed and identified. The condition of steady state wear is identified when the geometrical features of the undeformed rough profile are re-generated after wear debris formation.

The following sections are organized as follow: in Section 4.2.1 a parametric analysis is performed used the PF method; in Section 4.2.2 the results of the parametric analysis are interpreted studying the effect of the singularities in the simulated geometry; Finally, in Section 4.2.3 it is shown the possibility of a steady-state wear phenomenon.

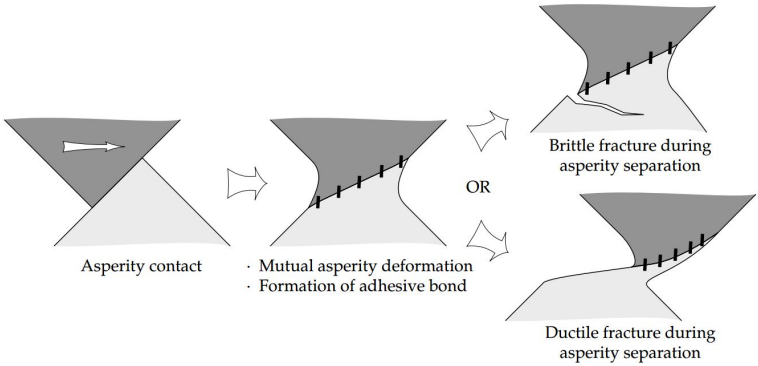

(a)

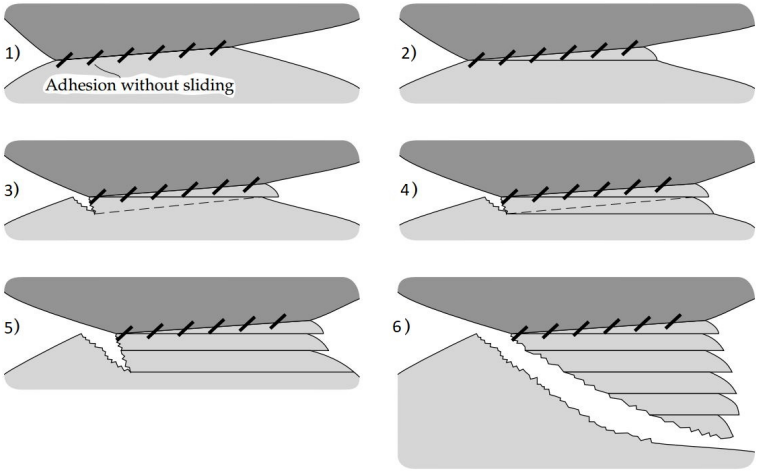

(b)

Figure 36: (a) Deformation of the asperities before fracture; (b) shearing mechanism of fracture of the asperities. With permission from [109]

4.2.1 Design of the numerical experiments

The geometry of rough profiles in contact has been herein simplified by considering triangular asperities with a periodic distribution along the profile, inspired by the model asperity study in [120]. Each asperity has

one side in contact with another, as it is shown in Fig. 37 (a). Taking advantage of periodicity, only the representative unit asperity junction is investigated (Fig. 37 (b)), with periodic boundary conditions imposed on each vertical side of the unit asperity junction. This configuration generates a geometry characterized by 6 re-entrant corners (Fig. 37 (c)) which are potential source of stress singularities and crack nucleation. Four re-entrant corners have a wedge angle 2β, while the remaining two have an angle 2γ. The condition of adhesion between the two asperities is modelled by considering the two asperities as a monolithic solid, in line with theoretical arguments for complete contact problems [123; 124; 125]. The sliding motion of the asperities is simulated by imposing a horizontal displacement on the top and on the bottom of the unit asperity junction, see Fig. 37 (b).

Values of the geometrical parameters		
γ	15; 30; 45; 60; 75	Asperity angle
L	1.0 ; 1.5 ; 2.0	Asperity lateral size (mm)
l_c	0.1 L ; 0.2 L ; 0.3 L ; 0.4 L	Horizontal projection of the junction area
Mechanical parameters		
E	117,000 MPa	Young modulus
v	0.35	Poisson ratio
G	70 N/mm	Fracture energy
l	0.2 mm	Phase Filed internal length scale

Table 2: Geometry and material parameters used in the simulation.

Although the present mechanical problem is nonlinear, we know from [97] that the critical stress corresponding to crack propagation in the PF approach is ruled by a scaling of the type $T_{\mathrm{c}} \sim \sqrt{EG_{\mathrm{c}}/l}$. Therefore, the apparent tangential stress at the onset of debris formation, T_{c}/L, where T_{c} is the critical tangential force per unit out-of-plane thickness for crack nucleation is expected to scale linearly with respect to $\sqrt{EG_{\mathrm{c}}/l}$. Hence, dimensional analysis suggest that:

$$T_c^* = \frac{T_{\mathrm{c}}}{L\sqrt{\dfrac{EG_{\mathrm{c}}}{l}}} = \Phi\left(\frac{l_{\mathrm{c}}}{L}, \gamma\right), \tag{4.6}$$

that is, that the dimensionless critical tangential force is solely function

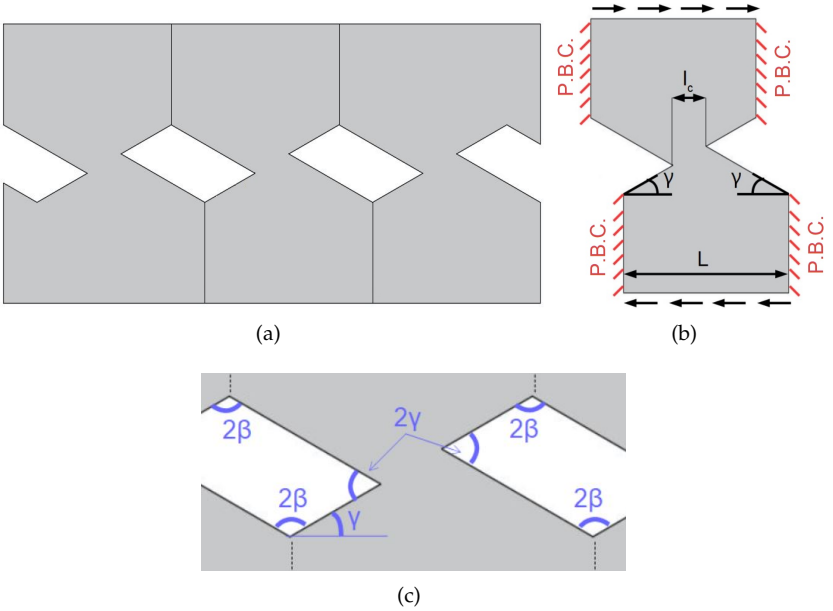

Figure 37: Geometry of the computational model: (a) contact between periodically distributed asperities; (b) the unit asperity junction and the boundary conditions (dashes denote periodic boundary conditions while arrows denote imposed displacements); (c) the re-entrant corners present in the geometry.

of l_c/L and γ.

Hence, the parametric analysis is carried out varying three geometrical parameters: the asperity slope angle γ, the asperity size L, which is also the distance between two adjacent asperities, and the horizontal projection of the junction area l_c (Fig. 37 (b)). The values selected for the parameters are collected in Table 2. This led to a total of 60 simulations, each one with around 57000 nodes. The choice of vary L in addition to l_c/L and γ is due to confirm dimensional analysis results suggesting an independence of L of the critical condition at crack nucleation. Fig. 39 shows the variation of T_c^* vs. the parameter L for each simulation. This plots show clearly that the dependence of the crack onset on the param-

eter L is almost negligible.

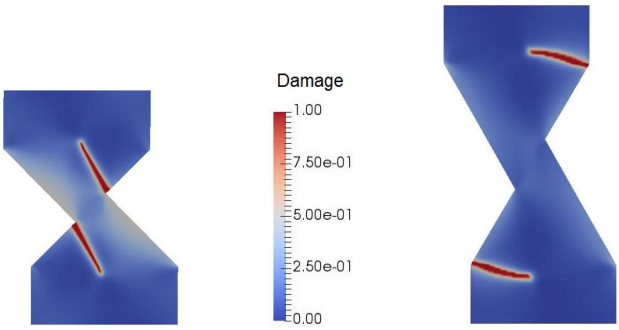

(a) Failure mode 1 (b) Failure mode 2

Figure 38: Different fracture modes: (a) fracture mode 1 generated by the parameters $\gamma = 45°, L = 1.5, l_c = 0.4L/2$; (b) fracture mode 2 generated by the parameters $\gamma = 60°, L = 1.5, l_c = 0.4L/2$; (c) fracture case 3 generated by the parameters $\gamma = 75°, L = 1, l_c = 0.2L/2$.

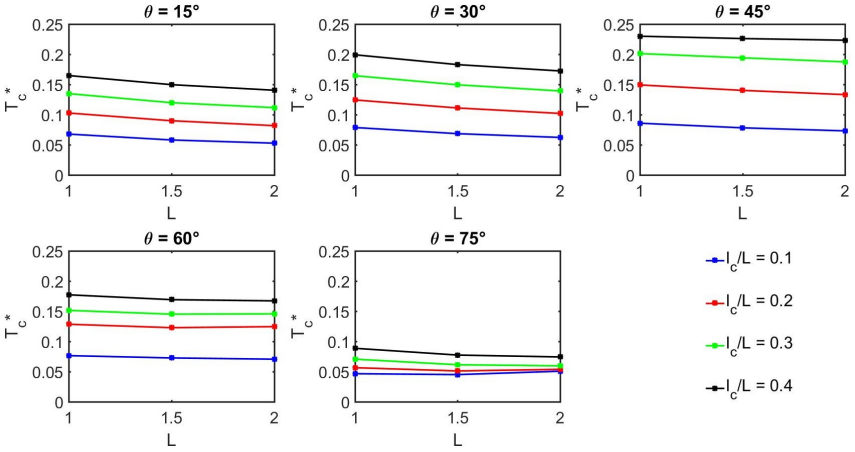

Figure 39: Variation of T_c^* vs L for each combination of model parameter.

l_c/L	$\gamma = 15°$			$\gamma = 30°$			$\gamma = 45°$		
	L			L			L		
	1.0	1.5	2.0	1.0	1.5	2.0	1.0	1.5	2.0
0.1	1	1	1	1	1	1	1	1	1
0.2	1	1	1	1	1	1	1	1	1
0.3	1	1	1	1	1	1	1	1	1
0.4	1	1	1	1	1	1	1	1	1

$\gamma = 60°$			$\gamma = 75°$		
L			L		
1.0	1.5	2.0	1.0	1.5	2.0
1	1	1	2	2	2
2	2	2	2	2	2
2	2	2	2	2	2
2	2	2	2	2	2

Table 3: Crack nucleation (1, 2 based on Fig. 38) for each combination of model parameter.

4.2.2 Discussion of numerical results and mechanical interpretation

The simulations show crack nucleation always in the proximity of a re-entrant corner. We can distinguish among two failure modes: (1) crack propagating from the re-entrant corners of amplitude 2γ (Fig. 38 (a)); (2) crack propagating from the re-entrant corners of amplitude 2β (Fig. 38 (b)). Table 3 shows which failure mode occurs for each combination of model parameters.

To propose a mechanical interpretation of the numerical results, it is remarkable to notice that the problem geometry presents 6 re-entrant corners (Fig. 37 (c)): 4 of amplitude 2β at the base of each asperity, and 2 of amplitude 2γ due to the junction of asperities. Angles γ and β are 90° complementary angles, i.e. $\beta + \gamma = \Pi/2$. Depending on the amplitude of the re-entrant corners, a stress singularity may occur and it can be responsible for the failure modes shown in Fig. 38.

To better understand, the stress-field components σ_{ij} near the crack tip for a radial distance $r \longrightarrow 0$ are given by the Williams [126] asymptotic analysis and are singular for $r = 0$, i.e.:

$$\sigma = r^{\lambda-1} f(\theta), \tag{4.7}$$

where r and θ are, respectively, the radial distance from the notch root and the angle measured from a horizontal axis emanating fro the notch tip (Fig. 40(a)), i and j are the indices of the stress tensor, λ is the eigenvalue characterizing the power of the stress singularity and f is the corresponding eigenfunction [127; 128]. For the present problem, the eigenvalues for Mode I and Mode II deformation, associated to notch opening or sliding, can be determinate from the roots of the following eigenequation:

$$\sin(2\lambda\alpha) \pm \lambda \sin(2\alpha) = 0, \tag{4.8}$$

where α is the angle shown in Fig. 4.40(a). The positive sign in Eq.(4.8) gives the roots corresponding to Mode I deformation (symmetric loading w.r.t. the angle bisector), while the negative value gives the roots corresponding to Mode II deformation (antisymmetric loading). The solution Eq.(4.8) can be found in [129], and the eigenvalue λ is shown in Fig. 40(b) vs. α in the range $\Pi/2 \leq \alpha \leq \Pi$, or vs. β and γ in the range $0 \leq \beta, \gamma \leq \Pi/2$.

As per Eq.(4.7) the stress singularities exist only for $\lambda < 1$. Consequently, considering the re-entrant corner angles in our numerical simulations, we can state that: the stress field associated to Mode I deformation is always singular; the stress field associated to Mode II deformation is singular if $\alpha > 129°$ (e.g. γ and $\beta < 51°$). The value of λ for the angles γ and β are collected in Table 4. Those leading to singular stress field components are highlighted. It can be noticed that the developed failure mode can be predict from the corner amplitude. In fact, the crack onset develop from the corner which generate a singular stress field in Mode II ($\alpha > 129°$). There exist some exception to this rule. For instance for the case of $\gamma = 60°$ and $l_c = 0.2L/2$ the corner whose generate a singular stress field in Mode II is the one at the bottom of the asperity. Consequently, a failure Mode 2 is expected but the simulations predict a failure mode 1.

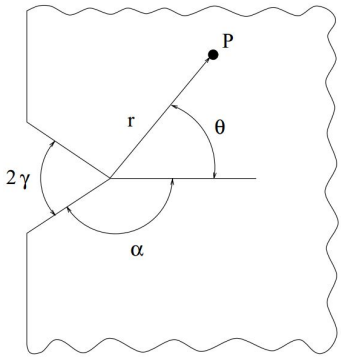

(a)

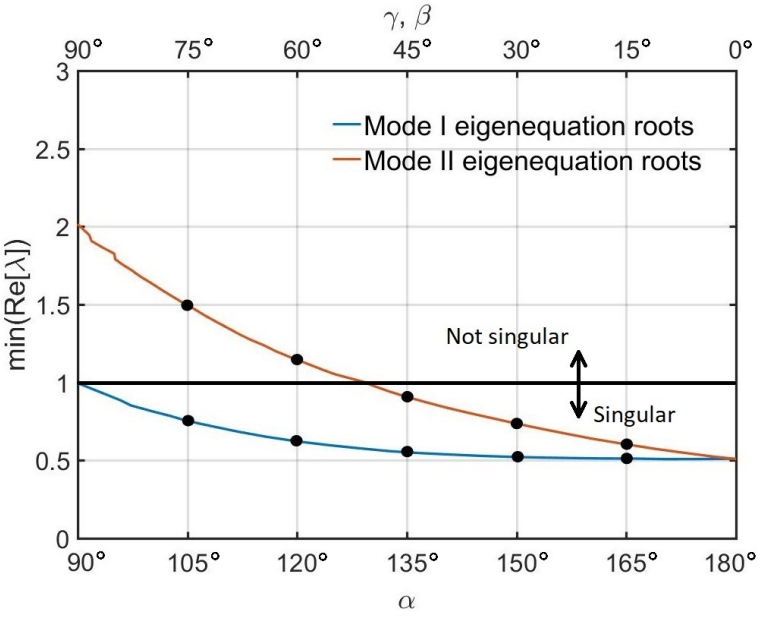

(b)

Figure 40: (a) Re-entrant corner geometry and polar coordinates; (b) eigenvalue λ vs. α, γ and β.

In order to understand these results we have to consider the mutual influence that the corners of amplitude 2α exert over each other. When these corners are close to each other, their mutual influence amplifies the stress singularity. In fact, all the exceptions observed are developed when $l_c = 0.2L/2$, that is when the two corners of amplitude 2α are closer.

Mode II stress singularity				Crack onset	
γ	λ_γ	β	λ_β	Failure mode 1	Failure mode 2
15°	0.61	75°	1.50	X	
30°	0.74	60°	1.15	X	
45°	0.91	45°	0.91	X	
60°	1.15	30°	0.74	X	X
75°	1.50	15°	0.61		X

Table 4: Mode II eigenvalues for each simulated re-entrant corner; In blue the eigenvalues which give a singular stress field are highlighted.

4.2.3 Occurrence of steady-state wear

In this section we investigate the conditions leading to steady-state wear in our model junction problem. Steady state adhesive wear is likely to happen when the new profile created by fracture has the same geometry as that of the undeformed original one. Consequently, the invariance in the profile slope will produce exactly the same crack pattern and therefore the same debris size during further tangential contact. In order to investigate on this phenomenon, the variation of the angle γ after fracture is compared to the original one, defining the value $\Delta\gamma = \gamma' - \gamma$. This value is plotted vs. l_c/L in Fig. 41. The angle γ' of the new asperity is numerically estimated from the crack propagation angle.

The plot confirm the results in Section 4.2.1: the variation of $\Delta\gamma$ is mostly governed by the slope asperity angle γ; the contact horizontal projection l_c has a small influence while the half lateral length influence can be neglected. Fig. 42 shows the crack patterns of the simulation which closer reproduce the steady state wear phenomenon.

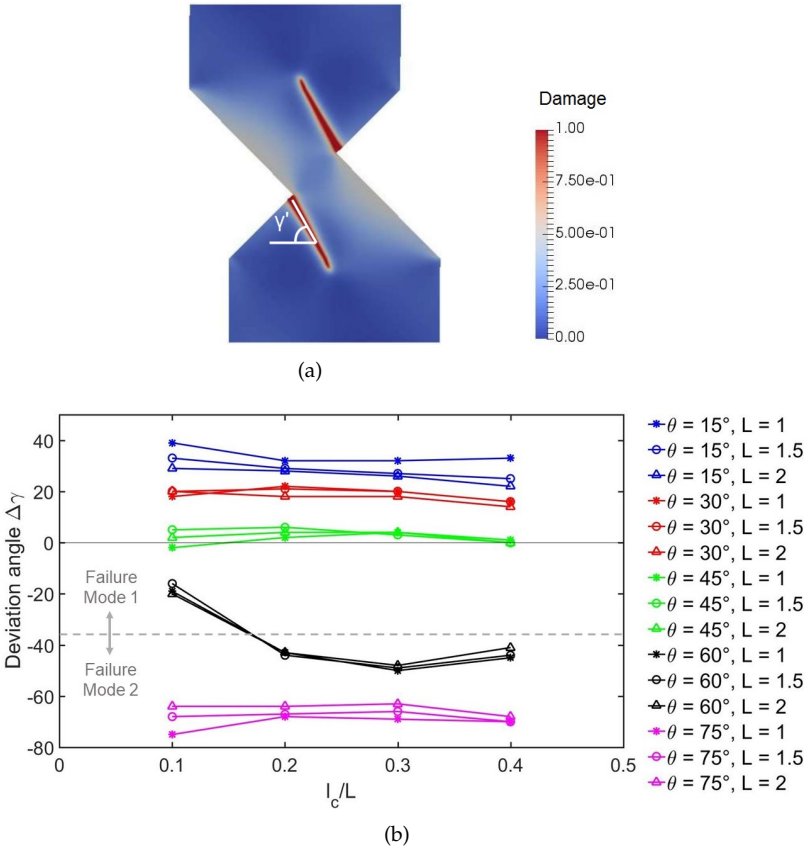

Figure 41: (a) Crack propagation angle γ'; (b) Deviation angle vs normalized contact area for all the simulations of the parametric analysis

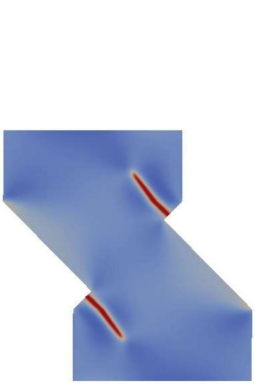

(a) $\gamma = 45°$, $L = 1.0$, $l_c = 0.8L/2$

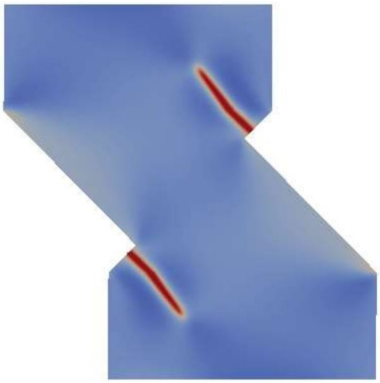

(b) $\gamma = 45°$, $L = 1.5$, $l_c = 0.8L/2$

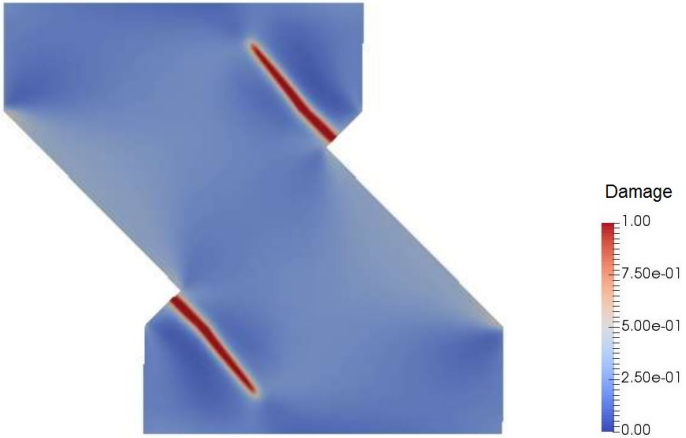

(c) $\gamma = 45°$, $L = 2.0$, $l_c = 0.8L/2$

Figure 42: Configuration which are most likely to develop steady-state wear.

Chapter 5

Fracture simulation in laminates

The prediction of the crack path in composite materials is a very challenging task due to their inherent heterogeneous character. Various factor such as the different mechanical properties of the constituent materials or the delamination of the interfaces[99; 130], make the crack propagating along complex and tortuous paths. The first approach to simulate such complex scenario can be found in [97]. In this study the interaction between an interface and the crack propagation has been investigated. The novelty of the method is the innovative modelling framework within the context of the PF method of fracture and the CZM. In particular, the characteristic length of the two approaches have been rigorously analysed in order to understand the interaction between the crack propagation and the delamination of the interfaces. This numerical framework has been herein employed as fundamental modelling tool for the fracture analysis of crack patterns in composite laminates.

In this regard, for instance, a notched specimen subjected to uniform tensile loading and with the presence of an interface (Fig. 43 (a)) was set up as representative case for the subsequent investigation. In this system the functional of the reaction forces can be stated as follow:

$$F = F\left(\sigma_c, \mathcal{G}_c^b, \mathcal{G}_c^i, E, \nu, l, L, \Delta\right). \tag{5.1}$$

where σ_c is the peak traction of the interface, E and ν are, respectively, the Young modulus and Poisson ratio of the bulk, l is the internal PF length, L is the sample size and Δ is the imposed traction displacement. The functional is manipulated using the Π-theorem of the dimensional analysis [131]. Considering σ_c and L as the physical independent quantities it follows:

$$\frac{F}{\sigma_c L^2} = \Phi\left(\frac{\mathcal{G}_c^b}{\mathcal{G}_c^i}, \frac{\mathcal{G}_c^i E}{\sigma_c^2 L}, \nu, \frac{l}{L}, \frac{\Delta}{L}\right) = \Phi\left(\Pi_1, \Pi_2, \nu, \frac{l}{L}, \frac{\Delta}{L}\right) \tag{5.2}$$

With this manipulation we can define two dimensionless number: $\Pi_1 = \mathcal{G}_c^b/\mathcal{G}_c^i$ and $\Pi_2 = (\mathcal{G}_c^i E)/(\sigma_c^2 L)$. Π_2 rules the size-scale effect given by the cohesive interface, in fact it is proportional to the ratio l_{CZM}/L [97]. When $\Pi_2 \longrightarrow 0$ the interface is very brittle and LEFM is recovered, in this case the dimensionless number Π_1 rule the crack penetration vs deflection competition as shown in Fig. 43 (b). On the contrary, as Π_2 increases, more relevant cohesive phenomena at the interface are present, setting a competition between these two parameters which rules the mechanical system.

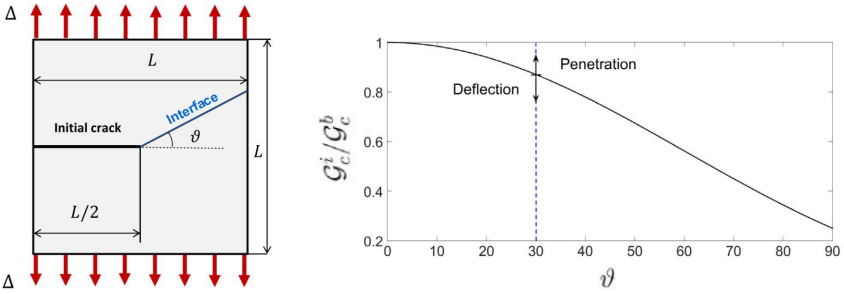

Figure 43: (a) geometry considered to study the effect of a crack impinging on an interface; (b) curve which separate the crack penetration and deflection cases for different impinging angles. With permission from [97]

The behaviour changes when we have a bi-material system Fig. 44(a). In this case for the prediction of crack penetration/deflection we have to consider the Dundurs' parameters defined as:

$$\alpha = \frac{\mu_1(1-\nu_2) - \mu_2(1-\nu_1)}{\mu_1(1-\nu_2) + \mu_2(1-\nu_1)}, \tag{5.3a}$$

$$\beta = \frac{\mu_1(1-2\nu_2) - \mu_2(1-2\nu_1)}{\mu_1(1-\nu_2) + \mu_2(1-\nu_1)}, \tag{5.3b}$$

where μ_i, ν_i $(i = 1, 2)$ denote the Lamé constant and the Poisson ratio of the two materials under consideration. In this case according to the value of $1/\Pi_1$ three different crack patterns can be developed when the crack imping on the interface: crack penetration for very large value of $1/\Pi_1$; single deflection for greater values of $1/\Pi_1$; double deflection when $1/\Pi_1$ takes a small value. For the case of $\beta = 0$ and $\Pi_2 \longrightarrow 0$ the three crack patterns can be predict from the diagram in Fig. 44(b).

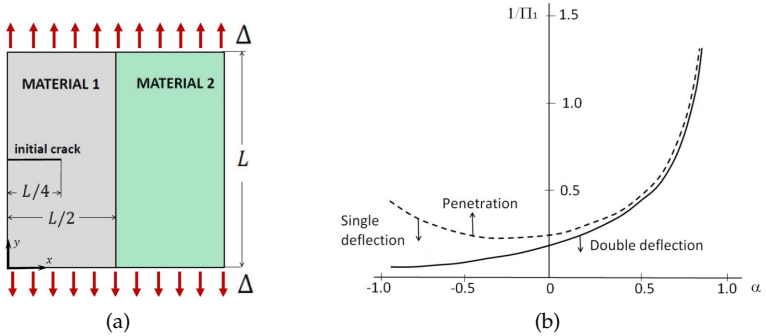

Figure 44: (a) geometry of the tensile test of a bi-material system; (b) curve which separate the crack penetration, crack single deflection and crack double deflection cases. With permission from [97].

The numerical simulation of these phenomena has been performed in [97]. Making use of the computational model formulated by the cited authors, which is described in Chapter 3, the crack propagation in laminates materials is studied. Laminates materials are made of one or two

materials. Adjacent layers are separated by an interface. Consequently, laminates are influenced by all the parameters introduced in the Eqs. (5.2) and (5.3). Unfortunately, a relation to predict crack penetration/deflection does not exist. Numerical simulation can then shade light on the prediction of cracks and failure of laminates.

The simulations presented in the following sections have been performed with the Finite Element Analysis Program FEAP [10].

5.1 2D applications

The laminates selected for the 2D application of the model described in Chapter 3 are the ones designed to increase the toughness of ceramic materials. Ceramic materials are largely used in technological applications, especially with the aim of achieving a desired resistance level to severe wear or corrosive phenomena at high temperatures. However, the main drawback of ceramics regards their brittleness. In order to increase their low toughness, laminates are often used, alternating ceramic and metallic layers. For instance, in [63; 64], Al/SiC and Al/TiN laminates have been tested. The metallic layers make the composite able to withstand higher deformations by means of the development of plasticity at several locations within the specimen, and therefore increasing the overall toughness of the laminate. The same toughening process has been achieved by alternating ceramic layers with polymeric layers in [132]. The main drawback of these solutions is that metals and polymers loose their mechanical properties at high temperatures and have a low wear resistance. A possible way to enhance the toughness of ceramics is to introduce brittle interfaces [133; 134]. Then, ceramics layers are alternated with thin layers of a very brittle ceramic. Such a very brittle layer acts as a brittle interface which make the crack path very complex, thus increasing toughness by acting on the crack tortuosity. This mechanism has been firstly theorized in [135] in the so called Cook-Gordon mechanism. It is the result of crack branching and crack deflection typical of the interaction between crack penetration in the layers and delamination along the existing interfaces. Another approach to foster complex crack

paths is to introduce porous layers between the ceramic ones [136]. However, the drawback of porous materials is their low wear resistance. An alternative approach for the toughening of ceramics is to introduce tough interfaces among the layers with preexisting defects [137]. The tough interface can be made of a ceramic material which guarantees the resistance to wear and corrosion, also at high temperatures. The defects present in the tough interfaces, guarantee the development of crack deflection with a consequent toughening of the ceramic material.

Considering the technological strategies herein described, the introduction of an interface with tailored properties is a strategy to create a complex crack and consequently enhance the toughness of ceramics. This phenomena is studied in the following sections by means of numerical simulations. Moreover, the results of the toughening strategy which make use of layers of a ductile material is also studied. This comprehend the study of the Al/SiC nanolaminate described in Section 2.2.

5.1.1 Crack propagation in bi-material laminates

In this section we study the effect of the interface toughness on the resulting crack path. The case of a single-edge notched bi-material laminate under tension (Fig. 45) is considered. The laminate has been modelled using the PF elements for the bulk and the interface elements compatible with the PF between each layer. The materials which compose the laminate are: a soft material 1 with high fracture toughness; a stiff material 2 with low fracture toughness. The material parameters are collected in Table 5.

Three cases have been examined: (1) laminate with perfectly bonded interfaces; (2) laminate with tough interfaces; (3) laminate with brittle interfaces.

In the first simulation, no interface elements are introduced in order to simulate fully bonded interfaces. The PF internal length l is set very small for both layers (see Table 5), to reproduce LEFM predictions as proven in [72]. The results of the simulations are shown in Fig. 46. The first layer that shows crack nucleation is the second one (material 2). In

Geometry parameters		
L	6 mm	Specimen length
l_y	0.25 mm	Layer thickness
h	0.005 mm	Interface thickness
Mechanical parameters material 1		
E_1	70000 MPa	Material 1 Young modulus
v_1	0.34	Material 1 Poisson ratio
$\mathcal{G}_1$	0.025 N/mm	Material 1 fracture energy
l_1	0.0075 mm	Material 1 PF length scale parameter
Mechanical parameters material 2		
E_2	300000 MPa	Material 2 Young modulus
v_2	0.14	Material 2 Poisson ratio
$\mathcal{G}_2$	0.005 N/mm	Material 2 fracture energy
l_2	0.0075 mm	Material 2 PF length scale parameter
Mechanical parameters interface		
k_0	2000 MPa/mm	Initial stiffness of interface
$\sigma_{c,0}$, $\tau_{c,0}$	100 MPa	Initial peak stress of the tough interface
$\mathcal{G}_c^i$	2.5 N/mm	Critical energy release rate for tough interface
$\sigma_{c,0}$, $\tau_{c,0}$	1 MPa	Initial peak stress of the brittle interface
$\mathcal{G}_c^i$	0.025 N/mm	Critical energy release rate for brittle interface
$\sigma_{c,0}/\sigma_c$, $\tau_{c,0}/\tau_c$	1	Ratio between the initial and final value of the peak stress of the interface

Table 5: Geometry and material parameters.

this layer two parallel cracks are predicted to propagate (Fig. 46 (a)) simultaneously and can be considered as two branches of the initial notch in the layer 1. After increasing the applied load, each crack in the second layer further branches in the next brittle layer (Fig. 46 (b)). The same process continue for the next brittle layer but only two branches are developed (Fig. 46 (c)). At this stage, the cracks in the brittle layers start connecting through the material 1. Finally, failure of the specimen is achieved (Fig. 46 (d)) and it is the result of a complex crack path mostly localized in the mid-span position.

In the second simulation, we introduce interface elements between each layer. The parameters used for the interface are $\sigma_{c,0} = \tau_{c,0} = 100$ MPa and $k_0 = 2000$ MPa/mm to model a stiff brittle interface. As can be expected, the evolution of the predicted crack pattern is very different from that of the previous simulation. The first layer showing the appearance of cracks is the second layer (Fig. 47 (a)) with the same pattern as in

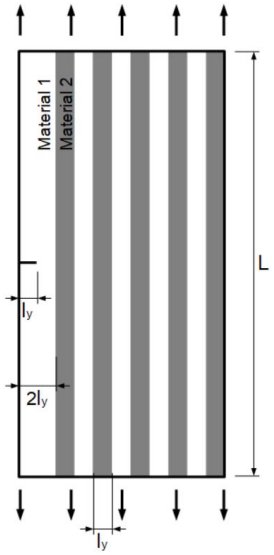

Figure 45: Specimen geometry.

the first simulation. Immediately after that, delamination events along the interface between the first and the second layers take place (Fig. 47 (b)). Then, the first layer is cracked by the propagation from the notch (Fig. 47 (c)). Continuing the simulation, cracking proceeds in the material 2 layers together with the development of delamination at interfaces (Fig. 47 (d)). At failure, delamination makes the crack pattern distributed along the whole specimen, contrary to the first simulation. Another important aspect is that the majority of the material 1 layers are not cracked, apart from the first layer containing the notch.

In the third simulation we introduce a more brittle interface, setting $\sigma_{c,0} = \tau_{c,0} = 1$ MPa and $k_0 = 2000$ MPa/mm. The evolution of the crack pattern is totally different from the previous two cases herein analysed (Fig. 48). Thus, in the current case, first, delamination is predicted to occur between the first and the second layer (Fig. 48 (a)). Then, the crack starts propagating from the notch until it impinges on the delaminated interface (Fig. 48 (b)). Subsequently, branching is predicted to take place

in the second layer (Fig. 48 (c)), and each branched crack is developed starting from where the delamination was stopped. Furthermore, crack penetration triggers delamination of the second interface. Finally, the sample failure is reached with a sudden development of delamination in all the interfaces and cracks in the brittle layers (Fig. 48 (d)). Again, the material 1 layers have been preserved from cracking.

The force-displacement curves of the above three simulations are shown in Fig. 49. All of them present an initial nonlinearity due to the formation of damage in the bulk. After that, the curve of the first simulation starts losing the load-bearing capacity slowly with a smooth drop. This is due to the gradual crack propagation within the specimen. The curves corresponding to the second and the third simulations show a completely different failure pattern and the nonlinear effects are much more pronounced in the load-displacement curve due to delamination. The development of cracking and delamination events cause multiple drops in the force.

The correspondence between crack/delamination events and the drops in the force can be examined closely in Fig. 50. In these graphs, the force-displacement curves are plotted together with other two quantities, the total crack propagation length and the crack propagation length in the bulk. The former is the sum of the length of the developed delamination and the length of the crack in the bulk. The latter is just the sum of the length of the cracks in the bulk. Both quantities are normalized with respect to the layer thickness, l_y. These plots show that, in general, delamination and cracking events occur simultaneously. This is in agreement with the patterns in Figs. 47, 48, where in some cases delamination triggers crack formation in the layers or vice versa. Another important consideration is that the delamination length in the simulation with brittle interfaces is bigger than the in simulation with tougher interface.

Finally we compare the results with what was theorized in [135] with the Cook-Gordon mechanism. According to that theory, the introduction of a brittle interface should increase the apparent material strength. The results reported in Fig. 49 seem to challenge this theory and a brittle interface reduces the apparent material strength as compared a tougher

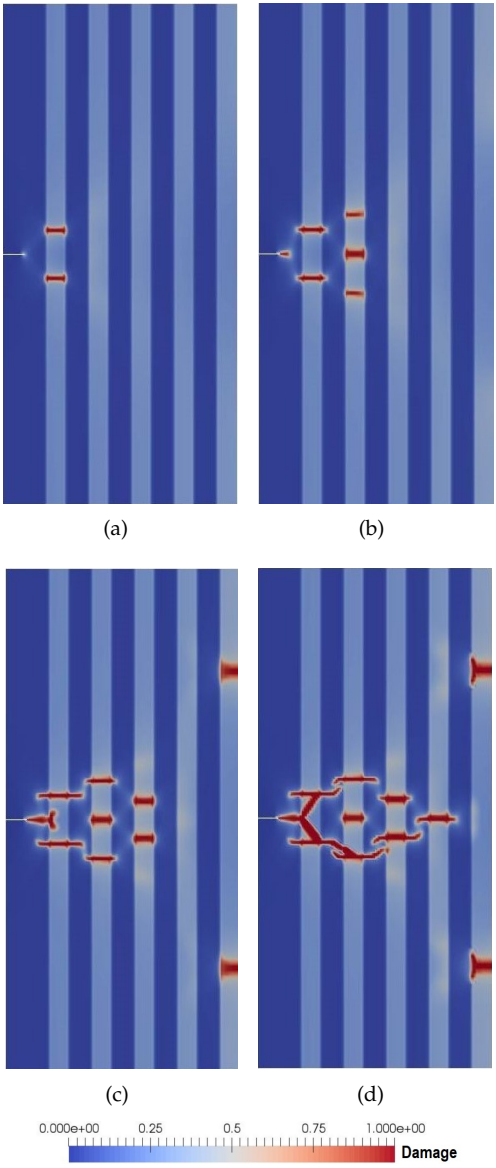

Figure 46: Crack evolution in the simulation with fully bounded layers.

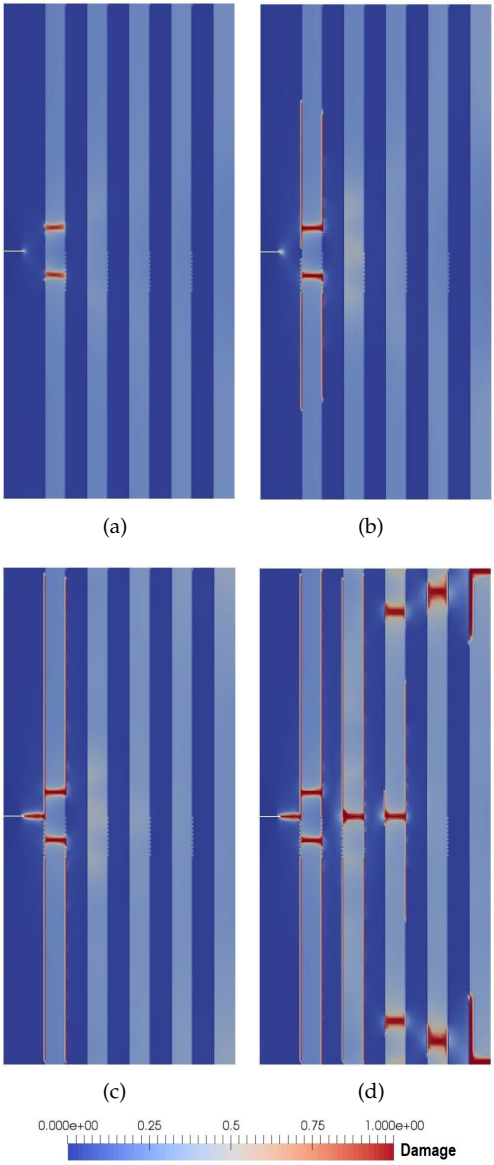

Figure 47: Crack evolution in the simulation with tough interface ($\sigma_{c,0} = 100$ MPa).

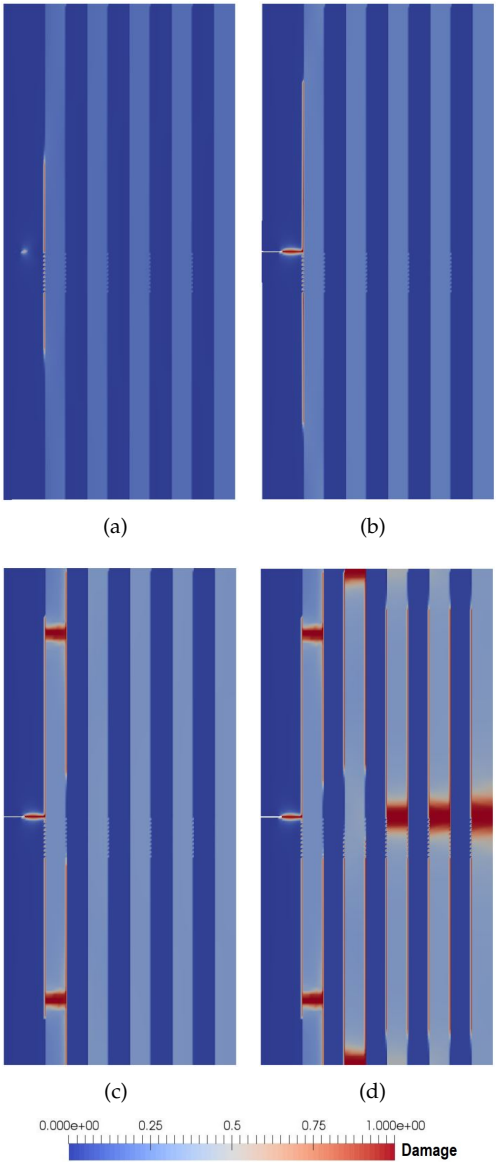

Figure 48: Crack evolution in the simulation with brittle interface ($\sigma_{c,0} = 1$ MPa).

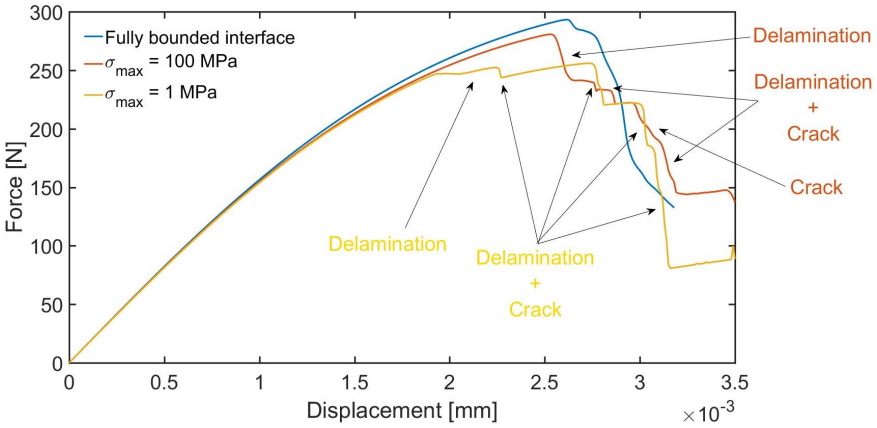

Figure 49: Force-displacement curve of the three simulations.

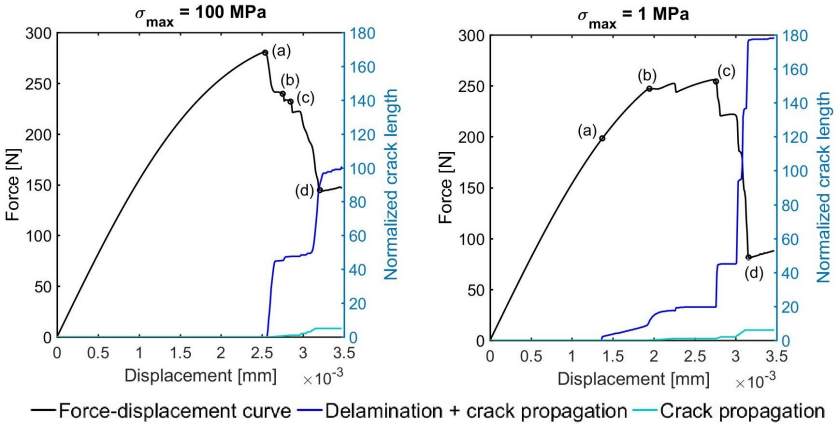

Figure 50: Force displacement curve compared with the crack and delamination length for the case of $\sigma_{\max}$ = 100 MPa (left) and $\sigma_{\max}$ = 1 MPa (right) normalized by the layer thickness l_y. The letter refer to the corresponding image in Fig. 47 for the case of $\sigma_{\max}$ = 100 MPa and to Fig. 48 for the case of $\sigma_{\max}$ = 1 MPa.

one.

This contradiction can be explained by noting that the assumptions behind the Cook-Gordon model are not satisfied in the present setting.

One of the most relevant differences relies on the fact that in the Cook-Gordon model the material is considered homogeneous and elastic until the condition of fracture of the interface is achieved. After delamination, discontinuities are considered along the interface and, consequently, the interface starts interfering with the linear elastic fracture mechanics crack tip stress distribution. In the present model, on the other hand, interfaces are introduced as another compliant material from the very beginning of the simulation. In [97], it is shown that the behaviour of such a system depends on the ratio between the interface process zone size and the bulk energy dissipation zone size (l_{CZM}/l). Depending on this ratio, the apparent strength of the overall material ranges between the strengths ruled by the following limit models: a model with prefect bonded interfaces and finite l; a model with elastic bulk material and finite l_{CZM}. In our simulations, the ratio l_{CZM}/l is kept constant. In fact, the bulk properties do not change (then l is constant), and l_{CZM} is constant since k does not change in our simulations. The latter is a consequence of the dimensional analysis performed in [97] from which we have $l_{CZM} \propto EG_c^i/\sigma_{\max}^2 = E/(2k)$. The consequence of having a constant ratio l_{CZM}/l is that delamination is triggered earlier in the presence of a brittle interface. Due to this, we have also longer delamination paths for a brittle interface.

These conclusions lead to the second important difference with respect to the Cook-Gordon model, where the load is supposed to be applied as a remote tensile stress at infinity. The assumption of infinite plane plays an important role, since there is no constrain on the size of the delamination path. As a result, a brittle interface could lead to a longer delamination with a consequent delayed crack propagation, increasing the elastic energy release rate. The specimens that we simulated are not long enough to be considered as infinite. Due to that, when the interface is brittle, delamination reaches the boundaries of the specimen causing the failure of the whole interface. This is also what accelerates the final failure of the specimen. As a result, for a brittle interface, the apparent strength of the specimen results to be lower than for a more ductile one.

Finally, there are other assumptions made in the Cook-Gordon model that are not in line with the hypotheses of the present approach. For instance, Cook and Gordon neglected the effect of the vertical stress σ_y in the interface fracture criterion. They made this simplification because their system is an homogeneous material with an interface, while here we have a laminate with different elastic properties for the laminae. This means that σ_y is not constant across the laminae and there are jumps in correspondence of the interfaces. We cannot say quantitatively which is the effect of the variation of σ_y on the interface delamination and on the overall strength. Nevertheless, we have good motivations to believe that σ_y cannot be neglected and that in any case is a source for possible discrepancies with respect to the Cook-Gordon model predictions.

5.1.2 Crack propagation in silicon nitride/boron nitride microlaminate

In this section, we reproduce the experimental results in [133] concerning the 4-point bending test of a silicon nitride/boron nitride (Si_3N_4/BN) microlaminate. Both constituent materials are brittle ceramics. The laminate is structured with layers of Si_3N_4 of thickness between 40 μm and 60 μm, alternated by layers of BN of variable thickness between 2 μm and 10 μm (Fig. 51 (a)). The BN layers act as brittle interface between the Si_3N_4 layers.

The 4-point bending test geometry is shown in Fig. 51 (b). The dimensions of the specimen are: total span L = 5 mm, thickness T = 3 mm, width W = 4 mm. The outer and inner span of the 4-point bending test are, respectively, $S_1 = 4$ mm and $S_2 = 2$ mm. This geometry is modelled with phase field elements for the Si_3N_4 layers, representing the bulk material, and cohesive interface elements compatible with phase field for the BN layers. Due to the variable thickness of the Si_3N_4 layers, in our simulation the thickness associated to the layers of this material is set equal to 40, 50 or 60 μm. The assignment of the Si_3N_4 layer thickness is randomly chosen according to a uniform distribution. The interface thickness, on the other hand, is set constant and equal to 5 μm. The material and frac-

ture parameters of the bulk are: Young modulus E = 310 GPa, Poisson ratio ν = 0.27, fracture energy $\mathcal{G}_s$ = 9 μN/μm and phase field internal length scale l = 2 μm. The interface parameters are: $\sigma_{c,0} = \tau_{c,0} = 32$ MPa and $k_0 = 70$ MPa/μm.

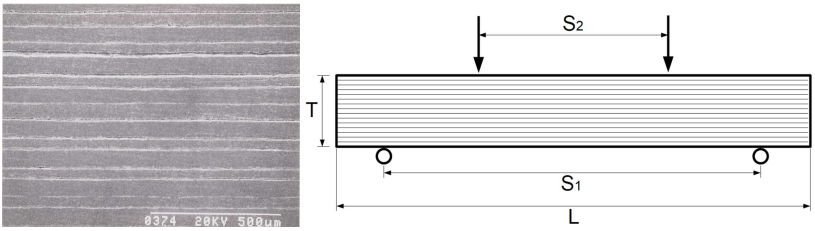

(a) (b)

Figure 51: (a) Si_3N_4/BN structure of the microlaminate; (b) 4-point bending experimental test geometry. Image (a) with permission from [133].

The experimental force-displacement curve (Fig. 52) shows an initial linear behaviour until the peak load of 475 N is reached. After this point, the load-carrying capacity of the specimen drops down to around 40% of the peak load. Then, the load continue increasing until a second drop is observed when the value of 240 N is reached. After this second drop, the load-carrying capacity is reduced to 10% of that at peak load. The specimen maintains this level until final failure.

Fig. 53 shows the evolution of the predicted crack pattern. Due to symmetry of the geometry and of the boundary conditions only half of the domain has been simulated, using around 380000 finite elements nodes and finer mesh where the crack is expected to propagate. The simulation shows an initial linear behaviour until the peak load of 475N is reached (Fig. 53(a)). Then, an interface situated in the middle of the specimen thickness fails due to delamination (Fig. 53(b)). After this first delamination event, the specimen continues gaining load-carrying capacity until the Si_3N_4 layers start failing. According to the numerical predictions, the layers that first fail are those at the intrados one and the one immediately next to the delaminated interface (Fig. 53(c)). The crack

is predicted to continue its propagation towards the extrados of the specimen until final failure (Fig. 53(d)). The result of the simulation in terms of force-displacement curve shows a good agreement with the experimental one (Fig. 52). The initial part of the curve, the peak load and the drop in load-carrying capacity are very well predicted, capturing the critical load at which damage events occur. The final part of the simulation shows a more progressive failure evolution until collapse. This is not in perfect agreement with experiments, since we suppose that the second drop in the force noticed in experiments is caused by a second severe delamination event which we were not able to reproduce numerically. One possible source for this mismatch can be attributed to the interface parameters, since no experimental characterization was available.

Another important result of the simulation is the very satisfactory prediction of the crack pattern features conforming to the experimental evidences. The experimental image in Fig. 54 (a) shows the strong crack deflection and branching developed due to delamination. The same behaviour has been reproduced by the numerical simulation (Fig. 54 (b)) where both phenomena are present in the simulated crack pattern.

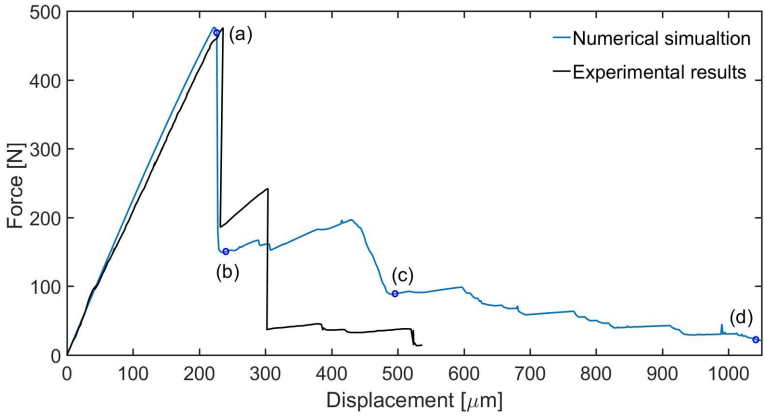

Figure 52: Numerically predicted vs. experimental force-displacement curves.

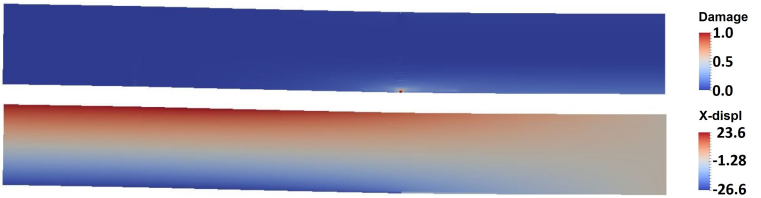

(a) Damage initiation before the first delamination.

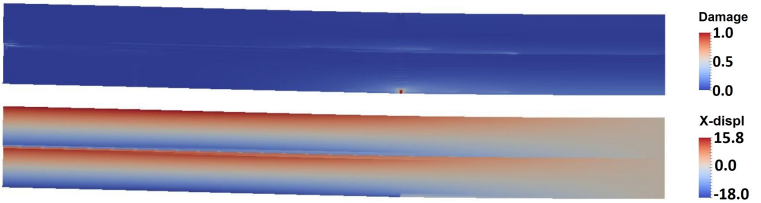

(b) Delamination of the middle layer.

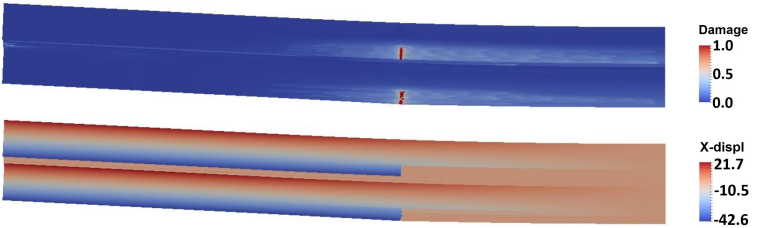

(c) Crack propagation through the layers.

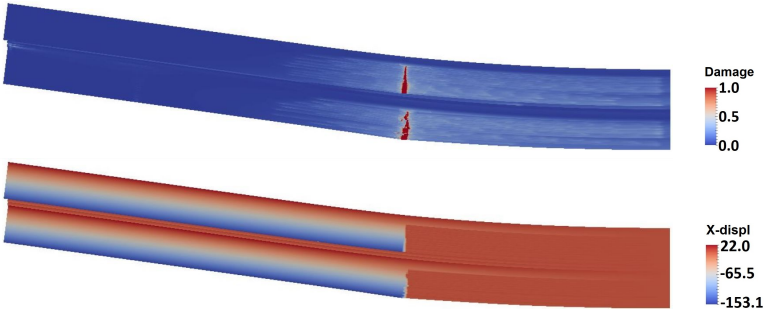

(d) Specimen failure.

Figure 53: Fracture propagation and delamination resulting from the numerical simulation. For each subfigure there is the damage contour plot on top and the x-displacement contour plot on bottom.

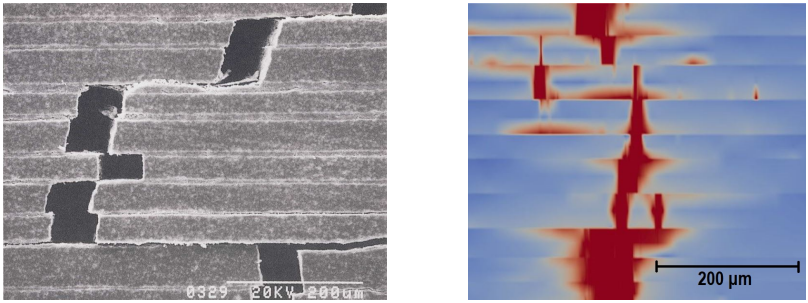

(a) (b)

Figure 54: (a) experimental crack pattern; (b) numerical result of the crack pattern. Image (a) with permission from [133].

5.1.3 Crack propagation in Al/SiC nano-laminates

In line with the previous applications, the experiments described in Section 2.2 are simulated. The simulations concern the results of the tensile test with layers perpendicular to the loading direction. The computational model used consist in the coupling between the PF and CZM. The PF model is used to describe the constitutive behaviour of the Al and SiC layers. The CZM is used to describe the behaviour of the interfaces.

The comparison between the simulation predictions with the experimental results, shade light on the properties of the interface. Unfortunately, the data available are not sufficient for the characterization of fracture properties of the two constituent materials. This is addressed to the fact that the tensile tests with layers parallel to the tensile direction fail prematurely due to the presence of columnar boundaries (Fig. 18 (a)).

Some considerations about the experimental results have to be done before the description of the computational procedure. First of all, it has to be considered that the stress-displacement curves provided in Section 2.2 are affected by machine imprecision in the measure of the displacement. Effects like deformation of the head of the specimen, specimen relaxation or image drifting has to be considered in the displacement measure. Unfortunately, the amount of the displacement affected by the

listed phenomena cannot be quantified. Moreover, it is probable that small plastic deformations are developed during the test. This deformation cannot be captured by our computational model. The PF model is suitable for brittle and quasi-brittle fracture. In order to account for the probable small plasticity developed in the Al layer, the internal length parameter l of the PF is set with a high value. In this way, we try to substitute the inelastic deformation given by plasticity with the inelastic deformation given by the damage. The experimental value of the stress, indeed, is a very precise measure. For all these reasons, the characterization of the interface is done in terms of peak stress.

Mechanical parameters of the Al/SiC nanolaminate		
E_{Al}	70000 MPa	Al Young modulus
v_{Al}	0.34	Al Poisson ratio
E_{SiC}	300000 MPa	SiC Young modulus
v_{SiC}	0.14	SiC Poisson ratio
Fracture parameters for the 50 nm layers		
G_{Al}	5 μN/μm	Al fracture energy
l_{Al}	0.025 μm	Al PF internal length
G_{SiC}	64 μN/μm	SiC fracture energy
l_{SiC}	0.025 μm	SiC PF internal length
σ_{max}	2100 MPa	Interface peak stress
K	5e5 MPa/μm	Interface stiffness
Fracture parameters for the 100 nm layers		
G_{Al}	2.5 μN/μm	Al fracture energy
l_{Al}	0.05 μm	Al PF internal length
G_{SiC}	60 μN/μm	SiC fracture energy
l_{SiC}	0.05 μm	SiC PF internal length
σ_{max}	1400 MPa	Interface peak stress
K	5e5 MPa/μm	Interface stiffness

Table 6: Geometry and material parameters of the tensile test.

The geometry and the imposed boundary conditions of the two simulated tensile tests are resumed in Fig. 55. The material parameter which has demonstrate to best fit the experimental peak stress are given in Table 6. Fig. 56 shows the predictions of the specimens at failure. In the case of 100 nm layer the failure is very brittle. There is a diffuse damage in the Al layer and a peak of the damage in the proximity of the interface that fails (Fig. 56 (b),(d)). This damage characterizes the small nonlinearity in the

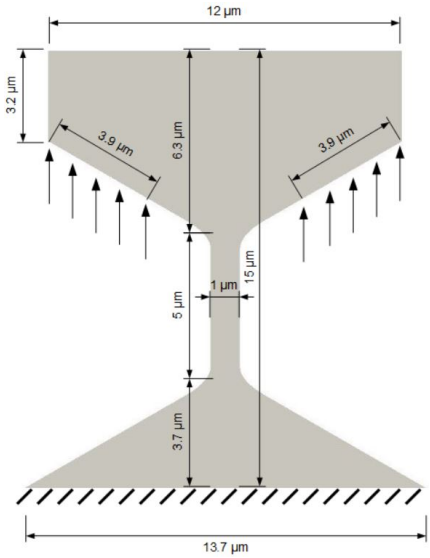

(a)

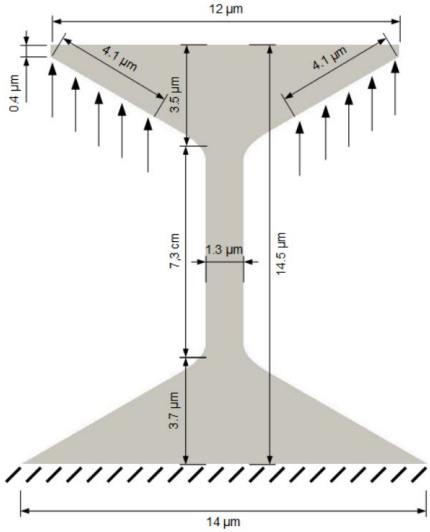

(b)

Figure 55: Geometry of the simulated tensile tests: (a) 50 nm layer thickness; (b) 100 nm layer thickness

resultant stress displacement curve (Fig. 57). In the case of 50 nm layers, the fracture energy of the Al is reduced. In this way a stronger nonlinearity is predicted and the Al layer fail together with the interface (Fig. 56 (a),(c)). Then, the crack pattern reproduce the experimental phenomenon in which the crack involve two interfaces and a layer. Consequently, the stress-displacement curve (Fig. 57) shows a stronger nonlinearity.

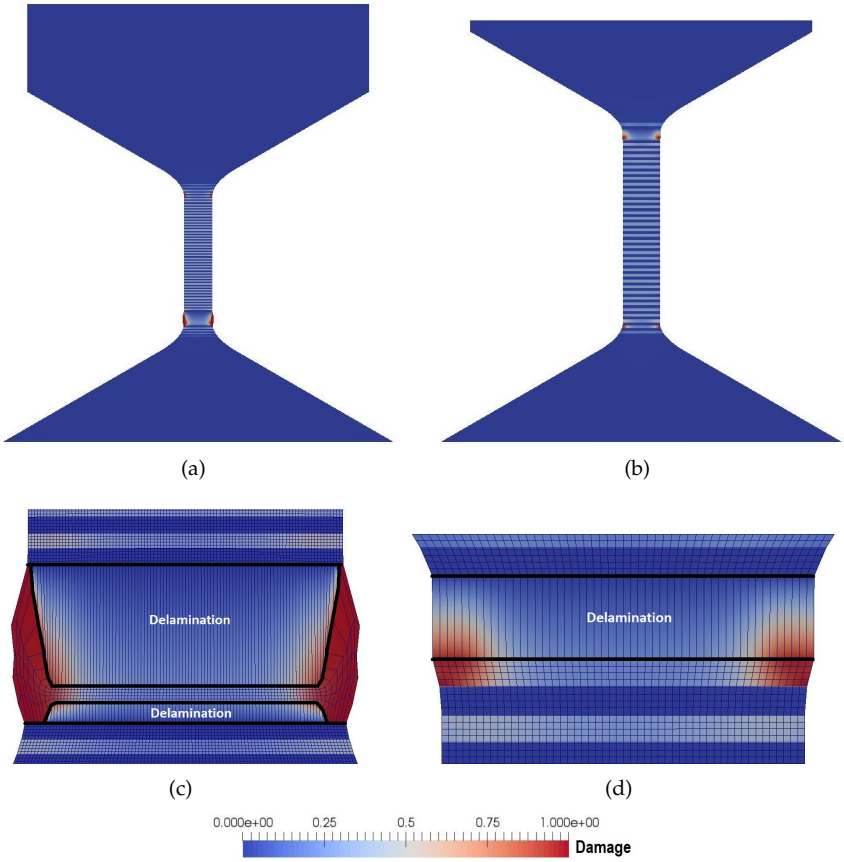

Figure 56: Failure of the specimens during the tensile test: (a) 50 nm layer thickness; (b) 100 nm layer thickness; (c) zoom on the 50 nm layer fail area: it is evident the competition between damage in the bulk and delamination; (d) zoom on the 100 nm layer fail area: pure delamination.

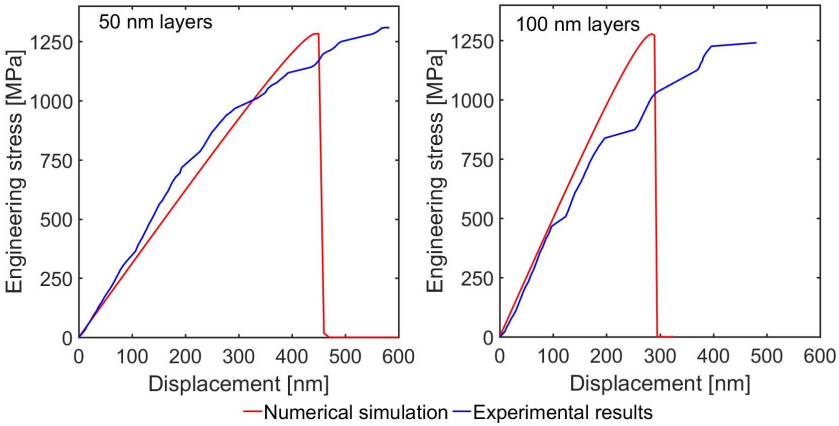

Figure 57: Stress-displacement curve comparison between the numerical prediction and the experimental results.

5.2 3D applications

In this section, the modelling capabilities of the proposed 3D computational framework coupling the PF approach of fracture and the CZM for interface cracking for finite elasticity (Section 3.1.3 and 3.2.2) are assessed through several examples. The main objective of these simulations concerns showing the ability of the proposed model to simulate different crack propagation paths in heterogeneous materials and engineering structural components with different 3D geometries.

In the first example we aim to show the effect of the interaction between the PF and the CZM within the proposed model. A tensile test of a flat single-edge notched specimen of a homogeneous material is then considered. The second and third examples illustrate the potentialities of the combined use of the enhanced-based solid shell formulation together with the 3D interface. These applications comprise the simulation of heterogeneous specimens using out-of-plane loading with planar structures (Section 5.2.2), and membrane loading with curved geometry (Section 5.2.3). Finally, an experimental case study regarding fracture

predictions in photovoltaic (PV) panels is considered (Section 5.2.4). In particular, a 4-point bending test of a solar panel is simulated, being the corresponding results correlated with experimental data taken from the related literature. All the simulations have been performed with the finite element program FEAP [10]. Dirichlet boundary conditions applied with a monotonically increasing law are defined in the numerical examples herein addressed.

5.2.1 Single-edge notched specimen

The first insight onto the potentialities of the proposed model is presented by means of the simulation of a flat single-edge notched specimen under uniform tensile loading. The geometry of the specimen is shown in Fig. 58. An interface perpendicular to a middle notch runs along all the length of the specimen. A prescribed displacement along the y-direction is prescribed at the top and bottom edges of the specimen. The material and geometry parameters used are collected in Table 7.

Several simulations with various interface parameters have been performed in order to show the different crack patterns that can be activated. According to [138], the occurrence of delamination together with crack propagation is governed by the interface maximum tensile traction. These authors claimed that when the length of the initial delamination or crack penetration is much smaller then the global dimension, crack deflection is confined within the stress field. In line with these considerations, in the system defined in Fig. 58, the global dimension L is much larger than the crack penetration/delamination length (the specific ratio between those dimensions is higher than 10). Therefore, we focus our parametric analysis on the variation of the peak traction of the interface in order to evaluate the accuracy of the proposed method with respect to linear elastic fracture mechanics predictions.

The computational model herein used is composed of 11794 nodes. The mesh is refined in correspondence of the centre of the specimen to achieve the convergence during crack propagation. The maximum ten-

Geometry parameters		
L	1 mm	Plate length
t	0.003 mm	Plate thickness
h	0.0001 mm	Interface thickness
Mechanical parameters for the PF model		
E_{b}	3240 MPa	Bulk Young modulus
υ_{b}	0.35	Bulk Poisson ratio
G_{b}	0.35 N/mm	Bulk fracture energy
l_{b}	0.02 mm	Phase Filed length scale parameter
G_{i}	0.35 N/mm	Interface fracture energy for mode I, mode II and mode III
$\sigma_{\max}$	1000 75 MPa	Interface maximum tensile traction for mode I, mode II and mode III
$g_{\mathrm{c},0}$	7e-4 0.014 mm	Interface initial critical opening for mode I, mode II and mode III
$g_{\mathrm{c}}/g_{\mathrm{c},0}$	1 5	Interface opening ratio for mode I, mode II and mode III

Table 7: Geometry and material parameters of the tensile test.

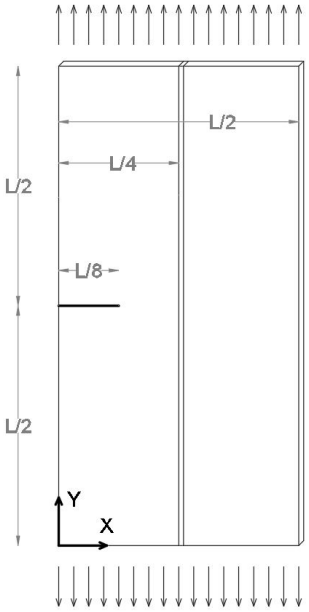

Figure 58: Specimen geometry.

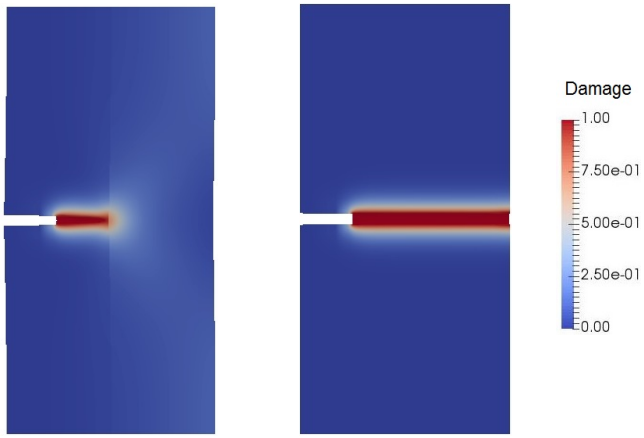

(a) Crack impinging on the interface

(b) Specimen failure

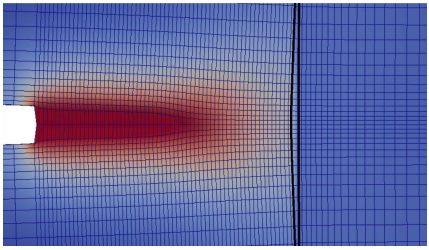

(c) Delamination of the interface (shown in black solid lines)

Figure 59: (a) & (b) two steps of crack propagation; (c) close-up view of delamination when the crack is approaching the interface.

sile (Mode I) traction of the CZM has been increased from 75 MPa to 1000 MPa. Moreover, the final interface critical opening for $\mathfrak{d} = 1$ (g_c) takes the following values: $g_c = g_{c,0}$, $2g_{c,0}$, $5g_{c,0}$. The general evolution of the simulations is shown in Fig. 59 for each of the cases defined above. In this graph it can be observed that the crack propagates straight in the bulk, and when imping on the interface two scenarios might occur depending on the interface peak traction: (1) no delamination is developed at the

interface and the crack starts propagating in the right bulk; (2) delamination occurs at the interface, so that the crack propagation in the adjacent bulk is delayed.

This behaviour can be recognized from the force-displacement curves in Fig. 60. In particular, when delamination occurs, the curve is characterized by two drops in carrying capacity of the system: the first kink

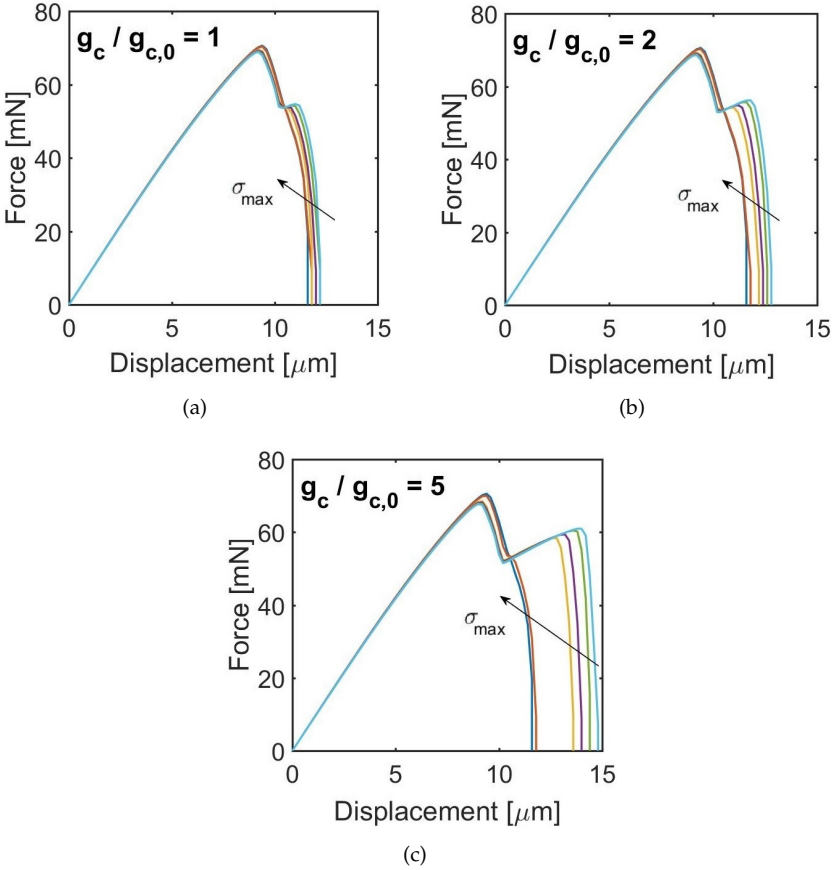

(a) (b) (c)

Figure 60: Force displacement curve varying $\sigma_{\max}$ and the ratio $g_c/g_{c,0}$. The arrow shows the direction of increasing of $\sigma_{\max}$.

corresponds to the failure of the left part and the second one is associated with the failure of the right part. The concurrence of crack propagation and delamination together is obtained for 75 MPa $< \sigma_{\max} <$250 MPa. For values of $\sigma_{\max} \geq 250$ MPa, the interface is stiff enough such that the crack propagates in the bulk without delamination.

The ratio $g_c/g_{c,0}$, which governs the coupling between the PF and the CZM, is also affecting the fracture predictions. High values of this ratio cause longer delamination paths. In fact, when $g_c/g_{c,0} > 1$, the damage in the bulk makes the interface more compliant and consequently the actual $\sigma_{\max}$ decreases according to the present model. Under this condition, delamination is triggered earlier. As a side effect, the crack propagation into the adjacent layer is delayed. This behaviour can be identified also in the force-displacement curve in Fig. 60 through observing that the second drop in the evolution curve is predicted to take place for larger displacements as $g_c/g_{c,0}$ increases.

5.2.2 Flat sandwich panel under 4-point bending and tension

This example concerns the fracture of a flat sandwich panel subjected to combined in-plane and out-of-plane loading (Fig. 61). The sandwich panel is made of three brittle layers with an interface between each layer. The topmost layer is characterized by a notch in the middle of the span that runs along over the complete width of the specimen, whereas its depth is equal to half its thickness. The topmost and the bottommost layers are assumed to have the same material parameters, while the middle layer is made of a stiffer material (Fig. 62). All the relevant material parameters used in the present application are reported in Table 8.

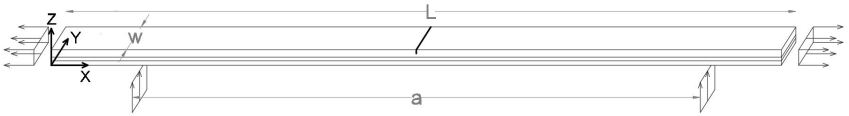

Figure 61: Geometry of the specimen under 4-point-bending and tension.

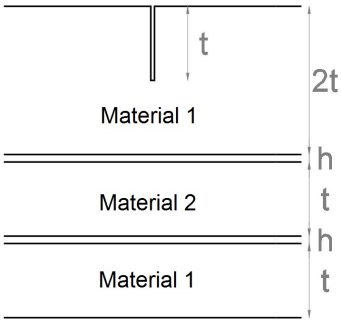

Figure 62: Sandwich panel structure along the thickness.

Geometry parameters		
L	2 mm	Panel length and outer bending span
w	0.5 mm	Panel width
a	1.556 mm	Inner bending span
t	0.01 mm	Main thickness
h	0.001 mm	Interface thickness
Δ_x/Δ_y	2	ratio between the in-plane (Δ_x) and out-of-plane (Δ_y) loading
Mechanical parameters		
E_1	100 GPa	Material 1 Young modulus
v_1	0.3	Material 1 Poisson ratio
G_1	0.5 N/mm	Material 1 fracture energy
l_1	0.05 mm	Material 1 Phase Filed parameter
E_2	200 GPa	Material 2 Young modulus
v_2	0.2	Material 2 Poisson ratio
G_2	1.0 N/mm	Material 2 fracture energy
l_2	0.05 mm	Material 2 Phase Filed parameter
G_{i}	0.5 N/mm	Interface fracture energy for Mode I, Mode II and Mode III
$\sigma_{\max}$	1000 and 0.01 GPa	Interface maximum tensile stress for Mode I, Mode II and Mode III
$g_{\mathrm{c}}/g_{\mathrm{c},0}$	1	Interface opening ratio for Mode I, Mode II and Mode III

Table 8: Sandwich panel geometry and material parameters.

By exploiting the symmetry of the system and of the applied boundary conditions, we consider only half domain for the simulations. The model has 12376 nodes and is refined in proximity of the notch. Two different simulations are carried out: the first simulation concerns with a

strong interface ($\sigma_{max} = 1x10^6$ MPa), where the second case comprises a weak interface definition ($\sigma_{max} = 10$ MPa).

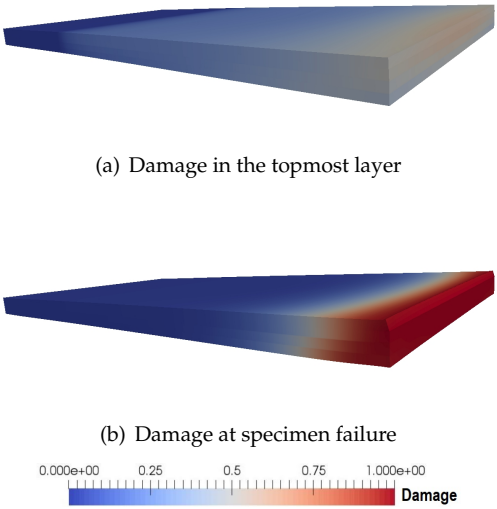

(a) Damage in the topmost layer

(b) Damage at specimen failure

Figure 63: Damage contour plot of the flat sandwich panel under tension and 4-point bending for the case of strong interfaces, showing crack through the specimen without delamination

In the simulation with a stronger interface, damage evolution is predicted to propagate from the notch (Fig. 63 (a)), and the final failure follows immediately after crack propagation (Fig. 63 (b)). Numerical results predict bulk failure without any delamination. On the contrary, for a weaker interface ($\sigma_{max} = 10$ MPa), the failure sequence follows this order: (1) failure of the topmost notched layer (Figs. 64(a), 65(a)), (2) interfacial delamination between the topmost and the middle layer (Figs. 64(b), 65(b)), (3) bulk failure of the middle layer (Figs. 64(c), 65(c)), (4) delamination between the middle and the bottommost layer (Figs. 64(d), 65(d)), (5) failure of the bottommost layer (Figs. 64(e), 65(e)).

Fig. 66 depicts the reaction force vs. the out-of-plane displacement curves for the above two scenarios. The strong interface evolution shows

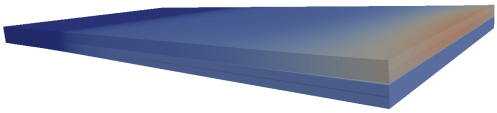

(a) Damage initiation in the topmost layer

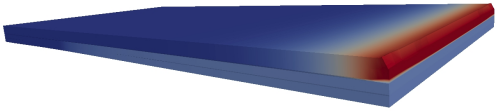

(b) Complete cracking of the topmost layer

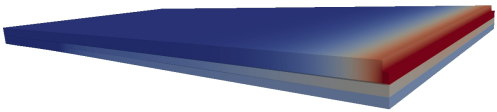

(c) Progressive cracking in the middle layer

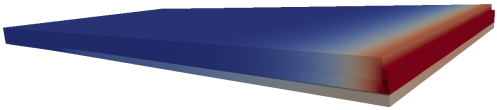

(d) Complete cracking of the middle layer and onset of delamination

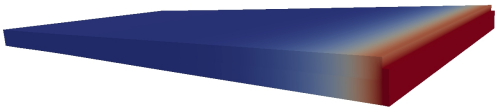

(e) Total specimen failure

Figure 64: Crack propagation evolution of the flat sandwich panel under tension and 4-point bending, for weak interface layer

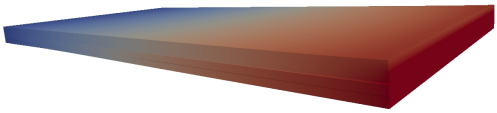

(a) Damage initiation in the topmost layer

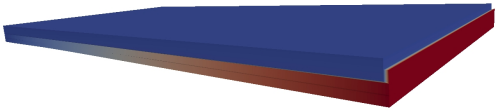

(b) Complete cracking of the topmost layer

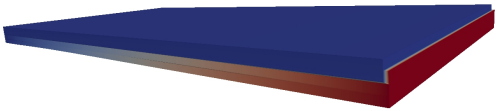

(c) Progressive cracking in the middle layer

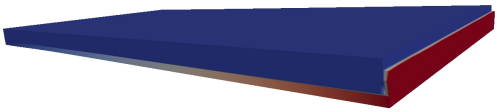

(d) Complete cracking of the middle layer and onset of delamination

(e) Total specimen failure

Figure 65: Delamination evolution of the flat sandwich panel under tension and 4-point bending, for weak interface layer

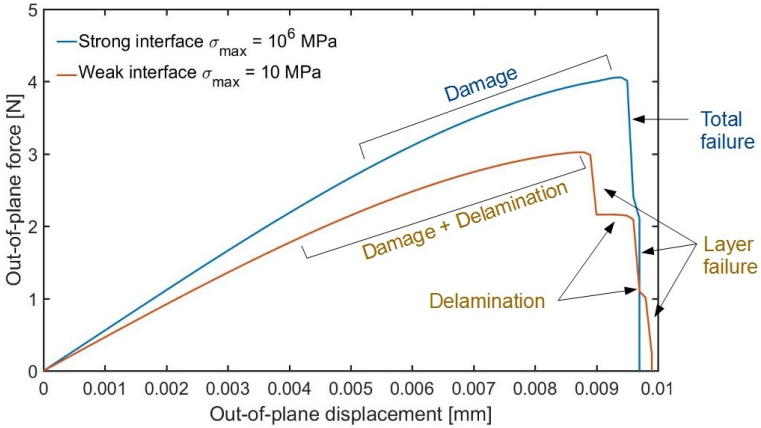

Figure 66: Force-displacement curve of the sandwich panel under tension and 4-point-bending

an initial nearly linear behaviour. Subsequently, nonlinear effects attributed to the deformation process and bulk damage can be identified. Finally, the absence of interface delamination leads to a characteristics brittle failure of the specimen upon failure. Conversely, the case including a weaker interface exhibits a much different response. Analysing the red curve in Fig. 66, it can be observed that nonlinear effects occur for much lower displacements due to the combination of three aspects: (1) the presence of geometrically bending deformation effects, (2) the development of bulk damage in the topmost layer, and (3) the onset and growth of delamination events which are provoked for the different stiffness values between adjacent layers. Moreover, at advanced stages, the evolution is characterized by several load drops. Specifically, these drops are directly associated with the failure of each of the composing layers, which concomitantly evolves with the progression of delamination along the adjoining interfaces.

5.2.3 Cylinder under tension

The proposed methodology is further examined in relation to a cylindrical geometry whose dimensions are: length $L = 2$ mm, external diameter $d_{\text{ext}} = 0.72$ mm, and inner diameter $d_{\text{int}} = 0.678$ mm (Fig. 67). The same material parameters used in Section 5.2.2 are considered, including the strong and weak interface cases.

The external layer is characterized by a notch which runs around all the circumference and its depth is half of its thickness. Due to the symmetry of the problem, the simulations are performed by considering $1/8$ of the total domain. The FE discretization presents by 13824 nodes. The specimen is loaded under tensile displacement along the x-direction.

Fig. 68 shows the force-displacement curves for a strong interface ($\sigma_{\text{max}} = 1\text{x}10^6$ MPa) and a weak interface ($\sigma_{max} = 10$ MPa). For the current application, delamination at each interface are predicted to take place for very small imposed displacements, simultaneously with bulk crack propagation.

This response stems from the fact that there are no bending effects. Therefore, the nonlinear evolution of both curves before the first drop in the load-carrying capacity is mostly due to the development of damage in the external layer. Furthermore, for the strong interface case, the failure is characterized by an almost perfect brittle evolution (sudden drop). In contrast, the weak interface scenario features a post-peak response as that noted in Section 5.2.2, from a qualitative standpoint (Figs. 69, 70).

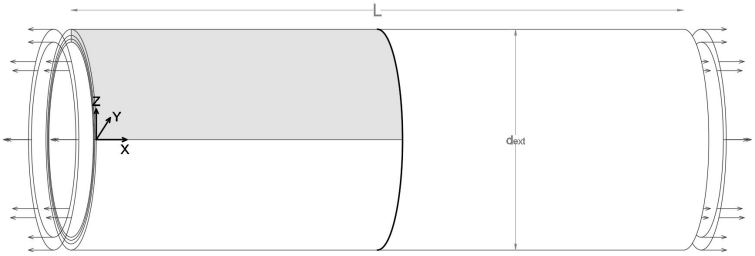

Figure 67: Geometry of the cylinder tension test. In grey is highlighted the symmetric domain considered for the simulation. The cross setion structure is the same depicted in Fig. 62.

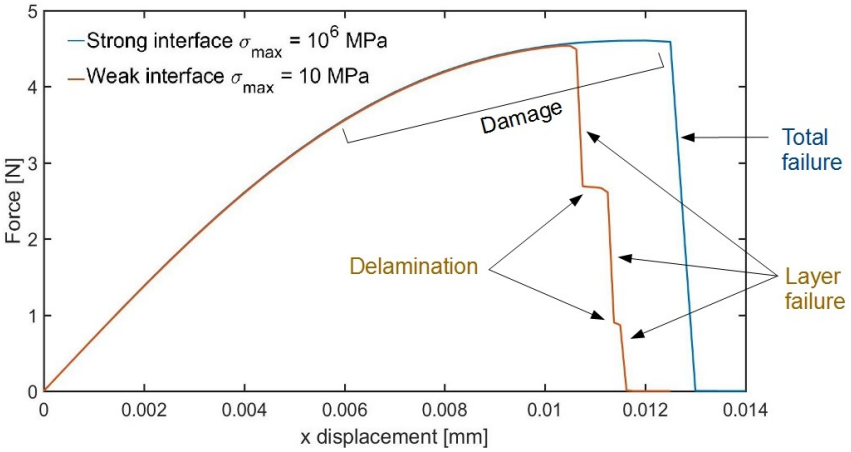

Figure 68: Force-displacement curves of the cylinder under tension

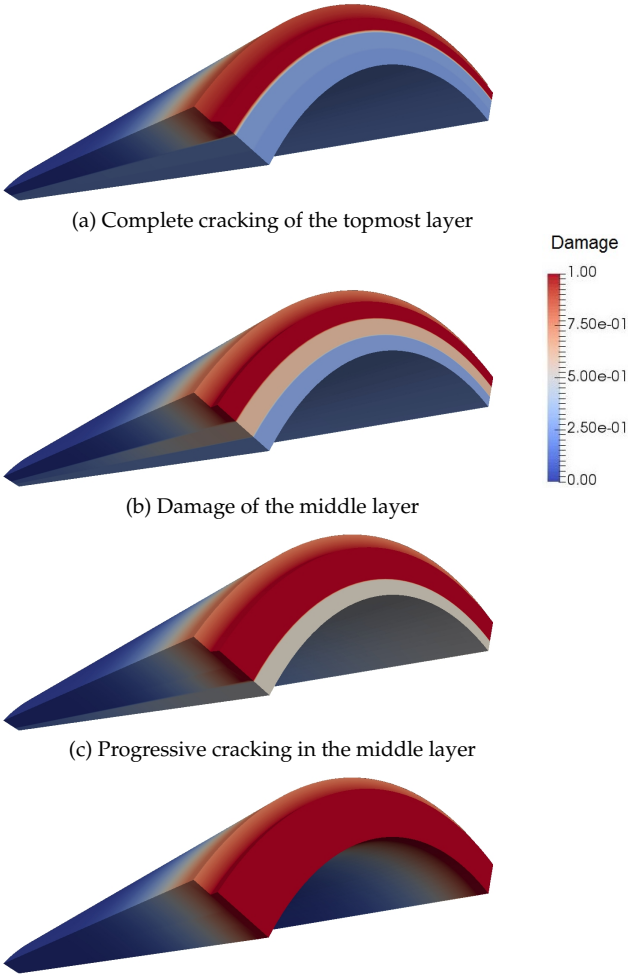

(a) Complete cracking of the topmost layer

(b) Damage of the middle layer

(c) Progressive cracking in the middle layer

(d) Complete cracking of the middle layer and onset of delamination

Figure 69: Crack propagation evolution of the sandwich panel with cylindrical geometry under tension, for weak interface layer.

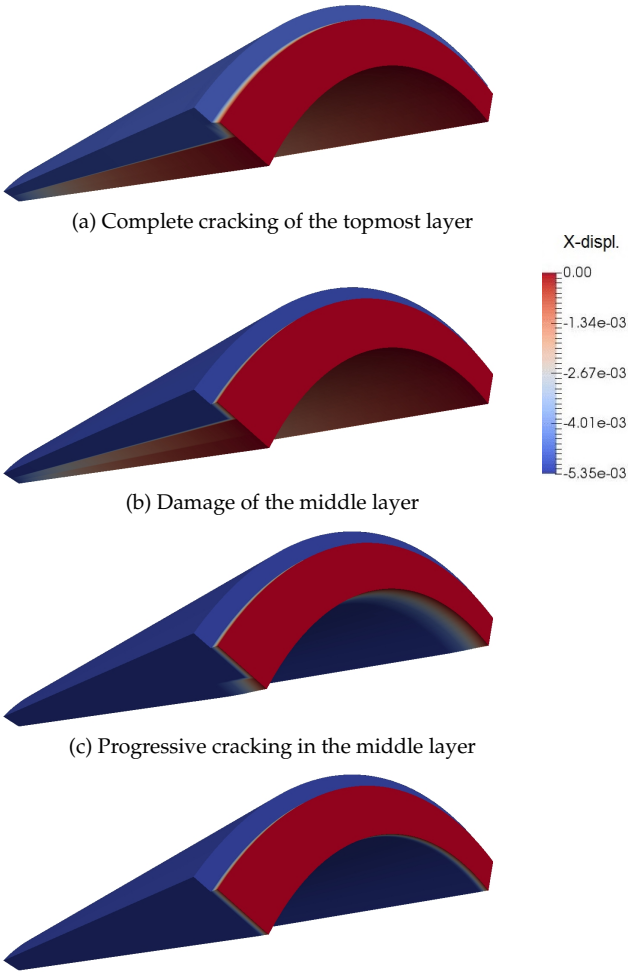

(a) Complete cracking of the topmost layer

(b) Damage of the middle layer

(c) Progressive cracking in the middle layer

(d) Complete cracking of the middle layer and onset of delamination

Figure 70: Delamination evolution of the sandwich panel with cylindrical geometry under tension, for weak interface layer.

5.2.4 Crack propagation in a solar photovoltaic panel

The last numerical example concerns the simulation of a 4-point bending experimental test of a photovoltaic (PV) module. The experimental test was performed and comprehensively described in [55]. A typical PV module is composed of 5 different layers (Fig. 71 (a)): the middle layer is made of solar cells, which are encapsulate in an adhesive material made of EVA, while the topmost and bottommost layers are made of glass and PET, respectively.

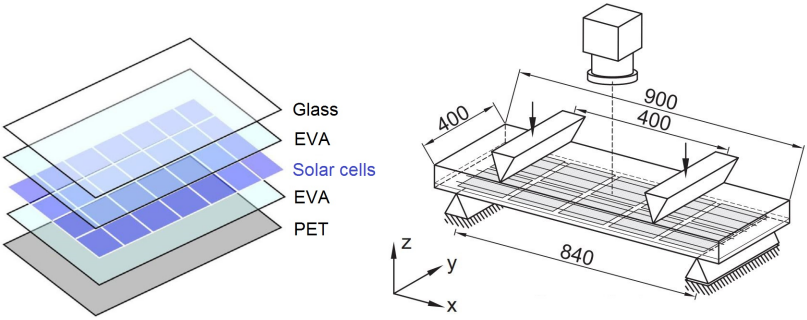

(a) PV panel structure.

(b) Experimental test setup (distances in mm).

Figure 71: Geometry and boundary conditions of the specimen PV panel.

The experimental set-up and the specimen geometry are shown in (Fig. 71 (b)). The panel is composed of 10 solar cells, which were disposed along two parallel rows (5 cells per row). An electroluminescence camera was positioned on top of the middle line in order to detect microcrack patterns. The experimental tests were conducted on specimens with busbars parallel or perpendicular to the applied displacement direction. Recalling the analysis carried out in [55], in the current investigation, we only consider the PV panel configuration with parallel busbars, where crack events are mostly concentrated along the middle line of the specimen.

The numerical model herein used to reproduce the experimental results comprises 11172 nodes. Again, the exploitation of symmetry con-

Mechanical parameters		
E_{Si}	130 GPa	Silicon Young modulus
υ_{Si}	0.16	Silicon Poisson ratio
G_{Si}	0.0432 N/mm	Silicon fracture energy
l_{Si}	0.04 mm	Silicon Phase Filed parameter
E_{EVA}	0.004 GPa	EVA Young modulus
υ_{EVA}	0.4	EVA Poisson ratio
E_{PET}	2.8 GPa	PET Young modulus
υ_{PET}	0.37	PET Poisson ratio
E_{Gl}	73 GPa	Glass Young modulus
υ_{Gl}	0.25	Glass Poisson ratio
G_{i}	100 N/mm	Interface fracture energy for Mode I, Mode II and Mode III
σ_{max}	1000 GPa	Interface maximum tensile stress for Mode I, Mode II and Mode III
$g_{\text{c}}/g_{\text{c,0}}$	1	Interface opening ratio for Mode I, Mode II and Mode III

Table 9: Sandwich panel geometry and material parameters.

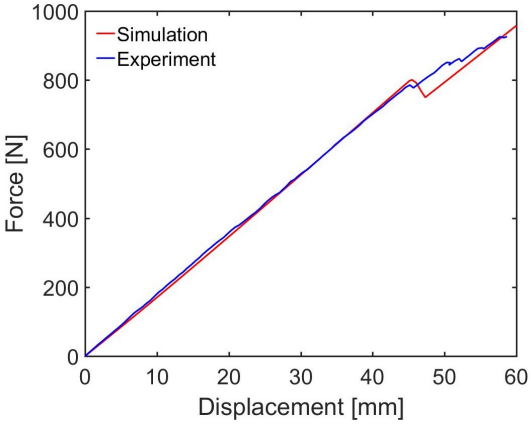

Figure 72: Force displacement curve.

ditions allows the discretization of just one quarter of the panel. The relevant material parameters for this test are collected in Table 9 complying within standard PV panels [139]. The middle layer of the specimen, corresponding to the solar cells, is modelled as a homogeneous single layer 0.166 mm thick with material properties of brittle Silicon (Si) (Table 9). The regularization parameter l_{Si} of the PF model for the Si layer is set

equal to 0.04 mm.

The EVA layers are 0.5 mm thick and the corresponding material properties, which strongly depend on temperature, are evaluated at room temperature. The bottommost PET layer and the topmost glass layer have a thickness equal to 0.1 mm and 2.55 mm, respectively. In between the Si and the EVA layers, interfaces 0.001 mm thick are introduced. Only PF fracture in the Silicon layer is allowed, due to its brittleness, and its competition with interface delamination is investigated.

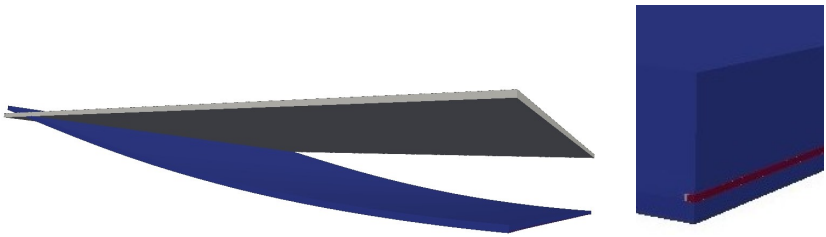

(a) Undeformed specimen (grey) and deformed specimen at failure (blue).

(b) Zoom on the failure line.

Figure 73: Simulation of the 4-point bending test on the PV panel.

The load-displacement curves corresponding to the experimental data and to the numerical predictions are shown in Fig. 72. The specimen response was characterized by an initial proportional load-displacement evolution up to a load level of around 800 N. This initial stage is satisfactorily reproduced by the current numerical method. Progressing along the loading application, the experimental evolution features a moderate variation of the stiffness of the specimen due to the development of microcracking phenomena in the Si cells. Analysing the corresponding numerical prediction, the present model enables capturing the load level at which this drop took place in the load-displacement curve with good accuracy. However, due to the fact that the present simulation devices a uniform Si layer instead of a cell-wise model, it is not possible to simulate the growth of multiple small cracks. This fact yields a load drop concentrated in one single event, rather than due to multiple cracks propagation. Nevertheless, it can be observed that at the final stage of such evo-

lution an (when cracking affected all the solar cells throughout the middle line of the panel), the numerical model captures the final stiffness of the panel, consistently with the experimental results. The deformed configuration at failure is shown in Fig. 73 (a) and cracking in the Si layer is shown in Fig. 73 (b).

Chapter 6

Conclusions and future developments

In the present thesis the PF model for brittle fracture and the CZM for cohesive fracture are adopted, extended and validated by numerical simulations and experiments. The coupling of these two models as well as their combination with other constitutive models such as plasticity or finite elasticity, leads to a modelling framework applicable to relevant problems in the field of material science and structural mechanics. In this dissertation we analyse problems at different scales and problems with materials with an heterogeneous structure.

The potential capabilities of the CZM are firstly employed in combination with the von Mises elasto-plastic model. This model shade light on the interaction between plasticity and crack propagation in ductile materials (Section 4.1). The investigation is supported by the experimental study on busbars (Section 2.1). This constitutive model is characterized in terms of CZM peak stress ($\sigma_{\max}$), critical opening (g_c) and initial stiffness (K). The use of the PSO algorithm allow to identify the parameters which best fit the experimental results. For this identification two kind of CZM are considered and compared: the Tvergaard model and the bilinear model. We obtain a good agreement between experimental and numerical curves in both cases. The Tvergaard model achieve a bet-

ter fitting of the 0.45 mm notch experiment. On the contrary, the bilinear model achieve a better fitting of the 0.8 mm notch experiment. Moreover, for the bilinear model is identified an optimal critical opening $g_c = 0.07$ mm. This value is physically more meaningful with respect to the value obtained using the Tvergaard model (g_c = 0.19 mm). The comparison with the experimental SEM images (Fig. 7) gives a discrepancy of one order of magnitude between the experimental and the numerical critical opening. Based on the arguments herein outlined, such discrepancy can be addressed to a diffusive nature of the fracture. With the CZM we confine the damage phenomena in the middle line of the specimen. Then, the high value of g_c could take also into account the damage developed in the surrounding area around the middle line.

Another problem at the micro level is faced making use of the PF model. In Section 4.2 the adhesive wear phenomenon is investigated simulating the fracture of idealized asperities of two surfaces in contact. We identify two failure modes from the parametric analysis and from the study of the asperities' singularity. The responsible of the crack nucleation is identified in the Mode II stress intensification around the asperity's geometry corners. The competition between crack nucleation at the base corners of the asperity or at the contact corners is gained by the corner which generates a Mode II stress singularity. The Mode II stress singularity is predicted to occurs when the total amplitude of the corner 2γ is smaller than $51°$. On the other side, the asperity crack propagation angle γ' is related with the possibility of predicting a steady state wear. It is found that the steady state wear is more likely to occur for an asperity slope of $\gamma = 45°$.

The predictive capabilities of the two fracture computational models (PF and CZM) adopted in the previous applications are exploited coupling them together at the constitutive level (Section 3.2.1). The coupling between the two models lay on the hypothesis that the increasing amount of damage $\mathfrak{d}$ at the surrounding bulk reduce the CZM stiffness. In this way many complex crack paths in composite materials are reproduced. This computational model is used for the investigation and the characterization of the fracture behaviour in composite laminated ma-

terials. The general behaviour of crack propagation and delamination interaction is investigated by means of a notched tensile test of laminate with layers perpendicular to the notch. This test is used as benchmark to investigate the effects of the variation of the interface parameters keeping constant the bulk material properties. Then, effects of tough and brittle interfaces are compared with the case of fully bounded layers. We find that the introduction of an interface makes the crack path more tortuous and involve a larger part of the specimen length. It is also identified that for this problem the peak stress of the CZM governs the development of crack penetration, crack branching and crack deflection phenomena.

Considering the general understanding of the problem that is acquired from these benchmark tests, the computational model is applied for the characterization of real laminates structures. The Si_3N_4/BN laminate is characterized identifying the Si_3N_4 fracture energy and the traction-separation law of the BN interfaces. The identification is performed simulating the experimental 4-point bending test. The crack pattern and the force-displacement curve of the experiment are reproduced with good agreement using a very weak BN interface.

Another application of the coupled PF and CZM framework is the characterization of the Al/SiC nanolaminate. The simulations concerns the experimental results described in Section 2.2. The PF model gives to the numerical predictions the nonlinear behaviour encountered in the Al layers during the experiments. Even though the origin of the nonlinear behaviour cannot be precisely defined, we suppose that it is generated by a diffuse damage. Then, the peak stress of the CZM is matched with the experimental peak tensile stress, finding the values of $\sigma_{\max} = 1.6$ GPa for the case of 50 nm layers and $\sigma_{\max} = 1.4$ GPa for the case of 100 nm layers. Another important result is given by the particular fracture pattern that the 50 nm layers simulation is able to reproduce.

The complex crack patterns developed in the simulations herein described, demonstrate the suitability of coupled PF and CZM framework for the study of fracture in laminates. The main advantages of this model is that the Griffith fracture criterion is inherently adopted in the PF model. Then, the implementation of a crack tracking algorithm or the

computations of the stress in the regions close to cracks are avoided. Moreover, there is no necessity to use a remeshing algorithm during the simulation like in other models (XFEM or SDA). This implicate a great reduction of computational time.

In order to study more complex laminate structures, the coupled PF and CZM modelling framework is enhanced from the bi-dimensional to the three-dimensional space (Sections 3.1.3 and 3.2.2). The PF model is enclosed in a 3D solid shell formulation, while the CZM is extended to a 3D interface element. Both formulations are coupled at the constitutive level and are enclosed in a finite elasticity formulation. Several numerical examples, concerning the crack propagation in a flat geometry, in a flat and curved sandwich panel and in a PV solar panel, are used to validate the proposed computational model. The model shows its powerful ability to simulate complex crack phenomena in 3D composite structures. The interaction between intralayer crack propagation and interlayer delamination can be captured including patterns with concurrent delamination and crack propagation. Moreover, the potentialities of the solid shell formulation can be exploited by simulating curved geometries and/or out-of-plane loading. The model herein presented fosters new possibilities for the three-dimensional simulation of failure in composite materials. In this concern, it has been shown that the proposed numerical framework opens new possibilities with regard to the accurate stress analysis in composite photovoltaic modules and the simulation of material-related failures related to brittle cracking in Silicon or backsheet delamination due to cohesion failure of the encapsulant material.

6.1 Future developments

The first development of this dissertation will be a more complete characterization of the Al/SiC nanolaminate. In Section 5.1.3 the peak stress of the interfaces is characterized by means of the coupled PF and CZM modelling framework. The fracture characterization of the two constituent materials will be performed using the same modelling framework and applying it to other nanoindentation test already performed in lit-

erature (Section 2.2). For instance, from the numerical simulation of the shear test proposed in [69], it can be identify the fracture energy of the Al. In this experiment the layers of the nanolaminate were parallel to the loading direction (Figs. 12(a),(b)). The failure of the specimen was found to occur among the middle Al layer and the two neighbour interfaces. Then, the reproduction of this crack pattern together with the fitting of the force-displacement curve will provide a good approximation of the Al fracture energy (Figs. 74(a),(b)). Once the fracture energy is identified, the simulation of the cantilever test experiments performed in [70] (Fig. 74(c),(d)) can provide information for the identification of the SiC fracture energy. In this case the experimental campaign is more significant and experimental data regarding various layer orientation and thickness are available. Consequently, fitting the force-displacement curves retrieved from the tensile and shear tests, will provide the overall fracture characterization of the nanolaminate.

A further validation of the fracture parameters retrieved from the previous approach will be performed by means of the identification procedure proposed in [63]. The procedure is based on the results of the micropillar splitting test (Fig. 11). A 3D computational model is built to reproduce the experiments. Taking advantage of the symmetric geometry and boundary conditions, the computational model consider one-sixth of the total domain (Fig. 75(a)). Symmetric boundary conditions were applied on both lateral surface of the simulated domain. One of the two lateral surfaces is equipped with a plane made of 3D interface elements. This plane has the objective of reproducinf the fracture propagation in the splitting test. In this investigation the specimen was made of one homogeneous material. The bulk material has been considered elastoplastic and 3D brick elements has been used. The indenter was modelled with a contact between the pillar and a rigid body with the Berkovich tip shape. The comparison between the numerical and the experimental force-displacement curve allow the identification of the fracture parameters of the model. Taking this procedure as starting point, the computational model will be enhanced in order to simulate the splitting test of the Al/SiC nanolaminate. The 3D solid shell with PF formulation together

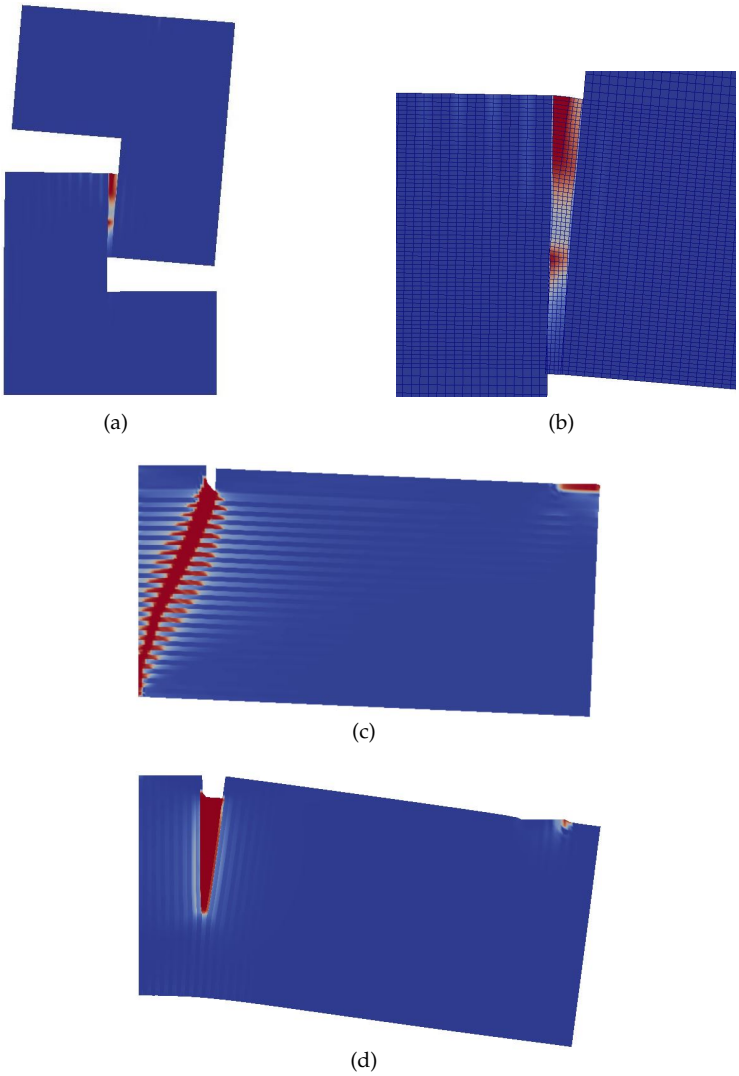

Figure 74: Simulation of nanoindentation tests for the characterization of the Al/SiC nanolaminate. (a) shear test simulation with layers parallel to the loading direction; (b) particular of the failure of the Al middle layer; (c) cantilever test simulation with layers perpendicular to the loading direction; (d) cantilever test simulation with layers parallel to the loading direction;

with the 3D interface elements will be used to reproduce the experimental tests available in literature (Fig. 75(b)). The 3D shell element will be used to model evry layer with its mechanical and fracture properties. The interface elements will be used for modelling the interfaces between layers. With this computational model, the geometry of the specimen to consider is one-third with symmetric boundary conditions. This procedure can provide a more precise characterization of the Al/SiC nanolaminate. In fact, phenomena like crack branching or deflection will be fully captured.

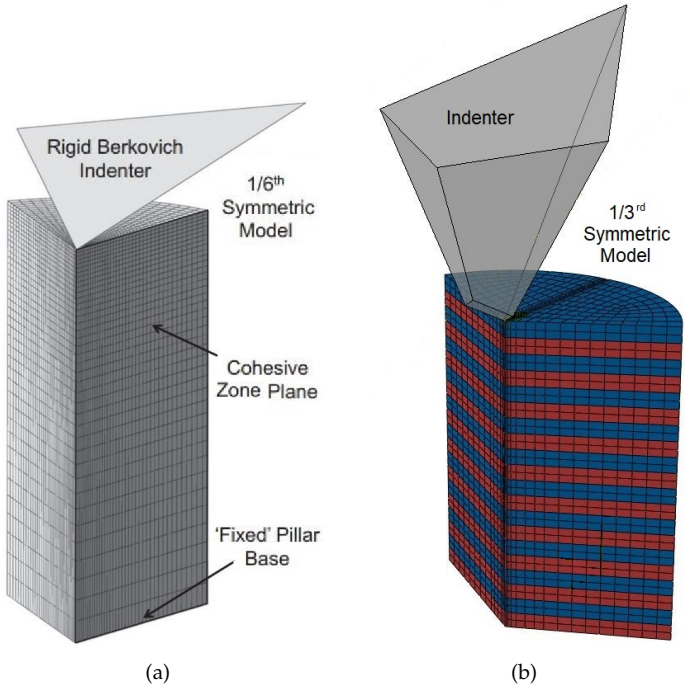

Figure 75: Computational model of the pillar splitting test. (a) model proposed in [63]; (b) model based on the 3D solid shell and 3D interface elements herein proposed. Image (a) With permission from [63].

The computation framework herein described and developed can be

used to explore many others applications. It can be studied other composite structures such as fibre reinforced composites or composite materials made of aggregates. Other applications could be found in the civil engineering field, studying the behaviour of masonries or reinforced concrete structures. All these applications share the problem of combining heterogeneous components separated by interfaces.

Aside the field of the applications, the computational model itself will be enhanced extending the formulation to the dynamic field. Many author have already developed a dynamic formulation of the PF model [140] and of the CZM [141]. Then, in the spirit of the coupling hypothesis described in Section 3.2.1, the two dynamical models will be coupled. In particular, the dynamic formulation will be based on the following Lagrangian functional L:

$$L = K - \Pi, \tag{6.1}$$

where Π is the potential energy functional defined in Eq. (3.49) and K is the kinetic energy of the coupled problem defined as:

$$K = \frac{1}{2}\int_{\Omega} \rho \dot{\mathbf{u}} \cdot \dot{\mathbf{u}} dV + \int_{\Gamma_i} \rho_i \dot{\mathbf{u}} \cdot \dot{\mathbf{u}} d\Gamma, \tag{6.2}$$

where ρ and ρ_i are, respectively, the density mass of the bulk and the interface, and $\dot{\mathbf{u}}$ is the velocity vector.

After the computation of the weak form of the variational problem of the functional (6.1), and after the linearization and the finite element formulation, the resulting linearized system of equation will reads:

$$\mathbf{M}\ddot{\mathbf{u}} + \mathbf{K}\mathbf{u} = \mathbf{F}^{\text{ext}} + \mathbf{F}^{\text{d}}, \tag{6.3}$$

where $\mathbf{M}$ is the mass matrix, $\ddot{\mathbf{u}}$ is the acceleration vector, $\mathbf{K}$ is the stiffness matrix, $\mathbf{F}^{\text{ext}}$ is the external force vector and $\mathbf{F}^{\text{d}}$ is the dynamic force vector. Making use of a lumped formulation, the mass matrix $\mathbf{M}$ will read:

$$\mathbf{M} = \mathbf{M}_b + \mathbf{M}_i = \left(N_{\text{n}} \frac{1}{n} \rho t \|\mathbf{J}\| + N_{\text{n}} \frac{1}{n} \rho t_i l \right) \mathbf{I}, \tag{6.4}$$

where $\mathbf{M}_b$ and $\mathbf{M}_i$ are, respectively, the mass matrix of the bulk and the interface element, N_{n} is a coefficient determined by the solution strategy of the dynamical simulation, n is the number of nodes of the element, t is the thickness of the bulk element, **J** is the Jacobian matrix, t_i and l are, respectively, the thickness and the length of the interface element and **I** is the identity matrix. The dynamic force vector $\mathbf{F}^{\mathrm{d}}$, which depend only on the bulk, will read:

$$\mathbf{F}^{\mathrm{d}} = \frac{1}{n}\rho t \|\mathbf{J}\| \ddot{\mathbf{u}}. \tag{6.5}$$

According to this formulations the dynamic interaction between crack propagation and delamination will be studied. For instance, in [142] a dynamic crack propagation experiment has been performed. It was considered the impact of a projectile against a borosilicate glass with a pre-existing interface. It was found that increasing the interface thickness the crack branching phenomenon is more relevant (Fig. 76). The reproduction of this experiments in the spirit of the dynamical computational model, will shed light on the phenomenon of crack branching due to the dynamic interaction between crack propagation and interfaces.

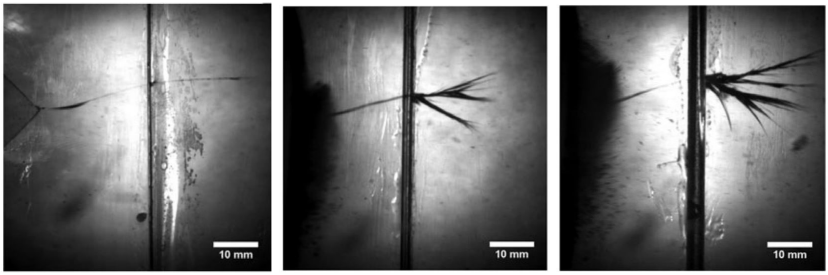

(a) (b) (c)

Figure 76: Experimental study performed in [142]. The influence of the interface thickness in the dynamic crack propagation is studied. Interface thickness of: (a) 0.2 mm; (b) 1.0 mm; (c) 2.7 mm. With permission from [142].

References

[1] T.J. Chuang and J.W. Rudnicki. *Multiscale deformation and fracture in materials and structures: the James R. Rice 60th anniversary volume*, volume 84. Springer Science & Business Media, 2001. 1

[2] C.E. Inglis. Stresses in a plate due to the presence of cracks and sharp corners. *Transactions of the institute of naval architects*, 55(219-241):193–198, 1913. 2

[3] A.A. Griffith. The phenomena of rupture and flow in solids. *Philosophical transactions of the royal society of london. Series A, containing papers of a mathematical or physical character*, 221:163–198, 1921. 2

[4] I. Sneddon. The distribution of stress in the neighbourhood of a crack in an elastic solid. In *Proceedings of the Royal Society of London A: Mathematical, Physical and Engineering Sciences*, volume 187, pages 229–260. The Royal Society, 1946. 2

[5] M.L. Williams. On the stress distribution at the base of a stationary crack. 1997. 2

[6] G.R. Irwin. Analysis of stresses and strains near the end of a crack traversing a plate. *Journal of applied mechanics*, 24(3):361–364, 1957. 2

[7] F. Ziegler. Bruch-und beurteilungskriterien in der festigungslehre. leipzig, fachbuchverlag 1989. 334 s., 220 bilder, 40 tab., dm 40,-. isbn 3–343–00245–3. *ZAMM-Journal of Applied Mathematics and Mechanics/Zeitschrift für Angewandte Mathematik und Mechanik*, 71(3):201–201, 1991. 3

[8] G.R. Irwin. Onset of fast crack propagation in high strength steel and aluminum alloys. Technical report, NAVAL RESEARCH LAB WASHINGTON DC, 1956. 3

[9] D.S. Dugdale. Yielding of steel sheets containing slits. *Journal of the Mechanics and Physics of Solids*, 8(2):100–104, 1960. 4

[10] O.C. Zienkiewicz and R.L. Taylor. *The finite element method: solid mechanics*, volume 2. Butterworth-heinemann, 2000. 5, 92, 111

[11] A. Salvadori L.J. Gray L. Távara, V. Mantič and Federico F. París. Cohesive-zone-model formulation and implementation using the symmetric galerkin boundary element method for homogeneous solids. *Computational Mechanics*, pages 1–17, 2013. 5

[12] A. Blázquez E. Graciani V. Mantič, L. Távara and F. París. A linear elastic-brittle interface model: application for the onset and propagation of a fibre-matrix interface crack under biaxial transverse loads. *International Journal of Fracture*, 195(1-2):15–38, 2015. 5

[13] J. Dolbow N. Moës and T. Belytschko. A finite element method for crack growth without remeshing. *International journal for numerical methods in engineering*, 46(1):131–150, 1999. 5

[14] T.P. Fries and T. Belytschko. The extended/generalized finite element method: an overview of the method and its applications. *International Journal for Numerical Methods in Engineering*, 84(3):253–304, 2010. 5

[15] A. Carpinteri P. Cornetti, N. Pugno and D. Taylor. Finite fracture mechanics: a coupled stress and energy failure criterion. *Engineering Fracture Mechanics*, 73(14):2021–2033, 2006. 5

[16] J. Oliver J.C. Simo and F. Armero. An analysis of strong discontinuities induced by strain-softening in rate-independent inelastic solids. *Computational mechanics*, 12(5):277–296, 1993. 5

[17] S. Blanco J. Oliver, A.E. Huespe and D.L. Linero. Stability and robustness issues in numerical modeling of material failure with the strong discontinuity approach. *Computer Methods in Applied Mechanics and Engineering*, 195(52):7093–7114, 2006. 5

[18] C. Linder and F. Armero. Finite elements with embedded strong discontinuities for the modeling of failure in solids. *International Journal for Numerical Methods in Engineering*, 72(12):1391–1433, 2007. 5

[19] X.P. Xu and A. Needleman. Numerical simulations of fast crack growth in brittle solids. *Journal of the Mechanics and Physics of Solids*, 42(9):1397–1434, 1994. 5

[20] M. Ortiz and A. Pandolfi. Finite deformation irreversible cohesive elements for three-dimensional crack-propagation analysis. *International Journal for Numerical Methods in Engineering*, 44:1267–1282, 1999. 5

[21] M. Paggi and P. Wriggers. Stiffness and strength of hierarchical polycrystalline materials with imperfect interfaces. *Journal of the Mechanics and Physics of Solids*, 60(4):557–572, 2012. 5, 50

[22] M. Corrado and J.F. Molinari. Effects of residual stresses on the tensile fatigue behavior of concrete. *Cement and Concrete Research*, 89:206–219, 2016. 5

[23] D. Krajcinovic V.A. Lubarda and S. Mastilovic. Damage model for brittle elastic solids with unequal tensile and compressive strengths. *Engineering Fracture Mechanics*, 49(5):681–697, 1994. 5

[24] M. Jirásek. Nonlocal models for damage and fracture: comparison of approaches. *International Journal of Solids and Structures*, 35(31-32):4133–4145, 1998. 5

[25] M. Frmond and B. Nedjar. Damage, gradient of damage and principle of virtual power. *International Journal of Solids and Structures*, 33(8):1083 – 1103, 1996. 5

[26] R. De Borst R.H.J. Peerlings, M.G.D. Geers and W.A.M. Brekelmans. A critical comparison of nonlocal and gradient-enhanced softening continua. *International Journal of solids and Structures*, 38(44):7723–7746, 2001. 5

[27] C. Comi. Computational modelling of gradient-enhanced damage in quasi-brittle materials. *Mechanics of Cohesive-frictional Materials*, 4(1):17–36, 1999. 5

[28] C. Comi and U. Perego. Fracture energy based bi-dissipative damage model for concrete. *International journal of solids and structures*, 38(36):6427–6454, 2001. 5

[29] B.J. Dimitrijevic and K. Hackl. A regularization framework for damage–plasticity models via gradient enhancement of the free energy. *International Journal for Numerical Methods in Biomedical Engineering*, 27(8):1199–1210, 2011. 5

[30] P.E. Bernard N. Moës, C. Stolz and N. Chevaugeon. A level set based model for damage growth: the thick level set approach. *International Journal for Numerical Methods in Engineering*, 86(3):358–380, 2011. 5

[31] N. Moës P.E. Bernard and N. Chevaugeon. Damage growth modeling using the thick level set (tls) approach: Efficient discretization for quasi-static loadings. *Computer Methods in Applied Mechanics and Engineering*, 233:11–27, 2012. 5

[32] G.A. Francfort B. Bourdin and J.J. Marigo. The variational approach to fracture. *Journal of elasticity*, 91(1):5–148, 2008. 5

[33] L. Ambrosio and V.M. Tortorelli. Approximation of functional depending on jumps by elliptic functional via t-convergence. *Communications on Pure and Applied Mathematics*, 43(8):999–1036, 1990. 6

[34] G.A. Francfort and J.J. Marigo. Revisiting brittle fracture as an energy minimization problem. *Journal of the Mechanics and Physics of Solids*, 46(8):1319–1342, 1998. 6

[35] J.J. Marigo H. Amor and C. Maurini. Regularized formulation of the variational brittle fracture with unilateral contact: numerical experiments. *Journal of the Mechanics and Physics of Solids*, 57(8):1209–1229, 2009. 6

[36] M. Hofacker C. Miehe and F. Welschinger. A phase field model for rate-independent crack propagation: Robust algorithmic implementation based on operator splits. *Computer Methods in Applied Mechanics and Engineering*, 199(45):2765–2778, 2010. 6, 32

[37] F. Welschinger C. Miehe and M. Hofacker. Thermodynamically consistent phase-field models of fracture: Variational principles and multi-field fe implementations. *International Journal for Numerical Methods in Engineering*, 83(10):1273–1311, 2010. 6

[38] M. Hofacker and C. Miehe. A phase field model of dynamic fracture: Robust field updates for the analysis of complex crack patterns. *International Journal for Numerical Methods in Engineering*, 93(3):276–301, 2013. 6

[39] M.A. Scott T.J.R Hughes M.J. Borden, C.V. Verhoosel and C.M. Landis. A phase-field description of dynamic brittle fracture. *Computer Methods in Applied Mechanics and Engineering*, 217:77–95, 2012. 6

[40] T. Gerasimov M. Ambati and L. De Lorenzis. Phase-field modeling of ductile fracture. *Computational Mechanics*, 55(5):1017–1040, 2015. 6, 35

[41] M. Arroyo M. Silani F. Amiri, D. Millán and T. Rabczuk. Fourth order phase-field model for local max-ent approximants applied to crack propagation. *Computer Methods in Applied Mechanics and Engineering*, 312:254–275, 2016. 6

[42] L.M. Schänzel C. Miehe and H. Ulmer. Phase field modeling of fracture in multi-physics problems. part i. balance of crack surface and failure criteria for brittle crack propagation in thermo-elastic solids. *Computer Methods in Applied Mechanics and Engineering*, 294:449–485, 2015. 6

[43] L.M. Schaenzel C. Miehe, M. Hofacker and F. Aldakheel. Phase field modeling of fracture in multi-physics problems. part ii. coupled brittle-to-ductile failure criteria and crack propagation in thermo-elastic–plastic solids. *Computer Methods in Applied Mechanics and Engineering*, 294:486–522, 2015. 6

[44] A. Krischok X. Zhang and C. Linder. A variational framework to model diffusion induced large plastic deformation and phase field fracture during initial two-phase lithiation of silicon electrodes. *Computer Methods in Applied Mechanics and Engineering*, 312:51–77, 2016. 6

[45] Y. Shen T. Rabczuk F. Amiri, D. Millán and M. Arroyo. Phase-field modeling of fracture in linear thin shells. *Theoretical and Applied Fracture Mechanics*, 69:102–109, 2014. 6

[46] T. Rabczuk P. Areias and M.A. Msekh. Phase-field analysis of finite-strain plates and shells including element subdivision. *Computer Methods in Applied Mechanics and Engineering*, 312:322–350, 2016. 6

[47] M. Ambati and L. De Lorenzis. Phase-field modeling of brittle and ductile fracture in shells with isogeometric nurbs-based solid-shell elements. *Computer Methods in Applied Mechanics and Engineering*, 312:351–373, 2016. 6

[48] L. De Lorenzis H. Gomez J. Kiendl, M. Ambati and A. Reali. Phase-field description of brittle fracture in plates and shells. *Computer Methods in Applied Mechanics and Engineering*, 312:374–394, 2016. 6

[49] M. Paggi J. Reinoso and C. Linder. Phase field modeling of brittle fracture for enhanced assumed strain shells at large deformations: formulation and finite element implementation. *Computational Mechanics*, pages 1–21, 2017. 6, 40, 41, 42

[50] Q.-Z. Zhu M. Bornert T.-T. Nguyen, J. Yvonnet and C. Chateau. A phase-field method for computational modeling of interfacial damage interacting with crack propagation in realistic microstructures obtained by microtomography. *Computer Methods in Applied Mechanics and Engineering*, 312:567–595, 2016. 6, 35

[51] M. Bornert T.-T. Nguyen, J. Yvonnet and C. Chateau. Initiation and propagation of complex 3d networks of cracks in heterogeneous quasi-brittle materials: direct comparison between in situ testing-microct experiments and phase field simulations. *Journal of the Mechanics and Physics of Solids*, 95:320–350, 2016. 6, 35

[52] M. Paggi and J. Reinoso. Revisiting the problem of a crack impinging on an interface: a modeling framework for the interaction between the phase field approach for brittle fracture and the interface cohesive zone model. *Computer Methods in Applied Mechanics and Engineering*, 2017. 6, 58, 59

[53] I. Kunze M. Köntges, S. Kajari-Schröder and U. Jahn. Crack statistic of crystalline silicon photovoltaic modules. In *26th European Photovoltaic Solar Energy Conference and Exhibition*, pages 5–6, 2011. 10

[54] A. Infuso M. Paggi, I. Berardone and M. Corrado. Fatigue degradation and electric recovery in silicon solar cells embedded in photovoltaic modules. *Scientific reports*, 4, 2014. ix, 10, 11

[55] M. Pander M. Ebert M. Sander, S. Dietrich and J. Bagdahn. Systematic investigation of cracks in encapsulated solar cells after mechanical loading. *Solar Energy Materials and Solar Cells*, 111:82–89, 2013. 10, 125

[56] S. Kajari-Schröder M. Paggi and U. Eitner. Thermomechanical deformations in photovoltaic laminates. *The Journal of Strain Analysis for Engineering Design*, 46(8):772–782, 2011. 10

[57] Y.L. Shen G. Tang N. Chawla, D.R.P. Singh and K.K. Chawla. Indentation mechanics and fracture behavior of metal/ceramic nanolaminate composites. *Journal of Materials Science*, 43(13):4383–4390, 2008. 16

[58] P. Dickerson R.G. Hoagland N.A. Mara, D. Bhattacharyya and A. Misra. Deformability of ultrahigh strength 5 nm cu/ nb nanolayered composites. *Applied Physics Letters*, 92(23):231901, 2008. 16

[59] T.S. Lee M.K. Chung B. Cheong J.H. Lee, W.M. Kim and S.G. Kim. Mechanical and adhesion properties of al/aln multilayered thin films. *Surface and Coatings Technology*, 133:220–226, 2000. 16

[60] J.S. Carpenter T. Nizolek W.M. Mook T.A. Wynn R.J. McCabe J.R. Mayeur K. Kang S. Zheng I.J. Beyerlein, N.A. Mara et al. Interface-driven microstructure development and ultra high strength of bulk nanostructured cu-nb multilayers fabricated by severe plastic deformation. *Journal of materials research*, 28(13):1799–1812, 2013. 16

[61] P. Dickerson R.G. Hoagland D. Bhattacharyya, N.A. Mara and A. Misra. Compressive flow behavior of al–tin multilayers at nanometer scale layer thickness. *Acta Materialia*, 59(10):3804–3816, 2011. 16

[62] J.K. Baldwin N.A. Mara A. Misra Amit Y. Kim, A.S. Budiman and S.M. Han. Microcompression study of al-nb nanoscale multilayers. *Journal of Materials Research*, 27(3):592–598, 2012. 16

[63] E.G. Herbert F. Carassiti M. Sebastiani, K.E. Johanns and George Mathews G.M. Pharr. A novel pillar indentation splitting test for measuring fracture toughness of thin ceramic coatings. *Philosophical Magazine*, 95(16-18):1928–1944, 2015. x, xv, 16, 18, 19, 92, 133, 135

[64] A. Misra N. Li, H. Wang and J. Wang. In situ nanoindentation study of plastic co-deformation in al-tin nanocomposites. *Scientific reports*, 4, 2014. 16, 92

[65] P.J. Kelly and R.D. Arnell. Magnetron sputtering: a review of recent developments and applications. *Vacuum*, 56(3):159–172, 2000. 17

[66] S.S. Singh H. Xie Y.L. Shen J. Llorca J. Molina-Aldareguia C. Mayer, L.W. Yang and N. Chawla. Orientation dependence of indentation behavior in al–sic nanolaminate composites. *Materials Letters*, 168:129–133, 2016. ix, 17

[67] A.C. Fischer-Cripps. *Factors Affecting Nanoindentation Test Data*. Springer, 2000. 17, 18

[68] K.E. Yazzie N. Chawla J. Llorca S. Lotfian, M. Rodríguez and J. Molina-Aldareguía. High temperature micropillar compression of al/sic nanolaminates. *Acta Materialia*, 61(12):4439–4451, 2013. x, 18, 19

[69] N. Mara C. Mayer, N. Li and N. Chawla. Micromechanical and in situ shear testing of al–sic nanolaminate composites in a transmission electron microscope (tem). *Materials Science and Engineering: A*, 621:229–235, 2015. x, 18, 20, 133

[70] C.R. Mayer. *Mechanical Behavior of Al-SiC Nanolaminate Composites Using Micro-Scale Testing Methods*. Arizona State University, 2016. x, 20, 133

[71] Karlsson Hibbitt and Sorensen. *ABAQUS/standard User's Manual*, volume 1. Hibbitt, Karlsson & Sorensen, 2001. 24

[72] A. Braides. *Approximation of free-discontinuity problems*. Number 1694. Springer Science & Business Media, 1998. 29, 93

[73] M. Hofacker C. Miehe and F. Welschinger. A phase field model for rate-independent crack propagation: Robust algorithmic implementation based on operator splits. *Computer Methods in Applied Mechanics and Engineering*, 199(45):2765–2778, 2010. 29, 30

[74] F. Welschinger C. Miehe and M. Hofacker. Thermodynamically consistent phase-field models of fracture: Variational principles and multi-field fe implementations. *International Journal for Numerical Methods in Engineering*, 83(10):1273–1311, 2010. 29, 30

[75] G.A. Francfort B. Bourdin and J.J. Marigo. The variational approach to fracture. *Journal of elasticity*, 91(1):5–148, 2008. 30

[76] D. Krajcinovic V.A. Lubarda and S. Mastilovic. Damage model for brittle elastic solids with unequal tensile and compressive strengths. *Engineering Fracture Mechanics*, 49(5):681–697, 1994. 32

[77] M. Jamshidian P.M. Areias M.-A. Msekh, J.-M. Sargado and T. Rabczuk. Abaqus implementation of phase-field model for brittle fracture. *Computational Materials Science*, 96:472–484, 2015. 35, 37

[78] M. Bischoff and E. Ramm. Shear deformable shell elements for large strains and rotations. *International Journal for Numerical Methods in Engineering*, 40(23):4427–4449, 1997. 36, 42

[79] S. Klinkel and W. Wagner. A geometrical non-linear brick element based on the eas-method. *International Journal for Numerical Methods in Engineering*, 40(24):4529–4545, 1997. 36

[80] J.C. Simo and F. Armero. Geometrically non-linear enhanced strain mixed methods and the method of incompatible modes. *International Journal for Numerical Methods in Engineering*, 33(7):1413–1449, 1992. 38

[81] L. Vu-Quoc and X.G. Tan. Optimal solid shells for non-linear analyses of multilayer composites. i. statics. *Computer Methods in Applied Mechanics and Engineering*, 192(910):975 – 1016, 2003. 40

[82] C. Miehe. A theoretical and computational model for isotropic elastoplastic stress analysis in shells at large strains. *Computer Methods in Applied Mechanics and Engineering*, 155(3-4):193–233, 1998. 40

[83] A.M. Habraken J. Degrieck R.J.A. de Sousa K. Rah, W.V. Paepegem and R.A.F. Valente. Optimal low-order fully integrated solid-shell elements. *Computational Mechanics*, 51(3):309–326, 2013. 42

[84] F. Gruttmann S. Klinkel and W. Wagner. A continuum based three-dimensional shell element for laminated structures. *Computers & Structures*, 71(1):43–62, 1999. 42

[85] A.M. Waas J.A. Schroeder S. Li, M.D. Thouless and P.D. Zavattieri. Use of mode-i cohesive-zone models to describe the fracture of an adhesively-bonded polymer-matrix composite. *Composites Science and Technology*, 65(2):281–293, 2005. xi, 43

[86] G.I. Barenblatt. The mathematical theory of equilibrium cracks in brittle fracture. *Advances in applied mechanics*, 7:55–129, 1962. 43

[87] A. Needleman. A continuum model for void nucleation by inclusion debonding. *Journal of applied mechanics*, 54(3):525–531, 1987. 44

[88] A. Needleman. An analysis of tensile decohesion along an interface. *Journal of the Mechanics and Physics of Solids*, 38(3):289–324, 1990. 44

[89] V. Tvergaard and J.W. Hutchinson. The relation between crack growth resistance and fracture process parameters in elastic-plastic solids. *Journal of the Mechanics and Physics of Solids*, 40(6):1377–1397, 1992. 44

[90] P.H. Geubelle and J.S. Baylor. Impact-induced delamination of composites: a 2d simulation. *Composites Part B: Engineering*, 29(5):589–602, 1998. 44, 62

[91] R. Fedele G. Bolzon and G. Maier. Parameter identification of a cohesive crack model by kalman filter. *Computer Methods in Applied Mechanics and Engineering*, 191(25):2847–2871, 2002. 44

[92] M. Paggi and P. Wriggers. A nonlocal cohesive zone model for finite thickness interfaces–part i: mathematical formulation and validation with molecular dynamics. *Computational Materials Science*, 50(5):1625–1633, 2011. 44

[93] N. Valoroso and R. Fedele. Characterization of a cohesive-zone model describing damage and de-cohesion at bonded interfaces. sensitivity analysis and mode-i parameter identification. *International Journal of Solids and Structures*, 47(13):1666–1677, 2010. 44

[94] S. Basu C.K. Desai, A.S. Kumar and V. Parameswaran. Measurement of cohesive parameters of crazes in polystyrene films. In *Experimental and Applied Mechanics, Volume 6*, pages 519–526. Springer, 2011. 45

[95] C.V. Verhoosel and R. Borst. A phase-field model for cohesive fracture. *International Journal for numerical methods in Engineering*, 96(1):43–62, 2013. 47

[96] J.G. Williams and H. Hadavinia. Analytical solutions for cohesive zone models. *Journal of the Mechanics and Physics of Solids*, 50(4):809–825, 2002. 47

[97] M. Paggi and J. Reinoso. Revisiting the problem of a crack impinging on an interface: a modeling framework for the interaction between the phase field approach for brittle fracture and the interface cohesive zone model. *Computer Methods in Applied Mechanics and Engineering*, 321:145–172, 2017. xii, xiii, 47, 80, 89, 90, 91, 101

[98] A.G. Evans P.G. Charalambides, J. Lund and R.M. McMeeking. A test specimen for determining the fracture resistance of bimaterial interfaces. *Journal of applied mechanics*, 56(1):77–82, 1989. 48

[99] C.G. Davila P.P. Camanho and M.F. De Moura. Numerical simulation of mixed-mode progressive delamination in composite materials. *Journal of composite materials*, 37(16):1415–1438, 2003. 48, 89

[100] M. Paggi and J. Reinoso. An anisotropic large displacement cohesive zone model for fibrillar and crazing interfaces. *International Journal of Solids and Structures*, 69:106–120, 2015. 50, 51, 59

[101] J. Reinoso and M. Paggi. A consistent interface element formulation for geometrical and material nonlinearities. *Computational Mechanics*, 54(6):1569–1581, 2014. 51, 58, 59

[102] M. Paggi and P. Wriggers. A nonlocal cohesive zone model for finite thickness interfaces–part i: mathematical formulation and validation with molecular dynamics. *Computational Materials Science*, 50(5):1625–1633, 2011. 58

[103] M. Paggi and P. Wriggers. A nonlocal cohesive zone model for finite thickness interfaces–part ii: Fe implementation and application to polycrystalline materials. *Computational Materials Science*, 50(5):1634–1643, 2011. 58

[104] Francesco Parrinello, Guido Borino, and Roberto Caserta. Effective reference and current integration for large displacement interface. *GIMC-GMA Conference*, 2016. 58

[105] V. Tvergaard. Effect of fibre debonding in a whisker-reinforced metal. *Materials science and engineering: A*, 125(2):203–213, 1990. 62

[106] S. Boyd and L. Vandenberghe. *Convex optimization*. Cambridge university press, 2004. 66

[107] M. Clerc. *Particle swarm optimization*, volume 93. John Wiley & Sons, 2010. 66

[108] E. Rabinowicz and R.I. Tanner. Friction and wear of materials. *Journal of Applied Mechanics*, 33:479, 1966. 77

[109] G. Stachowiak and A.W. Batchelor. *Engineering tribology*. Butterworth-Heinemann, 2013. xii, 77, 79

[110] B. Bhushan. *Modern tribology handbook, two volume set*. CRC press, 2000. 77

[111] J.M. Ziman. Electrons in metals: A short guide to the fermi surface. *Contemporary Physics*, 4(2):81–99, 1962. 77

[112] R. Holm. *Electric contacts: theory and application*. Springer Science & Business Media, 2013. 77

[113] J Archard. Contact and rubbing of flat surfaces. *Journal of applied physics*, 24(8):981–988, 1953. 77

[114] K.T. Turner V. Vahdat, D.S. Grierson and R.W. Carpick. Mechanics of interaction and atomic-scale wear of amplitude modulation atomic force microscopy probes. *ACS nano*, 7(4):3221–3235, 2013. 78

[115] B. Gotsmann M.A. Lantz. Atomistic wear in a single asperity sliding contact. *Physical review letters*, 101(12):125501, 2008. 78

[116] D.H. Warner R. Aghababaei and J.F. Molinari. Critical length scale controls adhesive wear mechanisms. *Nature communications*, 7, 2016. 78

[117] R. Shakiba J. Zhong and J.B. Adams. Molecular dynamics simulation of severe adhesive wear on a rough aluminum substrate. *Journal of Physics D: Applied Physics*, 46(5):055307, 2013. 78

[118] K.-H. Chung and K. Dae-Eun. Fundamental investigation of micro wear rate using an atomic force microscope. *Tribology Letters*, 15(2):135–144, 2003. 78

[119] J.A. Greenwood and D. Tabor. Deformation properties of friction junctions. *Proceedings of the Physical Society. Section B*, 68(9):609, 1955. 78

[120] C.A. Brockley and G.K. Fleming. A model junction study of severe metallic wear. *Wear*, 8(5):374–380, 1965. 78, 79

[121] D.H. Buckley. *Surface effects in adhesion, friction, wear, and lubrication*, volume 5. Elsevier, 1981. 78

[122] T. Kayaba and K. Kato. The analysis of adhesive wear mechanism by successive observations of the wear process in sem. *Wear of Materials*, pages 45–56, 1979. 78

[123] D.A. Hills A. Mugadu and D. Nowell. Modifications to a fretting-fatigue testing apparatus based upon an analysis of contact stresses at complete and nearly complete contacts. *Wear*, 252(5):475–483, 2002. 80

[124] M.I. Porter and D.A. Hills. Note on the complete contact between a flat rigid punch and an elastic layer attached to a dissimilar substrate. *International journal of mechanical sciences*, 44(3):509–520, 2002. 80

[125] D.A. Hills A. Mugadu and L. Limmer. An asymptotic approach to crack initiation in fretting fatigue of complete contacts. *Journal of the Mechanics and Physics of Solids*, 50(3):531–547, 2002. 80

[126] M.L. Williams. Stress singularities resulting from various boundary conditions in angular corners of plates in extension. *Journal of applied mechanics*, 19(4):526–528, 1952. 83

[127] A. Carpinteri and M. Paggi. Analytical study of the singularities arising at multi-material interfaces in 2d linear elastic problems. *Engineering fracture mechanics*, 74(1):59–74, 2007. 84

[128] M. Paggi and A. Carpinteri. On the stress singularities at multimaterial interfaces and related analogies with fluid dynamics and diffusion. *Applied Mechanics Reviews*, 61(2):020801, 2008. 84

[129] A. Seweryn and K. Molski. Elastic stress singularities and corresponding generalized stress intensity factors for angular corners under various boundary conditions. *Engineering Fracture Mechanics*, 55(4):529–556, 1996. 84

[130] Pedro P Camanho and Carlos G Dávila. Mixed-mode decohesion finite elements for the simulation of delamination in composite materials. 2002. 89

[131] E. Buckingham. *Model experiments and the forms of empirical equations*. 1915. 90

[132] E. Shin S. Bazhenov J. Im A. Hiltner, K. Sung and E. Baer. Polymer microlayer composites. *MRS Online Proceedings Library Archive*, 255, 1991. 92

[133] H. Liu and S.M Hsu. Fracture behavior of multilayer silicon nitride/boron nitride ceramics. *Journal of the American Ceramic Society*, 79(9):2452–2457, 1996. xiii, 92, 102, 103, 106

[134] S.Y. Qin J.X. Zhang, D.L. Jiang and Z.R. Huang. Fracture behavior of laminated sic composites. *Ceramics international*, 30(5):697–703, 2004. 92

[135] C.C. Evans J. Cook, J.E. Gordon and D.M. Marsh. A mechanism for the control of crack propagation in all-brittle systems. In *Proceedings of the Royal Society of London A: Mathematical, Physical and Engineering Sciences*, volume 282, pages 508–520. The Royal Society, 1964. 92, 96

[136] L. ShuQin C. Jian W. RuiGang L. Yong-Ming, P. Wei and L. JianQiang. Mechanical properties and microstructure of a si 3 n 4/ti 3 sic 2 multilayer composite. *Ceramics international*, 28(2):223–226, 2002. 93

[137] C. Baudin S. Bueno. Design and processing of a ceramic laminate with high toughness and strong interfaces. *Composites Part A: Applied Science and Manufacturing*, 40(2):137–143, 2009. 93

[138] Y.-H. Yoo W. Lee and H. Shin. Reconsideration of crack deflection at planar interfaces in layered systems. *Composites Science and Technology*, 64(15):2415 – 2423, 2004. 111

[139] S. Kajari-Schröder M. Paggi and U. Eitner. Thermomechanical deformations in photovoltaic laminates. *The Journal of Strain Analysis for Engineering Design*, 46(8):772–782, 2011. 126

[140] C. Kuhn A. Schlüter, A. Willenbücher and Ralf R. Müller. Phase field approximation of dynamic brittle fracture. *Computational Mechanics*, 54(5):1141–1161, 2014. 136

[141] M. Corrado and M. Paggi. Nonlinear fracture dynamics of laminates with finite thickness adhesives. *Mechanics of Materials*, 80:183–192, 2015. 136

[142] N.D. Parab and W.W. Chen. Crack propagation through interfaces in a borosilicate glass and a glass ceramic. *International Journal of Applied Glass Science*, 5(4):353–362, 2014. xv, 137